Dissertation
submitted to the
Combined Faculties for the Natural Sciences
and for Mathematics
of the Ruperto-Carola University of Heidelberg,
Germany
for the degree of
Doctor of Natural Science

presented by
Dipl.-Phys. Hannes Horst
born in Berlin (Germany)
Oral examination: February 6$^{\text{th}}$ 2008

The Mid-Infrared – hard X-ray correlation in Active Galactic Nuclei

Zusammenfassung

Die Korrelation zwischen Mittinfrarot- und Röntgenleuchtkraft in Aktiven Galaktischen Kernen

Der wichtigste Baustein des vereinheitlichten Modells für aktive galaktische Kerne (active galactic nuclei – AGN) ist die Existenz eines absorbierenden Torus. Das vereinheitlichte Modell hat sich in den letzten Jahren als sehr erfolgreich erwiesen; über die physikalischen Eigenschaften des Torus wissen wir jedoch nach wie vor sehr wenig. In dieser Arbeit präsentieren wir räumlich hochaufgelöste Mittinfrarot(MIR)-Bilder von nahen AGN und untersuchen die Korrelation zwischen der – auf das Ruhesystem des jeweiligen Objekts bezogenen – $12.3\,\mu$m- und der absorptionskorrigierten 2-10 keV-Leuchtkaft. Da die Röntgenstrahlen von der Akkretionsscheibe stammen und das Mittinfrarotkontinuum im Wesentlichen vom Torus emittiert wird, wo ein Teil der Strahlung von der Akkretionsscheibe reprozessiert wird, ermöglicht uns diese Methode die Geometrie des Torus zu untersuchen.

In unser Untersuchung finden wir eine starke Korrelation zwischen diesen beiden Leuchtkräften mit $L_{\mathrm{MIR}} \propto L_{\mathrm{X}}^{1.04\pm0.04}$. Außerdem ergeben unsere Daten, dass AGN vom Typ I und vom Typ II mit einer Wahrscheinlichkeit von 97 % das gleiche mittlere Leuchtkraftverhältnis $L_{\mathrm{MIR}}/L_{\mathrm{X}}$ haben. Da es uns die hohe räumliche Auflösung unserer Beobachtungen erlaubt, signifikante Beiträge von Störquellen auszuschließen, ist diese Ähnlichkeit zwischen Typ I- und Typ II-AGN sehr wahrscheinlich echt. Wir interpretieren dies als einen starken Hinweis auf Klumpigkeit des absorbierenden Mediums. Die Steigung der Korrelation befindet sich in guter Übereinstimmung mit den Vorhersagen des vereinheitlichten Modells und impliziert, dass sich die Geometrie des Torus bestenfalls geringfügig mit der Leuchtkaft eines AGN ändert. Darüber hinaus demonstrieren wir die außerordentliche Bedeutung von hoher räumlicher Auflösung für Infrarotstudien von AGN.

Abstract

The mid-infrared – hard X-ray correlation in Active Galactic Nuclei

The cornerstone of the unified scenario for active galactic nuclei (AGN) is the existence of an obscuring torus. While the unified scenario has proven very successful, little is known about the physical state of the torus itself. In this work, we present high spatial resolution mid-infrared (MIR) imaging of 25 nearby AGN. We investigate the correlation between the rest frame $12.3\,\mu$m and absorption corrected 2-10 keV luminosities. Since the X-rays originate in the accretion disc and the MIR continuum is accretion disc radiation reprocessed in the torus, this enables us to constrain the torus geometry.

We find a strong and highly significant correlation between both luminosities with $L_{\mathrm{MIR}} \propto L_{\mathrm{X}}^{1.04\pm0.04}$. Furthermore, we find that with a probability of 97 %, type I and type II AGN have the same luminosity ratio $L_{\mathrm{MIR}}/L_{\mathrm{X}}$. The high spatial resolution of our MIR imaging allows us to exclude any significant non-torus contribution to the AGN

mid-IR continuum, thereby implying that the similarity in the L_{MIR} / L_{X} ratio between type Is and type IIs is intrinsic to AGN. We argue that this is best explained by clumpy torus models. The slope of the correlation is in good agreement with the expectations from the unified scenario and indicates little to no change of the torus geometry with luminosity. In addition, we demonstrate that the high angular resolution is crucial for AGN studies in the IR regime.

Contents

List of Acronyms

ADU	Analog-Digital Unit
AGN	Active Galactic Nucleus / Nuclei
ASCA	Advanced Satellite for Cosmology and Astrophysics
BH	Black Hole
Blazar	combination of "BL Lac" and "Quasar"
BL Lac	BL Lacertae type object
BLR / NLR	Broad / Narrow Line Region
BLRG / NLRG	Broad / Narrow Line Radio Galaxy
CfA	Harvard-Smithsonian Center for Astrophysics
CONICA	The Near-IR Camera part of NaCo
CRIRES	Cryogenic high-Resolution IR Echelle Spectrograph at the VLT
DIT	Detector Integration Time
ESO	European Southern Observatory
FIR	Far InfraRed
fov	Field Of View
FR I / II	Fanaroff-Riley class I / II radio source
FSCD	Flat Spectrum Core Dominant radio source
FUSE	Far Ultraviolet Spectroscopic Explorer
FWHM	Full Width at Half Maximum
HBLR	Hidden Broad Line Region
HST	*Hubble* Space Telescope
IDL	Interactive Data Language
IF	Intermediate Field
INTEGRAL	INTErnational Gamma-Ray Astrophysics Laboratory
IPAC	Infrared Processing and Analysis Center
IR	InfraRed
IRACE	InfraRed Array Control Electronics
IRAS	InfraRed Astronomical Satellite
IRS	InfraRed Spectrograph aboard the *Spitzer* Space Telescope
ISM	InterStellar Medium
ISO	Infrared Space Observatory
ISOCAM / ISOPHOT	IR CAMera / PHOTometer aboard ISO
JEM-X	Joint European X-ray Monitor aboard INTEGRAL
LINER	Low Ionisation Nuclear Emission Region
mas	Milli ArcSecond
MIDI	the MID-Infrared instrument for VLTI
MIR	Mid-InfraRed (here $5\,\mu\mathrm{m} \lesssim \lambda \lesssim 30\,\mu\mathrm{m}$)
NaCo	NAOS-CONICA
NAOS	Nasmyth Adaptive Optics System

NASA	National Aeronautics and Space Administration
NED	NASA/IPAC Extragalactic Database
NLS1	Narrow Line Seyfert 1 galaxy
OVV	Optically Violently Variable quasar
PAH	Polycyclic Aromatic Hydrocarbons
PSF	Point Spread Function
Quasar	Quasi Stellar Radio Source
QSO	Quasi Stellar Object (optical equivalent to quasar)
rms	Root Mean Square
RXTE	Rossi X-ray Timing Explorer
(Beppo)SAX	Satellite per Astronomia a raggi X
SDSS	Sloan Digital Sky Survey
SED	Spectral Energy Distribution
SF	Star Formation / Small Field (only chapter 3)
SINFONI	A near-IR integral field spectrograph at the VLT
SMBH	Super Massive Black Hole
S/N	Signal-to-Noise ratio
SPICE	SPitzer IRS Custom Extraction software
STIS	Space Telescope Imaging Spectrograph aboard HST
Sy	Seyfert Galaxy
ULIRG	UltraLuminous InfraRed Galaxy
ULX	UltraLuminous X-ray source
VINCI	The VLT INterferometer Commissioning Instrument
VISIR	VLT Spectrometer and Imager for the mid-InfraRed
VLT	Very Large Telescope
VLTI	Very Large Telescope Interferometer
TMA	Three Mirror Antistigmatic system
WFPC2	WideField Planetary Camera 2 aboard HST
XMM(-*Newton*)	X-ray Multi-mirror Mission

1 Introduction

> *The more we learn about the world, and the deeper*
> *our learning, the more conscious, specific, and artic-*
> *ulate will be our knowledge of what we do not know,*
> *our knowledge of our ignorance. For this, indeed, is*
> *the main source of our ignorance – the fact that our*
> *knowledge can be only finite, while our ignorance must*
> *necessarily be infinite.*

Sir Karl R. Popper: Conjectures and Refutations: The Growth
of Scientific Knowledge (1963)

1.1 Active Galactic Nuclei

Since Maarten Schmidt (1963) identified the emission lines in the spectrum of the ra-
dio star 3C 273 and deduced that its redshift is 0.16, this new class of quasi-stellar
radio sources (Quasars) has fascinated astronomers throughout the world. Interpreting
this redshift as being cosmological implies a gigantic intrinsic luminosity, and in fact
Quasars are the most luminous non–transient objects ever discovered. In order to ex-
plain this enormous energy output several very different models were proposed, among
them accretion onto a supermassive black hole (Salpeter, 1964; Zeldovich, 1964). This
idea did not become popular until Lynden-Bell (1969) argued that dead quasars in the
form of "collapsed bodies" should be common in quiescent galactic nuclei and might be
detectable through their effect on the mass-to-light ratio. Further support came from
the discovery of variable X-ray sources by the *Uhuru* satellite which turned out to most
probably contain accreting black holes of stellar masses (e.g. see Webster & Murdin,
1972; Tananbaum et al., 1972; Thorne & Price, 1975, for the interpretation of Cyg X-1).

Accretion was soon thought to be an important phenomenon not only in galactic X-
ray sources and AGN, but also in cataclysmic variable stars and protostars. In all these
objects the accreted material usually has a non-negligible amount of angular momentum.
Therefore, it is natural to assume that the accretion takes place in a disc that is oriented
perpendicular to the angular momentum vector. A key uncertainty has long been how
these "accretion discs" transport matter inward while at the same time transporting
angular momentum outward. The α-prescription of turbulent viscosity by Shakura &
Sunyaev (1973) and, later, the more general β-viscosity (Duschl et al., 2000; Richard
& Zahn, 1999) proved to be successful parameterisations of the turbulent processes in
accretion discs. Despite the success of these models, however, some aspects of the hy-
drodynamics in accretion discs are still not well understood.
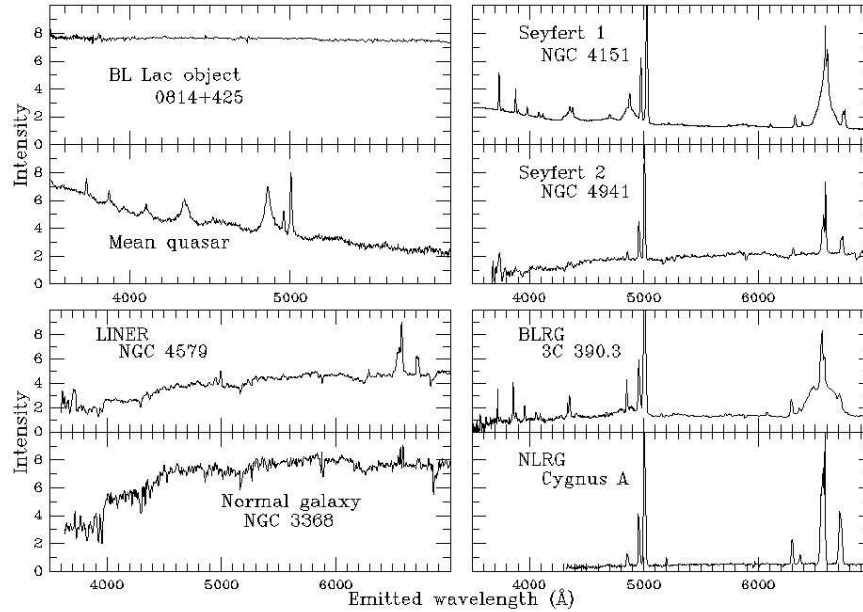
Figure 1.1: Optical spectra of different types of AGN, assembled by William C. Keel (http://www.astr.ua.edu/keel/agn/spectra.html). References for individual spectra: NGC 4941 & 4579: Keel (1983); NGC 3368: Kennicutt (1992); Cygnus A: Owen et al. (1990); 3C 390.3 & 0814+425: Lawrence et al. (1996); mean QSO: Francis et al. (1991); NGC 4151: compiled by Keel from several original sources.

Seyfert (1943) had been the first to systematically analyse galaxies with nuclear emission lines. To make active nuclei of galaxies a prime field of astrophysical research, however, it required the discovery of Quasars and their subsequent identification with the centers of distant galaxies (e.g. by Kristian, 1973). A variety of phenomena of nuclear activity were observed. Apart from Quasars, the most important classes of AGN are Seyfert galaxies, Radio galaxies and Blazars.

Seyfert galaxies appeared as the less luminous local counterparts of Quasars and came in two flavours: With the permitted emission lines showing a more broadened base than forbidden ones (Seyfert 1) and without this extra broadening (Seyfert 2). These very broad lines are also seen in the optical spectra of Quasars and are believed to originate in a region closer to the central black hole than the narrower lines. These regions are called Broad line regions (BLRs) and Narrow line regions (NLRs), respectively. Figure 1.1 shows the optical spectra of different types of AGN. We see the broad line components in the spectra of Seyfert 1 and Broad line radio galaxies (BLRGs) and quasars. They are missing in the spectra of Seyfert 2 and Narrow line radio galaxies (NLRGs).

Radio galaxies show gigantic radio lobes which are often connected to the centre of the galaxy by jets (A beautiful example for such an object is Cygnus A; as illustration, a radio map from Perley et al. (1984) is reproduced in fig. 1.2). Finally, Blazars are characterised by their extremely rapid variability (in some cases on timescales of one day) and polarised optical component. Despite these differences, all these objects show
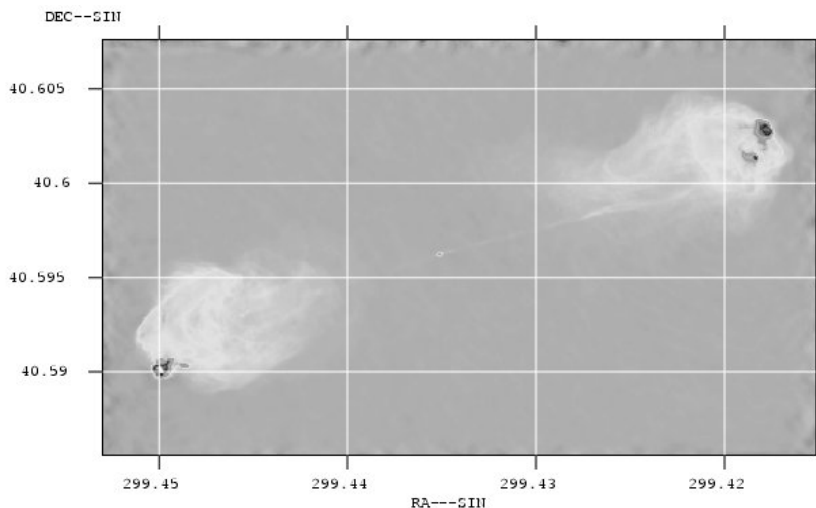
Figure 1.2: Radio map at 6 cm of the prototypical double-lobed radio galaxy Cygnus A, taken by Perley et al. (1984) with the Very Large Array (VLA). Most striking are the giant radio lobes which span a projected distance of 140 kpc. Both lobes show hot spots at their outer edges and are only connected to the central point source by very thin radio jets.

an optical continuum that is fairly well described by a power law and strong optical emission lines. Furthermore, they are usually bright in the X-ray and infrared (IR) regimes. Because of these similarities the question arose whether some aspects of the diversity in AGN appearance may result from the observer's location relative to the AGN. This led to the unified scenario for AGN which will be discussed in the next section. Readers looking for a more detailed account of AGN research may be interested in the review paper by Shields (1999).

1.2 The unified scenario for AGN

The term "unified scenario" is used for two different concepts in AGN research: A single physical model to reproduce radio-quiet type I AGN (with Broad lines) and type II AGN (without Broad lines); a model to unify the different classes of radio-loud AGN. In this section both of these schemes will be briefly discussed. For a more elaborate, but in some points somewhat outdated, account, consult Antonucci (1993) (for both radio-loud and radio-quiet AGN unification) and Urry & Padovani (1995) (for radio-loud unification only).

Radio-loud and radio-quiet AGN clearly require somewhat different physics. As the formation of jets – which power the radio lobes in radio-loud AGN – in accretion discs is still poorly understood, it is not known why some AGN have very powerful jets and others only weak ones or in some cases possibly none at all. Furthermore, the huge range of luminosities from Seyfert galaxies to QSOs (quasi-stellar objects - the name for Quasars and radio-quiet objects with the same optical properties) is largely intrinsic.

Figure 1.3: Idealised view of an AGN and its viewing angle dependent appearance: If the line of sight crosses the obscuring torus, the central continuum source as well as the broad line region clouds are hidden from the observer. Please note that the structures are drawn in logarithmic scale. This figure has been reproduced from Urry & Padovani (1995).
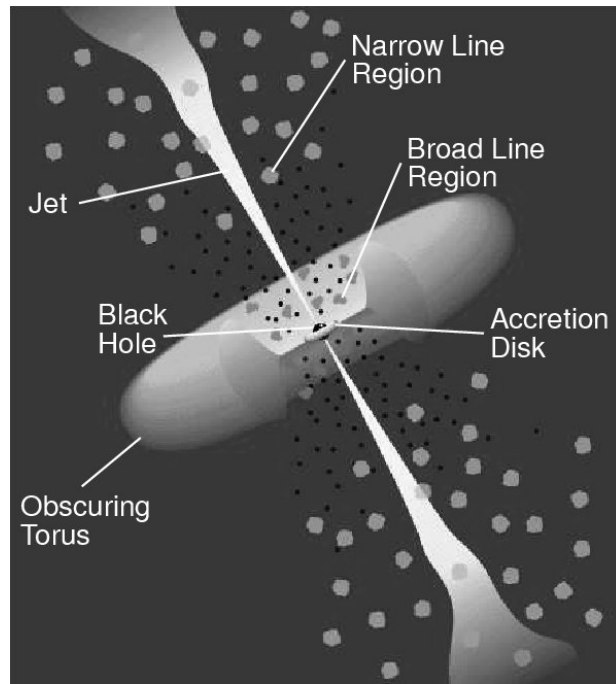
Some aspects of the diverse appearance of AGN, however, can be attributed to orientation effects.

1.2.1 Unification of radio-quiet AGN

Radio quiet AGN consist mainly of four classes of objects: Sy 1 and Sy 2 galaxies at low luminosities and their high-luminosity counterparts, type I and type II QSOs. Sometimes finer distinctions are made: As the strength of the narrow line components increase relative to the broad components, the AGN are assigned types 1.0, 1.2, 1.5, 1.8, 1.9 and 2.0. Furthermore, classifications like 1h (broad lines detected in polarised light only) and 1n (broad line AGN with unusually narrow Balmer lines), etc. have been established. For a precise definition of the different spectroscopic AGN classes, consult e.g. Véron-Cetty & Véron (2000).

The basic idea for explaining type I and type II objects with the same physical model, is the presence of an axi-symmetric absorber, containing molecular gas and large amounts of dust. The geometry of this absorber is thought to be either the one of a torus or of a warped disc. Fig. 1.3 illustrates this concept. In fig. 1.4, I demonstrate how the torus is orientated with respect to the observer in different types of AGN.

The first literature appearance of the idea of an orientation effect as the source for different AGN appearance seems to be a footnote in Rowan-Robinson (1977). It was picked up again, among others, by R. Antonucci to explain the presence of broad lines in the polarised flux of the Narrow Line Radio Galaxy 3C 234 (Antonucci, 1982, 1984) and the Seyfert 2 Galaxy NGC 1068 (Antonucci & Miller, 1985; Miller et al., 1991).

In both cases, the polarised spectrum showed broad lines and a strong continuum, typical for type I AGN, with the polarisation position angle being perpendicular to the radio jet. This was interpreted in the picture described above: While the strong

continuum and broad lines are blocked from direct view by the geometrically and optically thick torus, their light is scattered into the line of sight by electrons and, further outwards, dust grains (Miller et al., 1991) which are situated above (or below) the plane of the torus.

Subsequently, many more type II AGN were shown to exhibit a type-I-like spectrum in polarised light (e.g. by Tran et al., 1992; Lumsden et al., 2004; Zakamska et al., 2005). While these results are the most convincing arguments for the unification of radio-quiet AGN, other methods also contributed to establish the current picture. The strongest argument for the axi-symmetry of the absorber is provided by observations of ionisation cones. These usually have sharply defined conical or even biconical shapes and are often well aligned with the radio jet axis (e.g. Pogge, 1989; Evans et al., 1991; Storchi-Bergmann et al., 1992) and therefore match the picture imposed by the unified scenario. The ionisation cones can be identified with the NLR as illustrated in fig. 1.3.

A still unsettled question is the geometry of the obscuring material. While most theoretical work is done on models for tori (which will be discussed in more detail in chapter 2), some groups also pursue the idea of a geometrically thin but warped disc (e.g. Phinney, 1989; Pringle, 1996; Schinnerer et al., 2000; Galliano & Alloin, 2002).

There have been claims of "pure", unobscured type II AGN (e.g. by Tran, 2003; Tran et al., 2005; Wolter et al., 2005). While this issue has not been settled yet, it seems that pure type II AGN, if they exist at all, are a small subclass of AGN. In section 7.2, we present evidence from MIR imaging against the existence of pure type II AGN.

1.2.2 Unification of radio-loud AGN

As illustrated by 3C 234, the assumption of an axi-symmetric absorber is also employed in the unification of radio-loud AGN. Thus, NLRGs and BLRGs can be explained as being the same kind of objects viewed from different angles, just in the same way as Sy 1s and Sy 2s. There is much observational evidence to support this hypothesis, but since it is of the same kind as for the radio-quiet AGN, it will not be discussed here.

To fully account for the different flavours of radio-loud AGN, however, a second effect has to be taken into account: Relativistic Beaming of a collimated jet. Blandford & Rees (1978) and Blandford & Konigl (1979) proposed that Blazars are radio galaxies viewed along the axis of jets moving with highly relativistic velocities. They explained the low equivalent width of the emission lines in these objects with the continuum being relativistically boosted toward the observer. The most important arguments for a highly relativistic motion of the emitters in blazars are (1) the apparent superluminal motions of distinct knots, (2) the very short variability timescales – which lead to unphysical results on the sizes of the emitting regions if relativistic beaming is not taken into account – and (3) the presence of γ-ray photons up to TeV energies in some blazars (e.g. see Sanders, 1974; Quirrenbach et al., 1992; Tavecchio et al., 1998; Kataoka et al., 1999). In the radio, these sources have remarkably flat spectra and are dominated by the compact jet component. Therefore, they are called Flat-Spectrum Core-Dominant (FSCD) Radio Sources. In the optical, beamed sources are called "BL Lac" type objects and Optically Violently Variable Quasars (OVVs). Both classes are characterised by rapid variability and strong polarisation. The distinction is mostly historical, although most BL Lacs are local objects of luminosities comparable to the ones of Seyfert galaxies while OVVs are more distant and luminous AGN. The term "blazar", a combination of "BL Lac" and
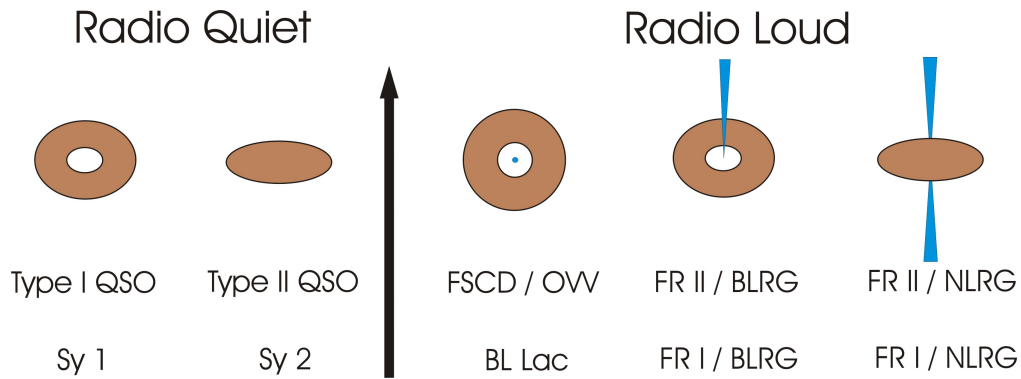
Figure 1.4: Sketch of the unified scheme for AGN. The thick black arrow divides radio-loud from radio-quiet objects and also denotes the direction of increasing luminosity. From left to right, the orientation of the torus (brown "doughnut") and the jet (blue cone) changes from face on to edge on. The weak jets in radio quiet objects have been omitted for clarity.

"Quasar" then usually refers to all beamed AGN.

The idea of blazars to be radio galaxies viewed along the axis of their jets was confirmed by the detection of weak, diffuse radio emission around many FSCDs (Antonucci & Ulvestad, 1984). These weak radio lobes are approximately isotropic, the core emission, on the other hand, shows a strong anisotropy. This is expected if the jet on one side is moving toward the observer while the jet on the other side is moving away. The same asymmetries are found in a large number of BLRGs. Reassuringly, asymmetric jets are much more frequent in BLRGs than in NLRGs which indicates that the jets in NLRGs are oriented closer to the plane of the sky as illustrated in fig. 1.4; see Barthel (1989) for a more thorough discussion of this point.

Another important aim of unified schemes for radio-loud AGN is to explain the dichotomy between Fanaroff-Riley class I (FR I) and FR II galaxies. Fanaroff & Riley (1974) discovered that at a certain critical luminosity in the radio (e.g. at $L_{178} \approx 2{\cdot}10^{25}$W Hz^{-1} at 178 MHz), the morphology of radio galaxies changes significantly. The lower luminosity FR I sources are brightest near the nucleus and show relatively broad jets and weak lobes. The higher luminosity FR II sources, on the other hand, are brightest at the outer edges of the radio lobes and have very thin jets; Cygnus A, the example shown in fig. 1.2, is a typical FR II galaxy.

FR I galaxies, being less luminous than FR II galaxies, seem to be the radio-loud counterparts of Seyfert galaxies and, among the classes of beamed sources, can be unified with the local BL Lac objects[1] which are intrinsically less luminous than beamed Quasars. FR IIs, on the other hand, are the same beasts as Quasars.

The reason for the different appearance of FR Is and IIs is that in FR Is the relativistic jets are weaker, more easily slowed down by the interstellar medium (ISM) and thus unable to inflate the huge radio lobes that are characteristic for FR IIs. Recent observations with the Infrared Space Observatory (ISO) by Müller et al. (2004) have confirmed

---

[1]The BL Lacs at cosmological distances should really be counted as OVVs since the spectroscopic distinction between these two classes is quite fuzzy anyway
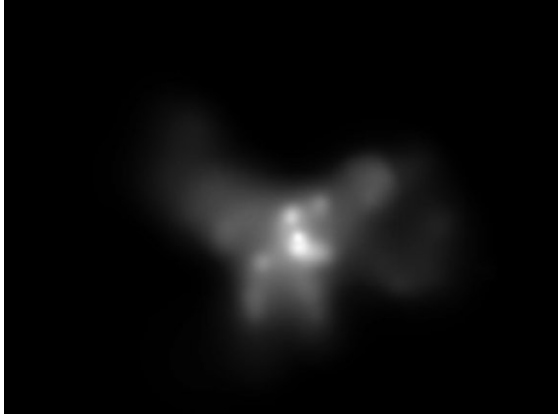
Figure 1.5: $0.1 - 10$ keV image of the ULIRG NGC 6240, taken with the *Chandra* X-ray telescope. The two separate nuclei are clearly visible.

that FR Is are intrinsically less luminous than FR IIs and not merely embedded in thick dust shells. Figure 1.4 illustrates how the different types of AGN fit into the unification scheme.

It should be noted that despite the great success of the unification scenario described above, AGN can have individually differing appearances. This is expected since an AGN depends on and interacts with its environment. The picture gets especially complicated for galaxies in which the type of activity (starburst or AGN) cannot be easily determined. The most important classes of composite objects are Ultraluminous Infrared Galaxies (ULIRGs) and Low Ionisation Nuclear Emission Regions (LINERs). ULIRGs are very dusty objects and always contain starbursts (Sanders & Mirabel, 1996). In addition, some of them contain deeply embedded AGN. One famous example is the double-nucleus of NGC 6240, shown in fig. 1.5.

LINERs have spectroscopic properties which place them between Sy nuclei and H II regions (see fig. 1.1). Some of these objects form the low luminosity end of the AGN population while others seem to be pure star forming objects. The most reliable way to discern between LINERs that contain AGN and those who do not, is to observe them in the X-rays (González-Martín et al., 2006; Flohic et al., 2006). But since the AGN in LINERs can be very weak, it is not always possible to discriminate between those and luminous X-ray binaries (ULXs).

1.3 Evolution of AGN

The scenario proposed by Lynden-Bell (1969) implies that the evolution of AGN is linked to the evolution of their host galaxies. A more specific prediction is that a large number of quiescent galaxies should contain Super Massive Black Holes (SMBHs) as the remnants of past AGN activity. This prediction was indeed proven true. The best known example of a quiescent SMBH is, of course, the one in the centre of our own Galaxy. This object is especially important as it is the one with the tightest constraints on mass and radius, ruling out most alternatives to BHs (Schödel et al., 2003).

We also find SMBHs at the centre of most other quiescent nearby galaxies (e.g. see Richstone et al., 1998). In addition, their mass even seem to correlate with that of the Bulge component of the host galaxy (Wandel, 1999; Ferrarese & Merritt, 2000; Gebhardt

et al., 2000) which indicates that the BH and its host galaxy evolve together and influence each other.

Even before these correlations were found, astronomers wondered how the gas that fuels an AGN (and makes the BH grow) gets into the centre of the host galaxy. One very popular idea is that external events disturb the kinematic structure of the galaxy and make gas fall inward. The most violent of these events are major mergers, i.e. mergers between two galaxies of comparable mass. Sanders et al. (1988) proposed that ULIRGs are transition objects: post-mergers and pre-AGN. ULIRGs show a significantly higher frequency of disturbed morphology and close companions than quiescent galaxies, and contain sufficient cold gas to fuel an AGN. This idea was later also supported by theory. Barnes & Hernquist (1996) showed that tidal interactions with close companions can, indeed, sufficiently disturb a galaxy in order to funnel gas into its centre.

Further evidence for this evolutionary scenario is provided by the redshift distribution of powerful quasars which has been determined quite accurately for X-ray selected QSOs (e.g. by Silverman et al., 2005). This distribution can be qualitatively reproduced by the major merger scenario, independently of the chosen structure formation model (Horst & Duschl, 2007). N-body simulations of galaxy mergers by Hopkins et al. (2006) show that, indeed, many observables, e.g. the AGN luminosity function, the column density distribution, the mass function of local SBMHs and the X-ray background, are fully consistent with the major merger scenario. Furthermore, it nicely fits into the cosmological concept of hierarchical structure formation.

On the other hand, host galaxies of local AGN do not show an increased frequency of significantly disturbed morphologies or close companions compared to quiescent galaxies (e.g. Grogin et al., 2005), in contradiction to the expectations from the major merger scenario. The resolution of this problem seems to be that AGN activity at low to moderate luminosities can be triggered by minor instabilities leading to the infall of small amounts of matter into the nucleus (King & Pringle, 2007) while, on the other hand, luminous quasars are triggered by more violent events (major mergers and, potentially, galaxy formation by monolithic collapse).

1.4 Current problems in AGN research

There are still many open questions regarding AGN. Three of these currently receive particular interest: AGN – host galaxy co-evolution, the formation of the first QSOs and the physical state of the axi-symmetric absorber.

It seems highly unlikely that different kinds of merger and instability events lead to the same fueling rate of the AGN, relative to the bulge mass. One possible explanation for the observed BH – bulge mass correlation is that every event that significantly enlarges the bulge also causes the central BH to grow close to the Eddington limit. Another possibility is a feedback process that induces self-regulation of BH growth. The most important feedback effect is probably the heating of the circumnuclear environment via energetic jets and winds (Begelman, 2003). Furthermore, radiative heating may be important as well. These heating processes will have two effects: Expelling gas from the centre of the galaxy and heating up molecular clouds and, thus, shutting down star formation. Unfortunately, the efficiency of these effects is still poorly constrained.

The field of AGN and host galaxy co-evolution touches the second major problem, the Astrophysicist's version of the hen and egg question: Did the first QSOs form in the cores of the first galaxies or did the first galaxies assemble around primordial SMBHs (Carr, 1975)? The detection of galaxies and QSOs at redshifts above 6 makes it increasingly unlikely that these objects can have formed by hierarchical merging. As demonstrated by Immeli et al. (2004), however, a monolithic galaxy formation is a plausible way to form galaxies at high redshifts. Thus, there is still no need to invoke primordial BHs in galaxy evolution. On the other hand, we have to wonder whether the SMBHs are formed along with the galaxy in a monolithic collapse or, later on, in a merger event. I believe that for the highest redshift QSOs the first alternative is much more likely. This view is supported by the recent result of Shields et al. (2006) who find the BH – bulge mass relationship to change at redshifts $z > 3$ toward less massive bulges.

Finally, the physics and geometry of the obscuring material in AGN continues to raise questions. Even the hypothesis that the absorbing medium has the geometry of a torus is not undisputed. Some authors (Phinney, 1989; Schinnerer et al., 2000; Galliano & Alloin, 2002) prefer to think of the obscuring medium as a thin, warped disc. The majority of models, however, does assume a torus-like geometry. The torus hypothesis is also supported by most observations, i.e. the biconical ionisation cones found in many AGN. Furthermore, we know that the absorbing material is very compact (e.g. Weigelt et al., 2004; Tristram et al., 2007) and has to be geometrically thick in order to reproduce the observed type I / type II ratio of $\sim 1/3$ (Osterbrock & Martel, 1993; Maiolino & Rieke, 1995; Akylas et al., 2006). This favors a geometry resembling a torus rather than a warped disc.

Another open question in this respect is whether the material in the torus is smoothly distributed (Pier & Krolik, 1992) or arranged in discrete clumps (Krolik & Begelman, 1988). While this debate is far from being settled, recent models for clumpy tori by Nenkova et al. (2002); Dullemond & van Bemmel (2005); Hönig et al. (2006) have proven successful in reproducing infrared observations of AGN. A full hydrodynamical treatment of clumpy tori, however, is still missing.

As we have seen, the putative torus is the key ingredient of the unified scenario. Therefore, to constrain its physical properties is of paramount importance for our understanding of AGN. In this work, we will try to contribute to this task by investigating the correlation between mid-IR and hard X-ray luminosities in AGN. A more thorough discussion of the models for AGN tori and the observational evidence we have, will be given in chapter 2.

1.5 The mid-IR – hard X-ray correlation and the scope of this work

The mid-infrared (MIR) – hard X-ray correlation is an interesting tool to test the unified scenario in general and different classes of torus models in particular. The intrinsic hard X-ray luminosity, i.e. corrected for absorption in the torus, is a good proxy for the bolometric luminosity of the accretion disc. The MIR luminosity, on the other hand, measures the total thermal dust re-emission from the torus. As the dust is heated by optical and UV photons from the accretion disc, a correlation between the intrinsic hard

X-ray and MIR luminosities is expected for AGN. This expectation was confirmed by Krabbe et al. (2001) and Lutz et al. (2004). The properties of the correlation these authors found, however, does not agree with model predictions. More details on this will be given in section 2.3.4.

Our contribution to this line of work is to observe a sample of AGN with – in the MIR – unsurpassed angular resolution and, thus, present data that is largely free of contamination from extra-nuclear emission. The X-ray data we use have been taken from the literature. An extensive search enabled us to select the observations of highest data quality and compare the results of different X-ray observations of the same objects. Therefore, our results are well suited to constrain the geometry of obscuring dust tori in AGN.

In order to set the stage, I will present the basic theory of obscuring tori in chapter 2. Different models as well as observational constraints will also be briefly discussed. In chapter 3, I will discuss the observing techniques for ground-based MIR observations as well as some specific properties of the VISIR instrument which we used.

Chapter 4 will then deal with the preparation and conduction of our two observing campaigns with the results being presented in chapter 5. The implications of our results for models of AGN as well as a comparison to results of projects similar to our own are put forward in chapter 6.

In chapter 7, I present a few other projects I have been involved in during my time as a Ph.D. student and which are relevant for the topic of this thesis. Finally, our conclusions as well as an outlook on present and future activities are given in chapter 8.

2 The physics of AGN tori

There's a tiresome young man in Bay Shore
When his fiancée cried, 'I adore
The beautiful sea',
He replied, 'I agree,
It's pretty, but what is it for?'

Morris Bishop, reproduced from 'Abstract and Concrete
Categories: The Joy of Cats' by Jiří Adámek, Horst Herrlich and
George E. Strecker

2.1 Basic geometry of the torus

An obscuring torus is the key ingredient of the AGN unification scenario. As we have seen (section 1.2.1), there is strong observational evidence for an axi-symmetric absorber to be the cause of the Sy 1 / Sy 2 dichotomy. Moreover, there are good indications that the absorber is compact and torus-shaped. With this assumption, its geometry can be constrained by some simple arguments.

2.1.1 The radius of the torus

The material absorbing the UV and optical continuum and broad line emission in type II AGN, is dust. This dust is assumed to be similar to the one observed in the Galactic interstellar matter and, thus, to consist mainly of different types of carbon and silicate grains. Based on this assumption, we can calculate the temperature $T_{\rm sub}$ at which dust particles sublimate. This process then defines the inner radius of the dusty part of the torus (Barvainis, 1987). As silicate dust is destroyed at lower temperatures than carbonaceous dust, I only consider the latter for the following calculations.

If we assume that the heating of the dust is mainly due to optical and UV radiation, and the emission mainly in the IR regime, a dust particle is in radiative equilibrium, if

$$\int_{\rm UV, optical} \pi a^2 Q_{\rm abs} F_\nu^{AD} d\nu = \int_{\rm IR} 4\pi a^2 Q_{\rm abs} \pi B_\nu(T) d\nu \,, \tag{2.1}$$

where a is the radius of the dust particle, $Q_{\rm abs}$ the absorption efficiency, F_ν^{AD} the radiation field at frequency ν originating in the accretion disc, and $B_\nu(T)$ the Planck function at temperature T. In the UV and optical and for small grains ($a \lesssim 0.05\,\mu{\rm m}$), we can assume $Q_{\rm abs}$ to be ≈ 1, while in the IR we can approximate it by a power-law:

$Q_{\text{abs}}/a = q_0 \nu^\gamma$ with $\gamma = 8/5$ (see the absorption efficiency plot in Draine & Lee, 1984). Here, we use $a = 0.04\,\mu\text{m}$, $q_0 = 2.99 \cdot 10^{-17}\,\text{m}^{-1}\,\text{Hz}^{-8/5}$ at $\nu = 3 \cdot 10^{14}$ Hz (wavelength $\lambda = 1\,\mu\text{m}$), as used in the radiative transfer calculations by Hönig et al. (2006). We then obtain the equilibrium temperature of the dust:

$$T_{\text{eq}} = 1136\,\text{K} \cdot L_{45}^{5/28}\, r_{\text{pc}}^{-10/28}\, a_{0.04\,\mu\text{m}}^{-5/28} \tag{2.2}$$

with r_{pc} being the radius with respect to the primary radiation source in parsec, $L_{45} = \int_{\text{UV,optical}} 4\pi r^2 F_\nu d\nu / 10^{45}$ erg s^{-1} the source luminosity in units of 10^{45} erg s^{-1} and $a_{0.04\,\mu\text{m}}$ the grain radius in units of $0.04\,\mu\text{m}$. The dust grains sublimate when $T_{\text{eq}} = T_{\text{sub}}$; using the sublimation temperature for graphite, $T_{\text{sub}} = 1500$ K, we get the sublimation radius r_{sub}:

$$r_{sub} = 0.46\,\text{pc} \cdot L_{45}^{1/2}\, T_{sub}^{14/5}\, a_{0.04\,\mu\text{m}}^{1/2}. \tag{2.3}$$

We will, henceforth, assume r_{sub} to be the inner radius of the dusty torus. Very recently, Kishimoto et al. (2007) found that near IR reverberation mapping of type I AGN agrees with the general picture of r_{sub} defining the inner radius of the torus. They find indications, however, for the dust chemistry to differ from the one in Galactic molecular clouds.

The existence of a sharp outer radius of the torus is much less obvious. The obscuring material may smoothly connect to the ISM in the AGN's host galaxy. SINFONI observations of NGC 3227 by Davies et al. (2006) show an ordered velocity field of molecular hydrogen out to radii of $10 \sim 20$ pc. We can therefore assume, that the torus stretches out to a few tens of parsecs.

2.1.2 The vertical extent

So far, we have considered the radial extent of the torus. In order to be an efficient absorber it has to be geometrically thick, in addition to be optically thick. We can infer its scale height by considering the ratio of type I to type II AGN which is estimated to be close to 1/3 (Osterbrock & Martel, 1993; Maiolino & Rieke, 1995; Akylas et al., 2006). We define θ as the half opening angle of the torus and Ω_{torus} as the solid angle it covers when seen from the nucleus. Then, the covering factor f_C of the torus is given by

$$f_C = \frac{\Omega_{\text{torus}}}{4\pi} = \cos\theta. \tag{2.4}$$

For $f_C \approx 2/3$, we get $\theta \approx 45°$. We now assume that the height h of the torus follows a simple radial dependence of the form $h(r) \propto r^\alpha$. Henceforth, we call α the flaring parameter. From this assumption, we obtain

$$f_C = \cos \arctan \left(c\, r_{\text{sub}}^{1-\alpha} \right), \tag{2.5}$$

where c is a constant and has the dimension pc$^{\alpha-1}$. The simplest solution for this equation is $h(r) = r$. In case α was smaller than unity, eq. 2.4 still requires $h(r_{\text{sub}}) \approx r_{\text{sub}}$ in order to match the observed Sy 1 / Sy 2 ratio. Therefore, we find $c \approx 1$ pc$^{\alpha-1}$.

2.2 The physical state of the torus

After the basic geometry of the torus has been established, we can now look into the theoretical considerations for the physical state of the torus in more detail.

2.2.1 The need for clumpiness

As mentioned earlier, there is still debate over whether the torus is clumpy or not. The basic argument for clumpiness, given by Krolik & Begelman (1988), is the dynamics of the torus: In order to dynamically support the geometric thickness of the torus, we require

$$\frac{\Delta v_z}{v_\varphi} \approx \frac{h}{r}, \tag{2.6}$$

where Δv_z is the velocity dispersion perpendicular to the torus mid-plane and v_φ is the torus' orbital velocity. This yields random velocities $\gtrsim 100$ km s^{-1}. If these velocities were thermal, the resulting temperature ($\sim 10^6$ K) would be too high to allow for the existence of dust. In sufficiently cold gas, however, these velocities would be highly supersonic. Dissipation of such motion can only be avoided if the collision rate between streams of different velocities is small – which can be achieved if the cool gas is organised in clouds.

An alternative to the scenario described above, is to – at least partially – support the thickness of the torus by pressure. This was proposed by Pier & Krolik (1992). Such pressure could be provided either by the radiation from the accretion disc, or by a large number of luminous stars combined with supernovae. The first possibility was investigated by Krolik (2007) who found a 2d axi-symmetric solution for a radiatively supported torus. Since, however, inwardly directed IR radiation is not considered in his model its applicability is not evident. The second possibility requires a very recent episode of intensive star formation which, in turn, requires fragmentation of the molecular gas. Thus, even if the torus was supported by radiation pressure from stars and supernovae, one would expect the medium to be clumpy. Please note, that for his modeling of a smooth torus, Schartmann et al. (2005) had to use a supernova rate that significantly exceeds the observed value.

2.2.2 Global structure

A basic analysis of the global structure of a molecular torus around a SMBH was provided by Camenzind (1995) and Schartmann et al. (2005). These authors assume the gas and dust to reside in a potential of the form

$$\phi_{\text{tot}} = \phi_{\text{BH}} + \phi_{\text{SC}} + \phi_{\text{CF}}, \tag{2.7}$$

where ϕ_{BH} is the gravitational potential of the BH, ϕ_{SC} the one of the nuclear star cluster and ϕ_{CF} the potential of the centrifugal force. Furthermore, they assume that the dust is provided by stars and, therefore, has the same rotational velocity and velocity dispersion as these donor stars. Assuming a density and velocity profile for the star cluster, the
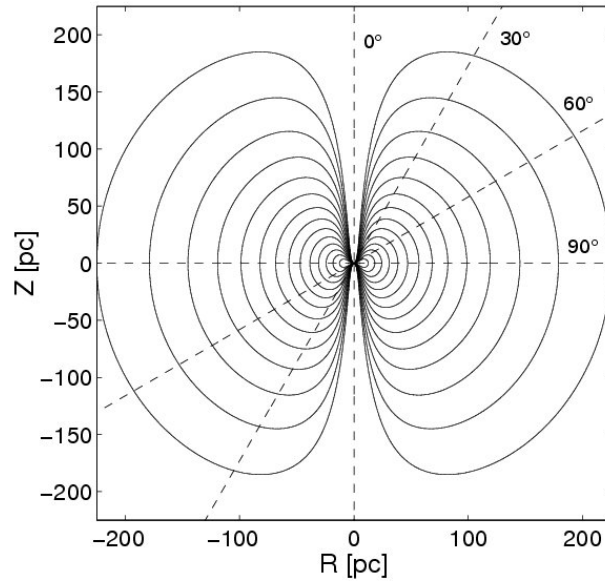
Figure 2.1: Isopynes (lines of constant density) for the Camenzind-Schartmann model in the $r - z$ plane. Numbers are in kg m^{-3}. Dashed lines indicate different angles from the torus axis. Figure reproduced from Schartmann et al. (2005).

Poisson equation for the torus can be formulated. For a torus in hydrostatic equilibrium and with the further assumption that the torus is isothermal, a density distribution for the dust can finally be obtained. An example is displayed in fig. 2.1. Close to the inner wall of the torus, the density is steeply declining; the density profile then flattens toward the outer parts of the torus. It is also important to note that the dust-free cone has steep walls which means that the opening angle is small.

Structure of clumpy tori

The major shortcoming of the physical considerations presented above is the neglection of cloud interactions. While clumpiness of the medium is assumed it is not taken into account for the analysis of the global properties of the torus.

This issue was addressed by Vollmer et al. (2004) and Beckert & Duschl (2004) who consider a torus that consists of distinct clouds, confined by self-gravity. The basis of their model is the assumption that kinetic energy that is dissipated in the torus drives a turbulent cascade down toward ever smaller spatial scales until fragmenting structures are inherently stable: self-gravitating clouds close to the shear limit are formed. The source of the kinetic energy that drives the turbulent cascade is accretion of interstellar matter (ISM) toward the AGN. The resulting clumpy torus is still accreting, with energy being dissipated in cloud-cloud collisions. This can become a stationary process with the torus being the link between ISM and AGN.

The effective viscosity of this system depends on the collision rate between individual clouds. The latter is parameterised by the dimensionless collision time $\tau = v_\varphi/r\omega_{\text{coll}}$ where ω_{coll} is the mean collision frequency for one cloud. Then the viscosity ν is

$$\nu = \frac{\tau}{1 + \tau^2} \frac{(\Delta v_z)^2 r}{v_\varphi}. \tag{2.8}$$

Except for the innermost part of the torus, the accretion time scale Beckert & Duschl (2004) derived via eq. 2.8 is smaller than the star formation timescale. Thus, in this
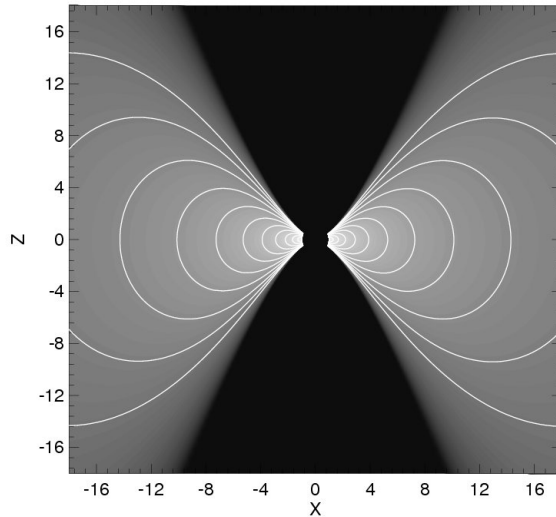
Figure 2.2: Density distribution for the collisional torus model. Meridional cut (here x is the radial coordinate) through the mass density distribution in the torus. Spatial coordinates have been scaled to the dust sublimation radius. Figure reproduced from Beckert et al. (2004).

picture star formation and subsequent supernovae are not important for the dynamics of the torus.

Combining the assumption of marginally stable clouds with the one of an isothermal torus governed by a gravitational potential of the form of eq. 2.7 allows us to derive a density distribution for the torus. An example is shown in fig. 2.2. The shape of the isopynes is significantly different than the ones derived by Schartmann et al. (2005) as shown in fig. 2.1. In particular, the clumpy torus has a wider opening angle and an overall flatter shape. For the clumpy model, the number of obscuring clouds N for an inclination i of the torus toward the observed (where $i = 0$ corresponds to a face-on view of the AGN) is

$$N(i) = \int_{s_{\mathrm{sub}}}^{s_{\mathrm{out}}} \frac{ds}{l_{\mathrm{coll}}} = \sin^{-1} i \int_{r_{\mathrm{sub}} \cos i}^{r_{\mathrm{out}} \cos i} \frac{dr}{l_{\mathrm{coll}}} \,, \qquad (2.9)$$

where l_{coll} is the mean free path for single clouds and r_{out} is the effective outer radius of the torus. The obscuring hydrogen column density then is

$$N_{\mathrm{H}}(i) = \int_{s_{\mathrm{sub}}}^{s_{\mathrm{out}}} \frac{ds}{l_{\mathrm{coll}}} N_{\mathrm{H,Cl}}(s) \,, \qquad (2.10)$$

with $N_{\mathrm{H,Cl}}$ being the hydrogen column of a single cloud. For a typical Seyfert 2 galaxy, this model yields between 6 and 10 clouds along the line of sight, on average. Due to this small number, fluctuations in the hydrogen column densities toward Seyfert nuclei are expected. The mass accretion rates $\dot{M}$ that correspond to these cloud densities and the observed opening angles of AGN tori are beyond the Eddington limit ($\dot{M} \approx \dot{M}_{\mathrm{Edd}}$). This is not in disagreement with the observed sub-Eddington luminosities of the AGN as a substantial amount of matter can be lost in outflows along the ionisation cones (Krolik & Kriss, 2001).

2.2.3 Dependence on luminosity

In the framework of the collisional torus model, accretion through the torus is required to support its geometric thickness. If the accretion rate declines, some of the remaining clouds will be scattered inward onto the accretion disc. Without sufficient energy resupply, the velocity dispersion will decrease and, finally, the torus collapses to a thin disc, similar to the one we find around the Galactic Centre (Vollmer et al., 2004). In a recent study, Hönig & Beckert (2007) determined the minimum bolometric luminosity of an AGN in order to support a geometrically thick torus to be $L_{\text{low}} \approx 5 \cdot 10^{42}$ erg s^{-1}.

Interestingly, the same luminosity was derived by Elitzur & Shlosman (2006) who used a very different approach to explain the structure of AGN tori: In contrast to the accretion scenario discussed so far, they argued that the torus is produced by a wind in which material is blown off the surface of the accretion disc, cools down and eventually forms dust. Here, the reason for the collapse of the torus is that in AGN with low accretion rates the disc wind cannot provide enough mass to support a thick and dense torus.

Another aspect of clumpy tori Hönig & Beckert (2007) investigated is the effect of radiation pressure on the torus structure. First of all, since the matter density within clouds declines with radius, the Eddington luminosity for individual clouds is a function of r. If we consider the largest clouds that are marginally stable against gravitational collapse, we get

$$L_{\text{Edd,Cl}} \quad \sim \quad r^{-3/2} \,. \tag{2.11}$$

Limiting the discussion to the largest clouds only is justified as these provide the strongest obscuration of the central engine. An important implication of rel. 2.11 is that large clouds at large radii are blown away from the torus if they are not shielded by other clouds. Therefore, strong flaring of the torus is inhibited and we expect $h(r)/r \approx$ const. Furthermore, radiation pressure also affects clouds situated at the inner edge of the torus. Above a luminosity $L_{\text{bol}} \approx 10^{45}$ erg s^{-1}, the maximum cloud size is set by radiation pressure rather than the shear limit. In this case, the volume filling factor declines and, effectively, the covering factor behaves as

$$f_C = \frac{\Omega_{\text{torus}}}{4\pi} \propto L^{-1/4} \,. \tag{2.12}$$

Thus, for AGN of increasing luminosities, we expect the type I / type II ratio to increase, as well. Strictly speaking, rel. 2.12 only applies for accretion at the Eddington limit, i.e. $L = L_{\text{Edd}}$. For Eddington ratios significantly lower than unity, the dependence of the covering factor on luminosity can be quite different.

2.3 Observational constraints and torus models

In the last section, I presented our current theoretical understanding of the physical state of the torus. In order to test these theoretical concepts, we have to compare their predictions to observations of AGN. As has been laid out in section 1.2.1, the evidence for the existence of obscuring tori is quite firm. To observationally constrain their geometry
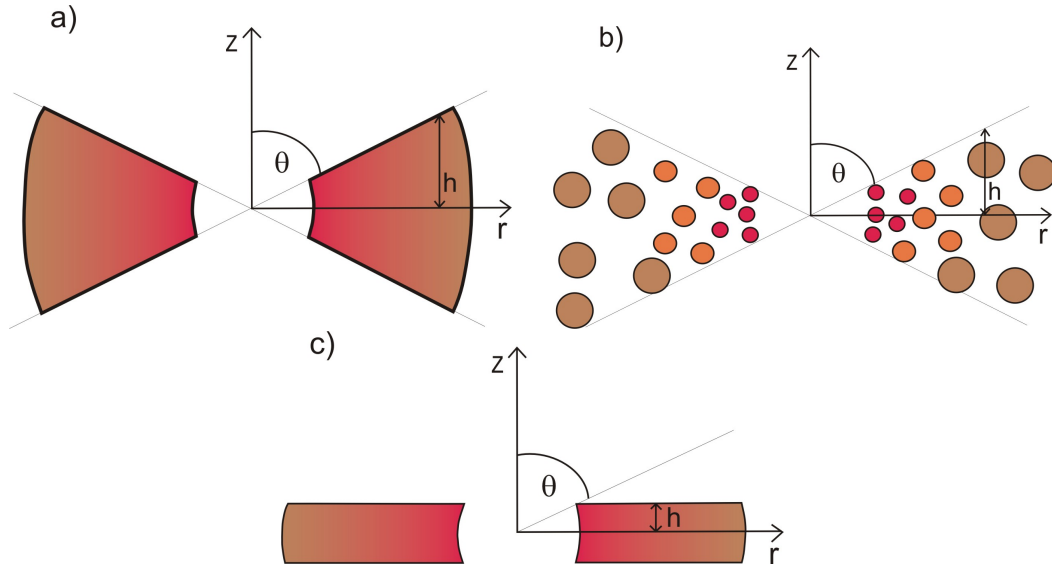
Figure 2.3: Sketch of different torus geometries that are considered in models. a): Flared disc geometry with constant h/r and half opening angle θ. b): As a) but with a clumpy rather than smooth dust distribution. c): coplanar, cylindrical disc with constant h.

(see fig. 2.3 for a sketch of different torus geometries that are considered in models) and physics, however, is a more demanding task. The most important achievements in this line of work will be briefly discussed in the following.

2.3.1 Mid IR SEDs and radiative transfer modeling

One of the most straightforward, and also most important tests of torus models is to compare the predicted dust emission to the observed one. The dust in the torus has temperatures between $200 \sim 1500\,\mathrm{K}$, therefore it mainly radiates in the mid infrared regime and its spectral energy distribution (SED) peaks at around $10\,\mu\mathrm{m}$.

Pier & Krolik (1993) compared the SED expected for a compact, cylindrical torus with MIR observations of NGC 1068 and several PG quasars. They found general agreement between observed and model SEDs. However, the absence of the $9.7\,\mu\mathrm{m}$ silicate feature in some type 2 and all type 1 objects proved to be a problem for the model. This was also noted by Efstathiou & Rowan-Robinson (1995) who tried to reproduce observations using different torus geometries. They found that models produced either too narrow an IR continuum or silicate features that are much stronger in absorption for type II objects than the observed ones. The comparably best results were obtained for tapered discs which behave like flared discs close to the sublimation radius and then flatten out and become coplanar for larger radii.

With the *Spitzer* space telescope, different groups (Hao et al., 2005; Siebenmorgen et al., 2005; Sturm et al., 2005), for the first time, managed to un-ambiguously detect the silicate feature in emission for some type I AGN. The feature, however, turned out to

Figure 2.4: Average MIR spectra for different AGN types, observed with *Spitzer*. The 9.7 μm feature appears strongly in absorption for ULIRGs and Sy 2 galaxies and mildly so for Sy 1 galaxies. Only quasars show the feature in emission. Figure reproduced from Hao et al. (2007).
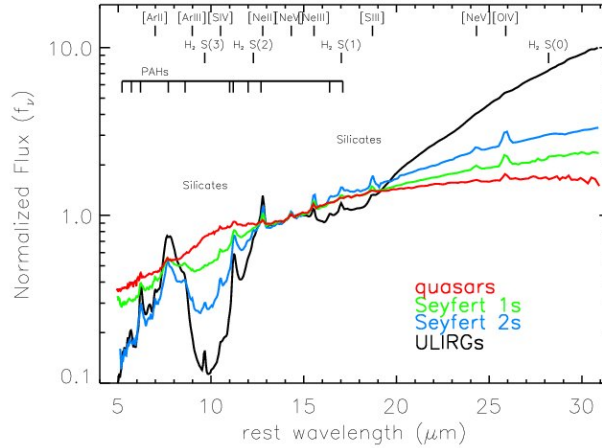
Figure 2.5: Comparison between the observed SED of NGC 1068 (blue diamonds and red curve) and a model SED based on the collisional torus model. The shaded area shows the range of model SED variations for different random cloud arrangements, the dark grey line is the average of these different SEDs. Figure reproduced from Hönig et al. (2006).
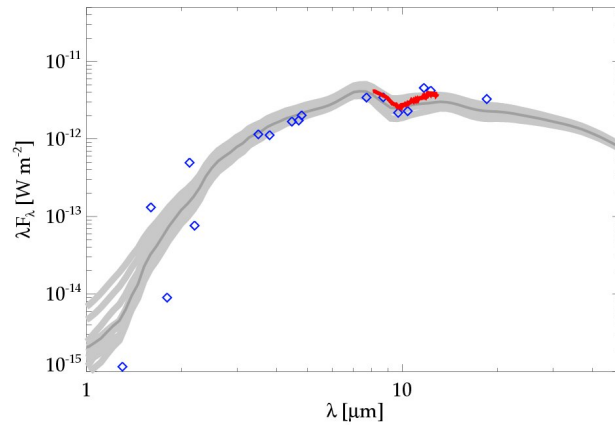
be rarer and weaker than expected from model calculations. As can be seen in fig. 2.4, the average MIR spectrum for Sy 1 galaxies even shows the feature weakly in absorption.

Nenkova et al. (2002) showed that the problems with fitting the shallow silicate features and the widths of the IR SEDs could be solved by accounting for the clumpiness of the emitting medium in the radiative transfer calculations. More recently, Hönig et al. (2006) performed 3D-modeling of clumpy tori, based on the collisional torus model. They showed that the application of their model to the prototypical Sy 2 galaxy NGC 1068 produces a SED that is in very good agreement with the observed one (fig. 2.5). The comparison of this kind of model SEDs to the ones of type 1 AGN also shows promising results (S. F. Hönig, private communication). The reason for the success of the clumpy ansatz is that, for type I sources, self-absorption within the torus can be accounted for: The cloud faces that are heated directly by the AGN show the silicate feature in emission while the cool sides of the clouds that face outward show it in absorption. The result is a very weak feature in either emission or absorption for type I sources. Similarly, in type II sources the absorption feature is weakened by the clumpy structure.
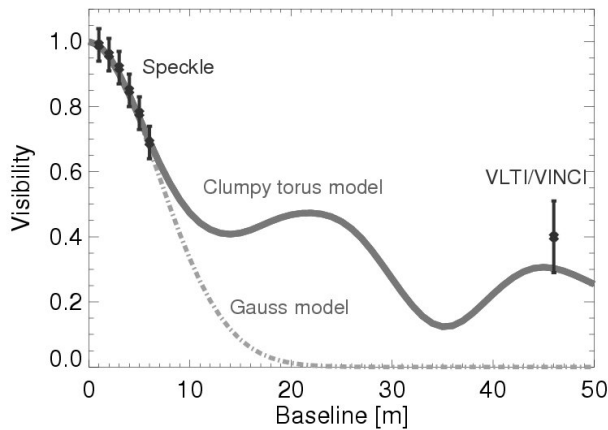
Figure 2.6: Comparison between K-band model visibilities for the collisional torus model (thick grey line), a simple Gaussian visibility curve (dashed-dotted lines) and observations of NGC 1068 (black diamonds). Figure is reproduced from Hönig et al. (2007).

2.3.2 Infrared interferometry

So far, high quality mid infrared interferometry data have been published only for three AGN: NGC 1068, Cen A and Circinus. They show very different structures.

In the case of Cen A, MIDI observations show that the bulk of the mid infrared radiation originates in an unresolved source. Therefore, Meisenheimer et al. (2007) suggest that the IR continuum of Cen A is not dominated by a dusty torus but by synchrotron emission from the base of the jet. In this picture, the prominent silicate absorption feature is produced in a foreground screen of cold dust – the famous dust lane in the host galaxy. However, Cen A is a weak AGN and, therefore, the torus may be too small to be resolved with the used MIDI observation. Meisenheimer et al. (2007) state a resolution of < 10 milli arcseconds (mas) while from eq. 2.3 we expect r_{sub} to be equivalent to $\lesssim 1$ mas.

In the case of Circinus, MIDI observations obtained by Tristram et al. (2007) do show indications for extension of the primary source of MIR radiation. They fit the observed visibilities using two components: A dense and warm disc of 0.2 pc radius and a less dense and cooler, geometrically thick component of ~ 1 pc radius which they identify with the obscuring torus. Furthermore, the observed visibility dependence on projected baseline is interpreted as a signature for clumpiness inside the torus.

For NGC 1068, K-band bispeckle and long-baseline interferometric data were analysed by Hönig et al. (2006). They found overall agreement between the visibilities and the collisional torus model. In fig. 2.6, the observed K-band visibilities of NGC 1068 are shown. A smooth torus is expected to have a Gaussian visibility curve. As can be seen, such a profile does not the match the VINCI observation. A clumpy torus model, on the other hand, can reproduce the data very well.

2.3.3 The type I / type II ratio

Another powerful, yet simple, tool to constrain torus models is to use the number statistics of type I and type II sources. As mentioned in section 2.1.2, the type I / type II ratio constrains the opening angle of the torus. Observations have shown, however, that this ratio depends on luminosity: The relative frequency of type I AGN compared to

Figure 2.7: Mid IR – hard X-ray correlation found by Lutz et al. (2004) – figure reproduced from their paper. Blue diamonds are type I (Sy 1.0-1.5) AGN, red stars are type II (Sy 1.8-2.0) AGN. The dotted line denotes slope unity.
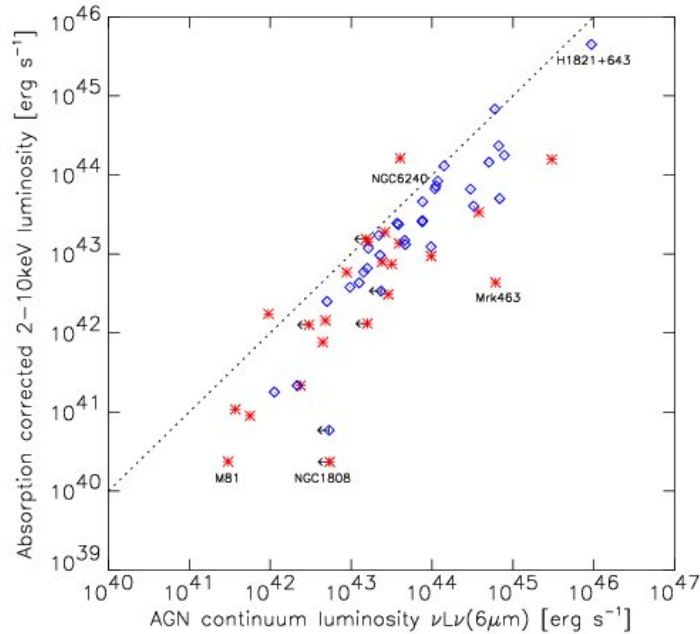
type IIs increases with luminosity from ~ 0.2 for $L_{2-10\,\mathrm{keV}} \lesssim 5 \cdot 10^{42}$ erg s^{-1} to ~ 0.6 for $L_{2-10\,\mathrm{keV}} \gtrsim 5 \cdot 10^{44}$ erg s^{-1} (Simpson, 2005, and references therein). Therefore, Lawrence (1991) suggested the "receding torus model" for which the opening angle increases with luminosity. The simplest incarnation of such a model is a coplanar disc (see fig. 2.3) with a scale height that is independent on accretion rate. As the sublimation radius of the torus increases with luminosity the solid angle covered by it decreases. This model was later refined by Simpson (2005) who found the type 1 fraction f_1 to depend on the $\lambda 5007$ [O III] luminosity $L_{\mathrm{[OIII]}}$ as

$$f_1 = 1 - \left(1 + 3\left(L_{\mathrm{[OIII]}}/L_0\right)^{0.54}\right)^{-0.5}. \tag{2.13}$$

with $L_0 = 10^{41.9}$ erg s^{-1}. For $L_{\mathrm{[OIII]}}/L_0 \gg 1/3$, eq. 2.13 yields $f_2 = 1 - f_1 \propto L_{\mathrm{[OIII]}}^{-0.27}$ which is close to the finding of Hönig & Beckert (2007) as laid out in eq. 2.12. And, indeed, the clumpy torus model offers an alternative explanation for the luminosity dependence of the type I / type II ratio: Instead of assuming the opening angle to increase with luminosity, it predicts the clumps to be packed less densely within the torus.

2.3.4 The mid-IR – hard X-ray correlation

Finally, the mid-IR – hard X-ray correlation can serve to constrain torus models. First of all, a strong correlation between the absorption-corrected hard X-ray luminosity L_X and the MIR luminosity L_{MIR} is expected for AGN. Moreover, the anisotropy of the torus emission should cause an offset in the L_{MIR}/L_X ratio: In type II objects, the hottest dust close to the sublimation radius is hidden from the observer, therefore the L_{MIR}/L_X ratio should be lower than in type I AGN by up to one order of magnitude (Pier & Krolik, 1992).

The correlation was first investigated by Krabbe et al. (2001) who found a strong correlation between the N-band ($8 - 13\mu$m) and absorption corrected 2-10 keV luminosities for a sample of 8 Seyfert galaxies. Lutz et al. (2004) evaluated the correlation for a sample of 71 AGN, observed with the ISOPHOT instrument aboard the Infrared Space Observatory (ISO). They found the dispersion of the correlation to be much larger than expected. Moreover, in both studies, no difference in the luminosity ratio $L_{\mathrm{MIR}}/L_{\mathrm{X}}$ between type I and type II AGN could be found. The results by Lutz et al. are shown in fig. 2.7.

The infrared luminosities used by Lutz et al., suffer from the large aperture ($24'' \times 24''$) of the ISOPHOT instrument. Thus, the large observed scatter in the correlation may be induced by extra-nuclear emission contaminating their flux measurements. Furthermore, such contamination could also hide the difference between the Sy types.

In order to avoid the problems Lutz et al. encountered when it comes to interpreting their data, we aimed to explore the mid-IR – hard X-ray correlation with the highest possible angular resolution in the MIR and, thus, minimise contamination. We decided to use archival X-ray data of nearby AGN and observe these with MIR instruments mounted at 8m-class telescopes. Therefore, two observing campaigns using the VISIR instrument at Unit Telescope 3 of ESO's Very Large Telescope (VLT) were undertaken. Both proved to be successful and provided us with MIR photometric data of high quality. These data were used to constrain the geometry of the dusty torus in AGN.

3 Observing Techniques

Zapp Brannigan: Good work everyone; the mothership
is destroyed.

...

Zapp Brannigan: What the hell is that thing?
Kif: It appears to be the mothership ...
Zapp Brannigan: Then what did we just blow up?
Kif: The Hubble Telescope

Futurama, Season 1, Episode 12 (1999)

3.1 Observing in the mid-Infrared

Groundbased mid-IR observations face a number of special problems due to the physical properties of the Earth's atmosphere. The obvious way to overcome these is to make MIR observations from space. This, however, currently limits the achievable angular resolution to that of *Spitzer's* 85 cm mirror. In order to do better and, in particular, make use of the high angular resolution capabilities of today's 8-10 m class telescope's, special observing techniques have to be applied to deal with the problems imposed by our atmosphere.

Our atmosphere absorbs the majority of the MIR radiation from astronomical sources. The main absorbers are the molecules H_2O, CH_4, CO_2, O_2 and O_3. There are, however, two spectral windows between $8 - 13\,\mu$m and $16.5 - 24.5\,\mu$m, in which the atmosphere is rather transparent; these are called N- and Q-band, respectively. While the transmission in the N-band is fairly good at a dry site – especially between $10.5 - 12\,\mu$m – the atmosphere's transparency in the Q-band is rapidly decreasing with wavelength and can be viewed as a superposition of many sub-bands with a typical spectral coverage of $\Delta\lambda \approx 1\,\mu$m and transmissivity of 60%.

The atmosphere does not only absorb MIR photons from astronomical objects but also emits a strong thermal background. This background can be described as blackbody radiation with a temperature of roughly 253 K. Also contributing to the background is the telescope itself which, in case of the VLT, radiates at about 283 K. To avoid internal background, MIR instruments have to be cooled. The VISIR instrument is operated at 33 K, its detectors at $\sim 4 - 6$ K, depending on the actual instrument setup.

The background is actually much stronger than the flux of the astronomical object that is targeted in observations. In the N-band, the surface brightness of the sky is $m_N = 3700$ Jy/arcsec^2 which is equivalent to $\sim 10^8$ photons/s reaching the detector. In

order to avoid saturation, the detector integration time (DIT) has to be short,typically a few tens of milliseconds.

To make the astronomical target visible, the background has to be removed. This is done by **Chopping** and **Nodding**. The basic idea is to perform differential imaging. The chopping technique consists of taking two exposures, one on-source (target plus background) and one off-source (background only), and subsequently subtract one from the other. This has to be done faster than the rate of background variations. For VISIR, a chop frequency of 0.25 Hz for N-band and 0.5 Hz for Q-band imaging has been found to be adequate. Spectroscopic observations are performed with a chop frequency of 0.1 Hz.

In practice, chopping is usually achieved by moving the secondary mirror of the telescope. This, however, slightly changes the optical light path and the resulting residual background is suppressed by nodding. For that, the whole telescope is pointed off-source and the same chopping observations as on-source are repeated.

If the amplitude of chopping and nodding (these two are usually identical), the so called chop-throw, is chosen small enough, it is possible to gain another image of the astronomical target from the off-source position. In fact with a chop-throw smaller by a factor of two than the detector's field of view, one gets three (when chopping and nodding are done parallel to each other) or four (when done perpendicular) images of the same object. Of course, this reduces the effective field of view to one third and one forth of the detector's, respectively. Here caution is required when observing extended sources or objects in crowded fields. The result of this procedure is shown schematically in fig. 3.1.

3.2 The VISIR instrument[1]

The MIR instrument used for our programme, was the VLT spectrometer and imager for the mid–infrared (VISIR, see Lagage et al., 2004). The instrument is located at the Cassegrain focus of unit telescope (UT) 3, Melipal (see fig. 3.2). It provides diffraction-limited imaging at high sensitivity in the two mid-infrared atmospheric windows: the N band between $8 - 13\,\mu$m and the Q band between $16.5 - 24.5\,\mu$m. In addition, it features a long-slit spectrometer with a range of spectral resolutions between 150 and 30000.

3.2.1 Layout of the instrument

As VISIR is observing in the thermal infrared, it is a cryogenic instrument. The optical bench is enclosed in a vacuum vessel. Standard Giffor-McMahon closed-cycle coolers are used to maintain the required temperatures: 33 K for most of the optical system, < 15 K for the part close to the detectors and $\sim 4 - 6$ K for the detectors themselves.

Imager and spectrograph are two sub-instruments with independent lightpaths, optics and detectors. Both parts have an all-reflective optical design.

---

[1]This section is based on information provided on the VISIR webpage at ESO: http://www.eso.org/instruments/visir/ and in the VISIR User Manual (Smette & Vanzi, 2007).
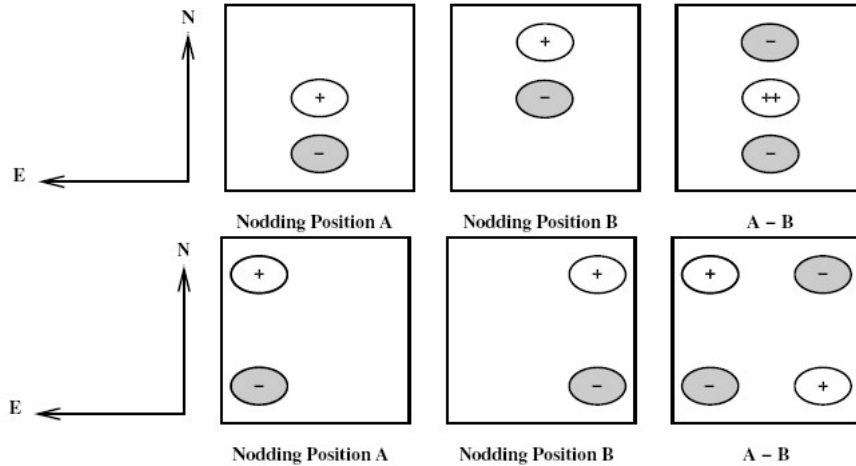
Figure 3.1: Schematic drawing of the content of a frame observed with chopping and nodding done parallel (top) and perpendicular (bottom). The arrows depict the North and East directions on the image; plus-signs indicate a positive flux, minus-signs a negative measured flux (resulting from the subtraction procedure). In each row, the two central panels show the two nodding half-cycle images in which the two different chopping positions have already been subtracted from each other. The panels on the right show the final frame of one complete chop-nod-cycle. Figure reproduced from Smette & Vanzi (2007).

The imager

The optical design of the imager – as shown in fig. 3.3 – consists of two parts, a collimator which provides an 18 mm diameter cold stop pupil in parallel light and a set of three objectives mounted on a wheel.

To avoid straylight and excessive background emission from the telescope structure, the pupil of the telescope is imaged on a cold stop mask. The collimator mirror (M1) is an aspherical mirror and is followed by a folding flat mirror (M2) which eases the mechanical implementation. The filter wheel is located just behind the pupil mask.

Two objectives – the intermediate field (IF) and small field (SF) objectives – are available on VISIR. Each of them is based on a three mirror anastigmatic (TMA) system with each of the TMAs being made of three conic mirrors.

The SF objective has a scale of $0.075''$/pixel and a field of view (fov) of $19.2'' \times 19.2''$. The IF objective's scale is $0.127''$/pixel with a fov of $32.5'' \times 32.5''$. The radius of the first Airy ring at $\lambda = 7.7\mu$m corresponds to $0.24''$ on the sky. This is the highest angular resolution achievable with VISIR.

For the N-band, ten narrow-band and one broad-band filters are offered. For the Q-band, three filters with intermediate widths can be used. The imager has some additional filters that have not been offered to the community yet.

The sensitivities of all offered filters are shown in fig. 3.4. Units are in mJy/h for a signal-to-noise ratio (S/N) of 10. For some filters, sensitivities close to the background limit can be achieved. Especially in the Q-band but also for some N-band filters, however,
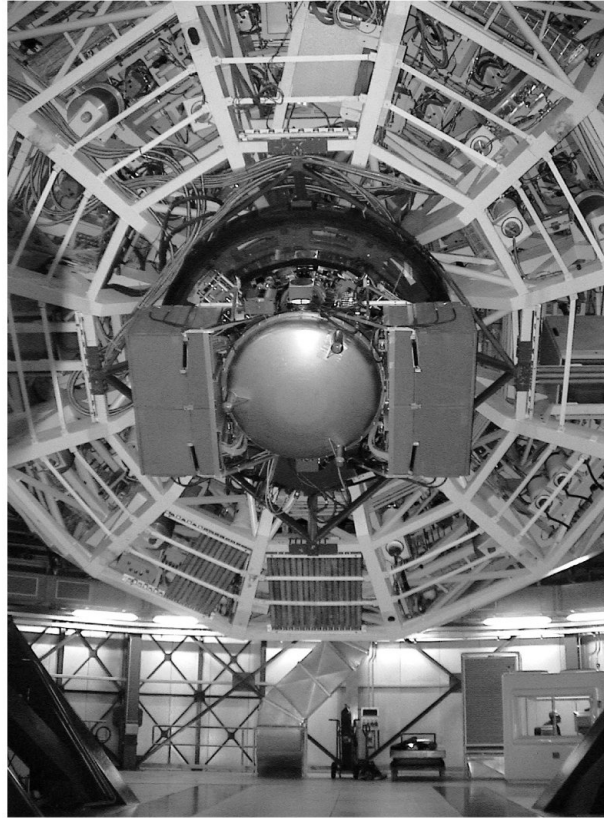
Figure 3.2: The VISIR instrument mounted at the Cassegrain focus of UT 3, Melipal. Image taken from ESO press release 13/2004: http://www.eso.org/public/outr rel/pr-2004/pr-13-04.html

VISIR Mounted behind the 8.2-m Mirror of Melipal

ESO PR Photo 16b/04 (12 May 2004)   © European Southern Observatory

the discrepancy between the theoretical limit and the observed sensitivity is quite large (up to a factor of 2). The most important factors for the sensitivity are atmospheric seeing and the amount of water vapour in the lower atmosphere. Therefore, observing during the "Bolivian winter" in February, when humid air flows down from the Altiplano toward Atacama desert, is not advisable.

The spectrograph

VISIR offers slit spectroscopy at three spectral resolutions, each with an angular scale of $0.127''$/pixel. The spectrograph has two arms – one with the low order gratings for the low and medium spectral resolution, the other with Echelle gratings for the high spectral resolution. In front of the slit wheel, a reflective re-imager consisting of two off-axis paraboloids and three folding flats is installed. The re-imager provides a 16 mm diameter cold stop pupil in parallel light and transforms the incoming VLT Cassegrain beam of F:13.4 to an F:10 beam at the spectrometer entrance.

The spectrometer has long slits and also short slits which are, however, only used in high resolution cross-dispersed mode. The long slits have a length of $32.5''$ covering the whole width of the detector, the short slits have a length of $4.1''$. The available slit widths are $0.4''$, $0.75''$ and $1''$. An additional slit with a width of $15.3''$ is used for target
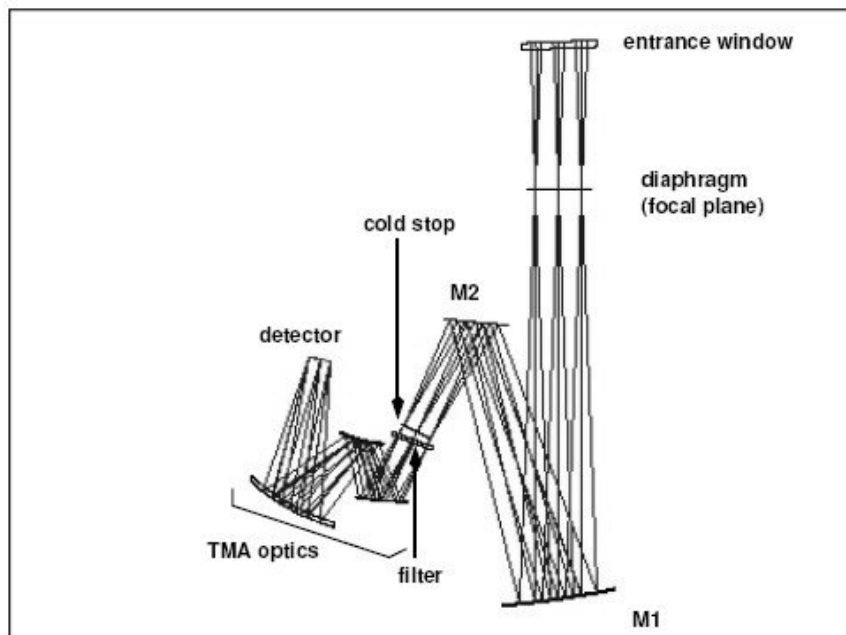
Figure 3.3: Optical design of the VISIR imager; the optical path is shown from the entrance window down to the detector. Figure reproduced from Smette & Vanzi (2007).

acquisition and centering on the detector.

The offered low resolution settings cover the whole N-band and provide a spectral resolution of ~ 300, the exact number depending on the chosen central wavelength. The medium resolution mode provides a resolution of ~ 3000; four settings in the N-band and one in the Q-band are offered. The high resolution mode offers long-slit settings centred on three narrow pass-bands (two in the N-band, one in the Q-band) and a total of 13 cross-dispersed settings (seven in the N-band and six in the Q-band); spectral resolutions vary between 11000 and 32000.

Detectors

Both imager and spectrograph are equipped with a 256×256 pixel detector. The quantum efficiency ranges between 50% to 65%. The temperature of the detectors is negligible compared to the background generated by the atmosphere and the telescope. Both effects are removed by chopping and nodding. Dark current residuals are at least 6 times lower than the photon noise for the spectrometer and negligible for the imager.

The detectors have a switchable pixel capacity. The large capacity ($1.8 \cdot 10^7$ e$^-$) is used for broad-band imaging, the small capacity ($1.9 \cdot 10^6$ e$^-$) for narrow-band imaging and spectroscopy. For background noise-limited performance, the detectors are best operated at half of the dynamic range for the large capacity and between 1/5 and 1/2 of the dynamic range for the small capacity.

The performance of the imaging system depends on the quality of the detector. While
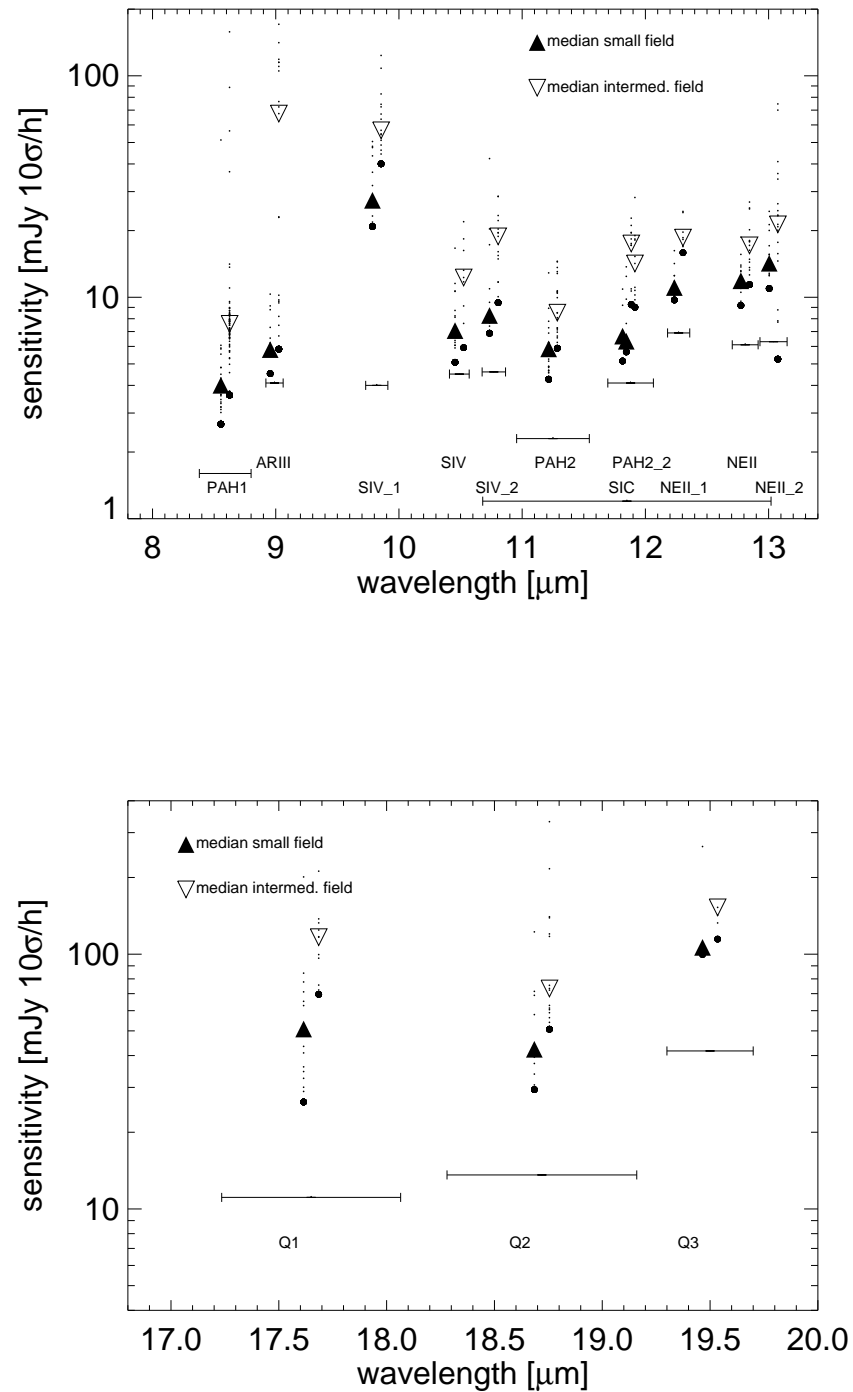
Figure 3.4: Sensitivities for VISIR imaging filters in the N-band (top) and Q-band (bottom). Units are in mJy/h for a signal-to-noise ratio of 10. Filled triangles depict median sensitivities for the SF objective, open triangles for the IF objective. Small dots show the sensitivities for individual observations, thick dots the best sensitivity ever achieved. Horizontal bars show the background noise limits for each filter. Their length corresponds to the filter's bandpass. Figure reproduced from Smette & Vanzi (2007).
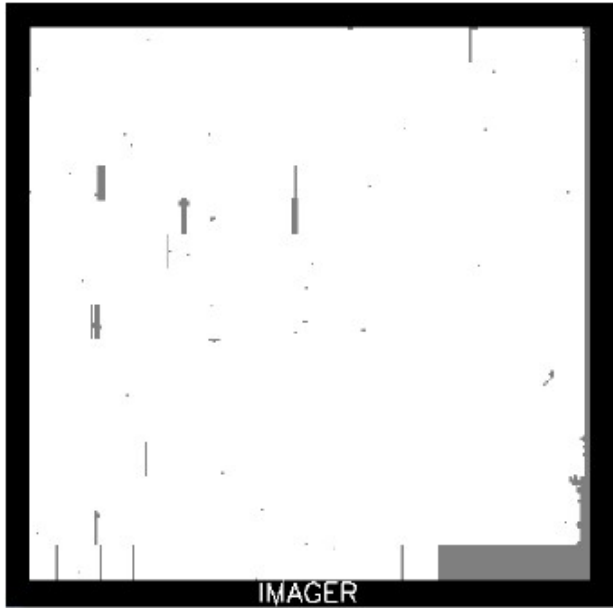
Figure 3.5: Bad pixel map of the imager. The large grey rectangular in the southwestern corner consists of pixels masked electronically in order to decrease detector striping and the appearance of ghosts. Figure reproduced from Smette & Vanzi (2007).

it has a reasonably low number of bad pixels ($< 2\%$), their positions are unfortunate for high precision photometry. Furthermore, the detector suffers from striping and the appearance of ghosts when observing bright targets.

The bad pixel map (fig. 3.5) shows that the Eastern side of the detector (assuming a Position Angle of 0) is heavily affected by bad pixels. The electronic ghost, on the other hand, usually appears on the Western side. The Southwestern corner of the detector has been electronically masked in order to decrease the ghost and also detector striping. This striping still appears when observing bright targets. As the minimum chop throw offered for VISIR is $8''$, it is virtually impossible to avoid all bad pixels and the ghost when using the SF objective. The consequences for our programme will be described in chapter 4.

3.2.2 Data acquisition

Both of the VISIR detectors are controlled by ESO's standard IRACE acquisition system. In imaging, up to 200 frames per second are read. This rate is too high to store every single frame; one image has a size of 256×256 pixels with 4 bytes per pixel, yielding 262 kB per read-out. Thus, during each chopping cycle the elementary exposures are added in real time and only the result is stored on disk.

Up to issue 80, the VISIR User Manual contained an incorrect equation for the total rejected time for one exposure. Therefore, the calculation is shown below. In issue 81, the error has been corrected.

A typical chopping frequency is $f_{\mathrm{chop}} = 0.25$ Hz. This means that one chopping half-cycle (i.e. the time spent in one chopping position) takes $T_{\mathrm{chop}} = 1/2 f_{\mathrm{chop}}^{-1} = 2$ s. One data file consists of all chopped images taken during one nodding position. For science observations, one nodding half-cycle usually takes $T_{\mathrm{nod}} = 90$ s. The number of images

stored in one data file then is

$$N_{\text{cyc\_chop}} \quad = \quad \frac{1}{2}\frac{T_{\text{nod}}}{T_{\text{chop}}} - N_{\text{skip\_chop}}, \tag{3.1}$$

where $N_{\text{skip\_chop}}$ is the number of chopping cycles dropped after each telescope movement due to stability issues. The number of nodding cycles $N_{\text{cyc\_nod}}$ is set according to the total integration time given by the observer.

Similarly to $N_{\text{skip\_chop}}$, a number $N_{\text{skip\_DIT}}$ of readouts at the beginning of each chopping position is ignored. When T_{DIT} is the time for one single exposure, the number of stacked images for one chopping position is

$$N_{\text{DIT}} \quad = \quad (2T_{\text{DIT}}f_{\text{chop}})^{-1} - N_{\text{skip\_DIT}}. \tag{3.2}$$

This yields a total on-source integration time of

$$T_{\text{source}} \quad = \quad 2N_{\text{cyc\_nod}}N_{\text{cyc\_chop}}N_{\text{DIT}}T_{\text{DIT}} \tag{3.3}$$

and a total rejected time of

$$T_{\text{skip}} \quad = \quad 2N_{\text{cyc\_nod}}T_{\text{DIT}}\left(N_{\text{skip\_DIT}}N_{\text{cyc\_chop}} + N_{\text{skip\_chop}}N_{\text{DIT}}\right) \tag{3.4}$$

The duty cycle $T_{\text{source}}/(T_{\text{source}} + T_{\text{skip}})$ is typically around 70 %. This has to be taken into account when applying for and planning observing runs with VISIR.

4 Our VISIR imaging campaign

> *While "pleasure" and "enjoyment" are often used to characterize one's efforts in science, failures, frustration and disappointments are equally, if not the more, common ingredients of scientific experience. Overcoming difficulties, undoubtly, contributes to one's final enjoyment of success. Is failure, then, a purely negative aspect of the pursuit of science?*

> Subrahmanyan Chandrasekhar: The Pursuit of Science: Its Motivations (1985)

4.1 Target selection and X-ray data

The targets for our first sample of objects (listed in table 4.1) were selected from the sample by Lutz et al. (2004). Our criteria were (1) observability at low airmass from Paranal observatory during ESO period P75, (2) redshifts below 0.1 and (3) coverage of a wide span of hard X-ray luminosities in both type I and type II objects.

For our second sample of objects (listed in table 4.2), we also selected targets not included in the Lutz et al. sample. We browsed the literature for relatively nearby AGN ($z \leq 0.1$) with inferred absorption-corrected hard X-ray luminosities that are observable at low airmass from Paranal observatory during ESO period P77. An additional criterion was the inclination of the host galaxy toward the plane of the sky. We set the limit at an inclination angle of $i = 65°$ in order to avoid viewing the AGN through large amounts of gas in the host galaxy. Note that two objects from our first sample – NGC 526a and NGC 7314 – do not meet this requirement. The classification of all AGN in our sample has been done according to Véron-Cetty & Véron (2006) with the exception of NGC 4303 (see section 4.1.3) and Cen A which is listed as a possible BL Lac object but is commonly referred to as an optical type 2 AGN. For the subsequent statistical analysis, we summarise Sy types 1.0, 1.2 and 1.5 as "type I" and Sy types 1.8, 1.9, 2.0 and 1h as "type II". Note that Véron-Cetty & Véron (2006) use the designation "Sy 3.0" for galaxies harbouring low ionisation nuclear emission regions (LINER).

For our target selection, we had to search the literature for AGN with inferred 2-10 keV luminosities. Observations at different epochs were taken as an indicator for the intrinsic variability of the object. This task requires a lot of care as X-ray observations can be of very varying quality, especially if other telescopes than *Chandra* and XMM-*Newton* are involved. Furthermore, different authors sometimes pursue different strategies for

fitting the observed data. In general, we give higher priority to recent data obtained with state-of-the-art telescopes.

In the following, I will discuss the hard X-ray properties of our targets from both samples. We have converted all luminosities to the cosmology employed in this work: $H_0 = 73$ km s^{-1} Mpc^{-1}, $\Omega_\Lambda = 0.72$ and $\Omega_m = 0.24$ (Spergel et al., 2006). For some very nearby AGN, the redshift is a poor indicator for the distance. In these cases, we use other distance estimates (e.g. form variable stars, the red giant branch, the Tully-Fisher relation). Whenever this is the case, it is stated in the text. Furthermore, we account for a distance uncertainty of 10% in all luminosities.

Where multi-epoch observations are not available, we assume a variability / uncertainty of a factor of 2 (0.3 dex). Formal errors to the X-ray luminosities are not stated here as these are only used in logarithmic units. See tables 4.1 and 4.2 for logarithmic luminosities and uncertainties. Please note that all 2-10 keV fluxes discussed here have been corrected for absorption.

4.1.1 X-ray data for the P75 sample

Fairall 9: With XMM-*Newton*, Gondoin et al. (2001) measured a hard X-ray flux of $F_{2-10\,\text{keV}} = (1.56 \pm 0.33) \cdot 10^{-11}$ erg s^{-1} cm^{-2}. From the compilation of earlier measurements shown in their paper, we can estimate the peak-to-peak variability / uncertainty to be of the order of 2. Most earlier observations yield a higher X-ray flux which may be due to the poor angular resolution of the first X-ray satellites. One observation from October 1984 yields a lower flux than the one obtained with XMM-*Newton*, but still within the assumed uncertainty. Yaqoob & Padmanabhan (2004) report a flux of $F_{2-10\,\text{keV}} = 2.2 \cdot 10^{-11}$ erg s^{-1} cm^{-2}, obtained with *Chandra*. Within errors, this is still consistent with Gondoin et al.'s measurement. From these fluxes we calculate a luminosity of $L_{2-10\,\text{keV}} = 7.43 \cdot 10^{43}$ erg s^{-1}. The reported hydrogen column density is $N_\text{H} = (3.0 \pm 0.2) \cdot 10^{20}$ cm^{-2}.

NGC 526a: Unfortunately, for this object no observations with *Chandra* or XMM-*Newton* have been published. Using *Beppo*SAX, Landi et al. (2001) measured $F_{2-10\,\text{keV}} = 1.8 \cdot 10^{-11}$ erg s^{-1} cm^{-2}, absorbed by $N_\text{H} = (1.33 \pm 0.15) \cdot 10^{22}$ cm^{-2}. Due to the observing capabilities at very high X-ray energies (2-100 keV) of *Beppo*SAX, the obtained fit is more reliable than the ones derived from ASCA and *Ginga* data (see Landi et al. 2001 for references).

Another observation of NGC 526a with the RXTE satellite has been performed by Revnivtsev et al. (2004). Extrapolating their 2-9 keV countrate yields $F_{2-10\,\text{keV}} = 2.7 \cdot 10^{-11}$ erg s^{-1} cm^{-2}. Both observations are consistent with each other if we assume an uncertainty of 0.2 dex. The resulting luminosity is $L_{2-10\,\text{keV}} = 1.37 \cdot 10^{43}$ erg s^{-1}.

NGC 3783: This object was observed with XMM-*Newton* by Blustin et al. (2002) who report an intrinsic flux of $F_{2-10\,\text{kev}} = 8.5 \cdot 10^{-11}$ erg s^{-1} cm^{-2} which corresponds to $L_{2-10\,\text{kev}} = 1.61 \cdot 10^{43}$ erg s^{-1}. The Galactic absorption toward NGC 3783 is $N_\text{H} = 8.7 \cdot 10^{20}$ cm^{-2}. The intrinsic warm absorption can be ignored for our purpose as it hardly affects the 2-10 keV band. Using the same measurements from Blustin et al., Shinozaki

et al. (2006) derive a luminosity of $L_{2-10\,\mathrm{keV}} = 8.7 \cdot 10^{42}$ erg s^{-1} – a result I am unable to reproduce.

Variability of this source is indicated by comparing the flux given above to the one reported by Malizia et al. (1997) ($F^{\mathrm{obs}}_{2-10\,\mathrm{keV}} = 4.09 \cdot 10^{-10}$ erg s^{-1}) which is about five times higher. Please note that the luminosity these authors report is not reliable. Not only do they use outdated cosmological parameters but also an incorrect redshift for NGC 3783. As their data is of high quality, we will use the results from Blustin et al. (2002) and allow for a variability / uncertainty of 0.3 dex.

NGC 4579: This object has been observed multiple times (Terashima et al., 1998; Ho et al., 2001; Dewangan et al., 2004; Cappi et al., 2006) with most of the results being in good agreement with each other. We here adopt the results of Cappi et al. – $L_{2-10\,\mathrm{keV}} = 1.26 \cdot 10^{41}$ erg s^{-1}, $N_{\mathrm{H}} \leq 2 \cdot 10^{20}$ cm^{-2} – which were obtained with XMM-*Newton*. The luminosity stated by Dewangan et al. (2004) is lower by factor of 10. This, however, seems to be a typographical error as all measured fluxes are consistent. A statistical uncertainty of 0.3 dex is assumed to account for the different results on $L_{2-10\,\mathrm{keV}}$ among the other authors.

NGC 4593: The two most reliable datasets for this object are from Reynolds et al. (2004) and Shinozaki et al. (2006), both obtained with XMM-*Newton*. They agree within errors. We adopt the values provided by Shinozaki et al.: $N_{\mathrm{H}} = 1.69 \cdot 10^{20}$ cm^{-2} and $L_{2-10\,\mathrm{keV}} = 8.60 \cdot 10^{42}$ erg s^{-1}. Steenbrugge et al. (2003) observed NGC 4593 with both XMM-*Newton* and *Chandra*. While the *Chandra* result ($L_{2-10\,\mathrm{keV}} = 8.91 \cdot 10^{42}$ erg s^{-1}) is in good agreement with the one cited above, the luminosity measured with XMM-*Newton* is higher ($L_{2-10\,\mathrm{keV}} = 1.2 \cdot 10^{43}$ erg s^{-1}). This may be due to intrinsic variability

Table 4.1: Characterisation of our galaxy sample for P75. Heliocentric redshifts z were taken from the NED, Seyfert types are according to Véron-Cetty & Véron (2006) and the inclination angles i of the host galaxies on the sky were taken from the Hyperleda database (Paturel et al., 2003). The absorption-corrected hard X-ray luminosities and intrinsic column densities have been compiled from the literature (see section 4.1.1 for details). The last column contains the physical scales resolved by VISIR, computed for an angular resolution of 0.35″, which is a typical value for our observations (see section 4.2).

Object	z	Sy	i	$\log L_{2-10\,\mathrm{keV}}$ [erg/s]	N_{H} [10^{21} cm^{-2}]	Scale [pc]
Fairall 9	0.047	1.2	55.7°	43.87 ± 0.15	0.3 ± 0.02	320
NGC 526a	0.019	1.9	74.0°	43.14 ± 0.10	1.33 ± 0.15	135
NGC 3783	0.010	1.5	29.9°	43.21 ± 0.15	n/a	70
NGC 4579	0.005	3.0	39.0°	41.10 ± 0.15	≤ 0.2	35
NGC 4593	0.009	1.0	36.0°	42.93 ± 0.20	0.169	65
PKS 2048-57	0.011	1h	48.4°	42.84 ± 0.20	237 ± 20	80
PG 2130+099	0.062	1.5	63.0°	43.65 ± 0.20	n/a	415
NGC 7314	0.005	1h	70.3°	42.20 ± 0.15	7.2 ± 1.0	35

of the source. We can account for this with an uncertainty of 0.4 dex.

PKS 2048-57: Risaliti et al. (2002), observing with ASCA, inferred $N_H = (2.37 \pm 0.20) \cdot 10^{23}$ cm^{-2} and $F_{2-10\,keV} = 2.65 \cdot 10^{-11}$ erg s^{-1} cm^{-2}, the latter yielding $L_{2-10\,keV} = 6.88 \cdot 10^{42}$ erg s^{-1}. An independent analysis of archival ASCA data by Heckman et al. (2005) yields $L_{2-10\,keV} = 2.88 \cdot 10^{42}$ erg s^{-1}, after conversion to our cosmology. These results are consistent if we consider variability of the source: Georgantopoulos & Papadakis (2001) report a flux variation by a factor of almost two within one week of observation. For our study we use the results by Risaliti et al., allowing for a luminosity uncertainty of 0.4 dex.

PG 2130+099: Lawson & Turner (1997) find this object to be unabsorbed and emit $F_{2-10\,keV} = 5.3 \cdot 10^{-12}$ erg s^{-1} cm^{-2} and, thus, $L_{2-10\,keV} = 4.50 \cdot 10^{43}$ erg s^{-1}. More recently, Gallo (2006) observed PG 2130+099 with XMM-*Newton* and obtained $F_{2.5-10\,keV} = 3.1 \cdot 10^{-12}$ erg s^{-1} cm^{-2}. If we use the luminosity value from Lawson & Turner and assume an uncertainty of 0.4 dex, this will be in good agreement with Gallo's result.

NGC 7314: This object was observed with XMM-*Newton* by Shinozaki et al. (2006). After converting their result to our cosmology, we get $L_{2-10\,keV} = 1.5 \cdot 10^{42}$ erg s^{-1} and a column density of $N_H = (7.2 \pm 1.0) \cdot 10^{21}$ cm^{-2}. Older observations by Malizia et al. (1997); Turner et al. (1997); Risaliti (2002); Risaliti et al. (2002); Kraemer et al. (2004) are in good agreement with these numbers if one accounts for the different cosmological parameters used.

4.1.2 X-ray data for the P77 sample

MCG-01-01-043: This object was observed with ASCA by Turner et al. (1997). They report $N_H = 3.27^{+2.74}_{-0.0} \cdot 10^{20}$ cm^{-2} and a luminosity that – corrected for the different cosmologies – translates to $L_{2-10\,keV} = 3.5 \cdot 10^{42}$ erg s^{-1}. Please note that Turner et al. state that there is a slight ambiguity in the source identification. Fortunately, this measurement is backed up by INTEGRAL observations (Ebisawa et al., 2003). JEM-X measures $F_{3-10\,keV} = 1.55 \cdot 10^{12}$ erg s^{-1} cm^{-2}. This yields $L_{3-10\,keV} = 2.84 \cdot 10^{42}$ erg s^{-1}. Thus, we can safely assume the results of Turner et al. to be valid.

Mrk 590: With XMM-*Newton*, Gallo et al. (2006) estimated a 2-10 keV luminosity which, in our cosmology, yields $L_{2-10\,keV} = 6.6 \cdot 10^{42}$ erg s^{-1}. This is in good agreement with the results of a combined *Chandra* and XMM-*Newton* programme by Longinotti et al. (2007) ($L_{2-10\,keV} = 8.9 \cdot 10^{42}$ erg s^{-1}). Shinozaki et al. (2006), on the other hand, having observed Mrk 590 with XMM-*Newton* as well, report a luminosity of $L_{2-10\,keV} = 4.1 \cdot 10^{43}$ erg s^{-1} (after conversion to our cosmology).

For this work we will use Longinnotti et al.'s result and allow for an uncertainty of 0.5 dex.

NGC 1097: Iyomoto et al. (1996) observed this object with ASCA and obtained $N_H = 1.3^{+0.4}_{-0.3} \cdot 10^{21}$ cm^{-2} and $F_{2-10\,keV} = 1.7 \cdot 10^{-12}$ erg s^{-1} cm^{-2}, the latter corresponding

to $L_{2-10\,\mathrm{keV}} = 6.18 \cdot 10^{40}$ erg s^{-1}.

In the compilation by Strateva et al. (2006), a luminosity of $L_{2-10\,\mathrm{keV}} = 0.00668 \cdot 10^{42}$ erg s^{-1} is stated, the source of the data being a *Chandra* observation by M. Eracleous that has not been published yet. The discrepancy to the result of Iyomoto et al. is one order of magnitude. It seems likely, however, that the number given in Strateva et al.'s paper is simply a typo: M. Eracleous is not only a co-author of their paper, but also of another one by Nemmen et al. (2006) who also observed NGC 1097 with *Chandra* and report $N_{\mathrm{H}} = 2.3^{+2.8}_{-1.7} \cdot 10^{20}$ cm^{-2} and $F_{2-10\,\mathrm{keV}} = 1.73 \cdot 10^{-12}$ erg s^{-1} cm^{-2} and, thus, the exact same flux as Iyomoto et al.

As results from *Chandra* are generally more reliable than those from ASCA, we will adopt the values from Nemmen et al. for our analysis.

NGC 4303: This low-luminosity AGN was observed by Jiménez-Bailón et al. (2003), using the *Chandra* telescope. The nuclear source does not show intrinsic absorption. Thus, the the Galactic value of $N_{\mathrm{H}} = 1.67 \cdot 10^{20}$ cm^{-2} is adopted. The unabsorbed flux is $F_{2-10\,\mathrm{keV}} = 2.6^{+1.0}_{-0.8} \cdot 10^{-14}$ erg s^{-1} cm^{-2}. This corresponds to a luminosity of $L_{2-10\,\mathrm{keV}} = 1.44 \cdot 10^{39}$ erg s^{-1}. Please note that Jiménez-Bailón et al. (2003) cannot exclude the possibility that the nuclear X-ray source of NGC 4303 is an X-ray binary system instead of an AGN. They come, however, to the conclusion that this is unlikely.

NGC 4472: This object, unfortunately, has not been detected in the hard X-ray band so far and was erroneously included in our sample. The most stringent upper limit to its flux is from Panessa et al. (2006): $F_{2-10\,\mathrm{keV}} \leq 6.6 \cdot 10^{-14}$ erg s^{-1} cm^{-2}. The corresponding luminosity limit is $L_{2-10\,\mathrm{keV}} \leq 1.48 \cdot 10^{39}$ erg s^{-1}. This is in agreement with the 3σ detection in the soft band by Soldatenkov et al. (2003) who measured $L_{0.5-2.5\,\mathrm{keV}} = 1.7 \cdot 10^{38}$ erg s^{-1}. Whether this source is dominated by a star-burst or suffers from Compton-thick absorption is still under investigation.

NGC 4507: For this object the estimates for the hydrogen column density vary a lot. The highest value ($N_{\mathrm{H}} = 4.9 \cdot 10^{23}$) is given by Malizia et al. (1997). Some of the same authors (Bassani et al., 1999) later estimated $N_{\mathrm{H}} = (2.92 \pm 0.23) \cdot 10^{23}$. Here, we adopt the latter value as it is also a good average of the different published column densities. The resulting absorption-corrected flux is $F_{2-10\,\mathrm{keV}} = 7.03 \cdot 10^{-11}$ erg s^{-1} cm^{-2}. This yields $L_{2-10\,\mathrm{keV}} = 2.00 \cdot 10^{43}$ erg s^{-1}. We assume an uncertainty of 0.3 dex which matches the variability observed by Georgantopoulos & Papadakis (2001).

NGC 4698: Three *Chandra* observations of this object have been published, by Cappi et al. (2006), González-Martín et al. (2006) and Panessa et al. (2006). Cappi et al. report $N_{\mathrm{H}} \leq 4 \cdot 10^{21}$ cm^{-2} and $L_{2-10\,\mathrm{keV}} = 1.59 \cdot 10^{39}$ erg s^{-1}. If we use the distance to NGC 4698 from Tully (1988) which was also used by Cappi et al., the flux measurements by Panessa et al. and González-Martín et al. yield $L_{2-10\,\mathrm{keV}} = 1.54 \cdot 10^{39}$ erg s^{-1} and $L_{2-10\,\mathrm{keV}} = 4.90 \cdot 10^{38}$ erg s^{-1}, respectively. As all three observations seem to be of comparable quality we adopt a mean luminosity of $L_{2-10\,\mathrm{keV}} = 1.21 \cdot 10^{39}$ erg s^{-1} and an uncertainty of 0.6 dex.

NGC 4941: Maiolino et al. (1998) present *Beppo*SAX observations of this object.

Their best fit results are $N_{\rm H} = 4.5^{+2.5}_{-1.4} \cdot 10^{23}$ cm^{-2} and $L_{2-10\,{\rm keV}} \approx 2 \cdot 10^{41}$ erg s^{-1}. Risaliti (2002) complements the *Beppo*SAX data with ASCA observations. He draws the conclusion that the absorbing column is actually Compton-thick. Terashima et al. (2002) also find $N_{\rm H} \sim 10^{24}$ cm^{-2} and attribute the difference between their and Maolino et al.'s result to variability of the absorbing column. Since NGC 4941 has not been observed by X-ray telescopes recently, we have to use the estimate by Maiolino et al. We consider the uncertainty of this luminosity estimate to be large and set it to 0.6 dex.

IRAS 13197-1627: The most recent X-ray observation using XMM-*Newton* is by Miniutti et al. (2007). They report a hydrogen column density of $N_{\rm H} = (3.9 \pm 0.4) \cdot 10^{23}$ cm^{-2}. If we convert the absorption-corrected luminosity they infer to our cosmology, we get $L^{\rm obs}_{2-10\,{\rm keV}} = (0.6 \pm 0.2) \cdot 10^{43}$ erg s^{-1}. Miniutti et al. also estimate the true intrinsic luminosity of the AGN by multiplying the reflection fraction. After correcting for the different cosmologies, it is $L^{\rm int}_{2-10\,{\rm keV}} = (3.9 \pm 2.6) \cdot 10^{43}$ erg s^{-1}. The first value is also consistent with $L_{2-10\,{\rm keV}} = 0.37 \cdot 10^{43}$ erg s^{-1} as resulting from the flux reported by Bassani et al. (1999) – even though these authors assumed a much higher column density of $N_{\rm H} = (7.6 \pm 1.3) \cdot 10^{23}$ cm^{-2}. For our further analysis. we will adopt Miniutti et al.'s estimate for $L^{\rm obs}_{2-10\,{\rm keV}}$ and take the conservative assumption of an uncertainty of 0.4 dex.

Cen A: Observations with *Chandra* and XMM-*Newton* by Evans et al. (2004) yield an absorbing column density of $N_{\rm H} \approx 10^{23}$ cm^{-2} and an intrinsic luminosity of $L_{2-10\,{\rm keV}} = 4.80 \cdot 10^{41}$ erg s^{-1} with a peak-to-peak variability by a factor of $\lesssim 2$. This is consistent with older estimates by Grandi et al. (2003) ($F_{2-10\,{\rm kev}} = 3.8 \cdot 10^{-10}$ erg s^{-1} cm^{-2}, yielding $L_{2-10\,{\rm keV}} = 6.71 \cdot 10^{41}$ erg s^{-1}) and Risaliti (2002) ($N_{\rm H} \approx 9 \cdot 10^{22}$ cm^{-2}). Malizia et al. (1997) estimated a very different luminosity of $1.6 \cdot 10^{43}$ erg s^{-1}. This discrepancy is mainly due to the incorrect distance of 12 Mpc used by these authors (this issue is discussed in subsection 4.1.3). Therefore, we adopt the luminosity from Evans et al. and the absorbing column density from Risaliti.

NGC 5135: Bassani et al. (1999) reanalysed ASCA data recorded by Turner et al. (1997) who reported $N_{\rm H} = 4.7^{+7.6}_{-0.0} \cdot 10^{20}$ cm^{-2} and $F_{2-10\,{\rm keV}} = 2.0 \cdot 10^{-13}$ erg s^{-1} cm^{-2}, and come to the conclusion that the object is likely to be Compton-thick. This is in disagreement to the analysis made by Turner et al. More recently, Levenson et al. (2004) observed NGC 5135 with *Chandra*. They find $N_{\rm H} > 10^{24}$ cm^{-2}. From the flux of the Iron Kα line they estimate the intrinsic hard X-ray luminosity to be $L_{2-10\,{\rm keV}} \approx 1 \cdot 10^{43}$ erg s^{-1}.

Since Bassani et al. and Levenson et al., as well as Guainazzi et al. (2005) agree that NGC 5135 is obscured by Compton-thick material, we will use the numbers from Levenson et al. (2004). To account for the high uncertainty of the luminosity estimate, we will set it to 1.0 dex.

MCG-06-30-015: This source has been extensively studied due to its prominent, relativistically-broadened Iron Kα line (e.g. Tanaka et al., 1989; Fabian et al., 2003). A dusty warm absorber with an equivalent neutral column density of a few 10^{21} cm^{-2} is known to be present (Reynolds et al., 1997; Lee et al., 2001). Extrapolating the latest 3–45 keV Suzaku X-ray data (Miniutti et al., 2007) to 2–10 keV results in an intrinsic

power-law luminosity of $L_{2-10\,\mathrm{keV}} = 3.7 \cdot 10^{42}$ erg s^{-1}. The source is known to vary significantly. Therefore, we have used time-averaged measurements for the above calculation and also assign a variability / uncertainty of 0.4 dex. This is consistent with an INTEGRAL/JEM-X measurement by Beckmann et al. (2006). For the column density, we adopt the equivalent value from Reynolds et al. (1997), $N_{\mathrm{H}} = (3.5 \pm 1.1) \cdot 10^{21}$ cm^{-2} which was calculated from optical reddening.

NGC 5995: This object was observed by Panessa & Bassani (2002), using the ASCA satellite. They find $N_{\mathrm{H}} = 9.0^{+0.5}_{-0.3} \cdot 10^{21}$ cm^{-2} and (after conversion to our cosmology) $L_{2-10\,\mathrm{keV}} = 3.48 \cdot 10^{43}$ erg s^{-1}.

ESO 141-G55: This object was observed with XMM-*Newton* by Gondoin et al. (2003). They find the absorption to be Galactic with $N_{\mathrm{H}} = 5.5 \cdot 10^{20}$ cm^{-2}. After we correct the luminosity they determined for the slightly different redshift and cosmological parameters we use, we end up with $L_{2-10\,\mathrm{keV}} = 8.01 \cdot 10^{43}$ erg s^{-1}.

Mrk 509: Shinozaki et al. (2006) observed this AGN with XMM-*Newton* and find an intrinsic absorption of $N_{\mathrm{H}} \leq 4.8 \cdot 10^{20}$ cm^{-2} and (after correcting for slightly different cosmology and redshift) $L_{2-10\,\mathrm{keV}} = 1.3 \cdot 10^{44}$ erg s^{-1}. Using *Chandra*, Yaqoob & Padmanabhan (2004) observed Mrk 509 and find (again, after converting to our cosmology) $L_{2-10\,\mathrm{keV}} = 1.3 \cdot 10^{44}$ erg s^{-1}, as well. Since the flux measured by these authors is larger than the one observed by Shinozaki et al. by a factor of 1.5, it seems as if they fitted a somewhat different absorbing column density. Nevertheless the agreement between these two analyses is very good; we will thus use the numbers given by Shinonzaki et al.

NGC 7172: Intrinsic luminosity and column density estimates for this source show a surprising range of variation. From *Beppo*SAX observations, Dadina (2007) infers $N_{\mathrm{H}} = 1.1 \cdot 10^{21}$ cm^{-2} (although this seems to be underestimated by a factor of 100 due to a typographical error) and $F_{2-10\,\mathrm{keV}} = 8.9 \cdot 10^{-12}$ erg s^{-1} cm^{-2}, yielding $L_{2-10\,\mathrm{keV}} = 1.33 \cdot 10^{42}$ erg s^{-1}. Awaki et al. (2006), on the other hand, report $N_{\mathrm{H}} = (8.3 \pm 0.2) \cdot 10^{22}$ cm^{-2} and $L_{2-10\,\mathrm{keV}} = 5.8 \cdot 10^{42}$ erg s^{-1}.

Risaliti et al. (2002) compiled observations of NGC 7172 that had been executed between 1985 and 1997. Column densities range between $(7 - 11) \cdot 10^{22}$ cm^{-2} and absorption corrected fluxes between $(0.9 - 7.7) \cdot 10^{-11}$ erg s^{-1} cm^{-2} with a weak trend toward lower fluxes with time. For our study we adopt the results of Awaki et al. as they are intermediate ones.

A high variability of NGC 7172 in the hard X-ray band has been observed by Georgantopoulos & Papadakis (2001) who report a flux variation by a factor of ~ 6 within one week of observation. To account for this we set the uncertainty to 0.8 dex.

NGC 7213: This object has been observed repeatedly by X-ray satellites. The most recent results are by Starling et al. (2005) from XMM-*Newton* observations (Galactic $N_{\mathrm{H}} = 2.04 \cdot 10^{20}$ cm^{-2}, $L_{2-10\,\mathrm{keV}} = 1.7 \cdot 10^{42}$ erg s^{-1}), Zhou & Wang (2005), re-analysing archival XMM -*Newton* data ($L_{2-10\,\mathrm{keV}} = 1.68 \cdot 10^{42}$ erg s^{-1}) and Bianchi et al. (2004) who performed simultaneous observations with XMM-*Newton* and *Beppo*SAX ($N_{\mathrm{H}} = 2.04 \cdot 10^{20}$ cm^{-2}, $L_{2-10\,\mathrm{keV}} = 1.72 \cdot 10^{42}$ erg s^{-1}). The agreement of these studies

is very good. We will use the arithmetic mean of these three luminosity estimates.

3C 445: The three most recent observations of 3C 445 were all carried out with XMM-*Newton*; Shinozaki et al. (2006) measured $N_{\mathrm{H}} = 1.32^{+0.1}_{-0.2} \cdot 10^{23}$ cm^{-2} and – in our cosmology – $L_{2-10\,\mathrm{keV}} = 2.6 \cdot 10^{44}$ erg s^{-1}. Grandi et al. (2007) find $N_{\mathrm{H}} = 4^{+3}_{-2} \cdot 10^{23}$ cm^{-2} and an unabsorbed flux of $F_{2-10\,\mathrm{keV}} = 1.7 \cdot 10^{-11}$ erg s^{-1} cm^{-2} which translates to $L_{2-10\,\mathrm{keV}} = 1.2 \cdot 10^{44}$ erg s^{-1}. The observations by Sambruna et al. (2007) yield $N_{\mathrm{H}} = 2.25^{+0.62}_{-0.43} \cdot 10^{23}$ cm^{-2} and, after conversion to our cosmology, $L_{2-10\,\mathrm{keV}} = 8.1 \cdot 10^{43}$ erg s^{-1}. Given the complexity of the source (see section 4.1.3 for details), these numbers agree very well. We therefore use the mean values.

NGC 7469: From XMM-*Newton* observations Zhou & Wang (2005) derive a luminosity of $L_{2-10\,\mathrm{keV}} = 1.29 \cdot 10^{43}$ erg s^{-1}. NGC 7469 was also observed with *Chandra* by Jiang et al. (2006) who find a purely Galactic absorption of $N_{\mathrm{H}} = 4.9 \cdot 10^{20}$ cm^{-1}. After correcting for the different cosmology we use as well as for a slightly different redshift, the luminosity they estimate translates to $L_{2-10\,\mathrm{kev}} = 1.46 \cdot 10^{43}$ erg s^{-1}. This is in good agreement with the result of Zhou & Wang.

Scott et al. (2005) observed this object simultaneously in the X-rays and UV domains with *Chandra*, FUSE and STIS. They do not state a 2-10 keV flux in their paper. Using the power law model shown in their figure 1, however, we derive $F_{2-10\,\mathrm{keV}} = 2.46 \cdot 10^{-11}$ erg s^{-1} cm^{-2}. This, in turn, yields $L_{2-10\,\mathrm{keV}} = 1.45 \cdot 10^{43}$ erg s^{-1}.

As these three observations agree very well with each other, we will use the mean luminosity and set the uncertainty to 0.2 dex.

NGC 7674: This object appears to be Compton-thick. Malaguti et al. (1998) suggest an intrinsic luminosity of $L_{2-10\,\mathrm{keV}} \approx 10^{45}$ erg s^{-1}. For their estimate they assume the electron scattering material to have the same geometry as in the prototypical Seyfert 2 galaxy NGC 1068. Correcting for the different cosmology they use, decreases this number to $\sim 4.4 \cdot 10^{44}$ erg s^{-1}.

Another way to estimate the intrinsic 2-10 keV luminosity is via the correlation between the $\lambda 5007$ [OIII] and 2-10 keV fluxes. This correlation was recently refined by Panessa et al. (2006) who reported $\log F_{2-10\,\mathrm{keV}} - \log F_{[\mathrm{OIII}]} \approx 1.74$. Dahari & De Robertis (1988) measured a flux of $F_{[\mathrm{OIII}]} = 4.3 \cdot 10^{-13}$ erg s^{-1} cm^{-2}. Bassani et al. (1999) corrected this result for intrinsic absorption and obtained $F^{\mathrm{int}}_{[\mathrm{OIII}]} = (1.85 \pm 0.1) \cdot 10^{-12}$ erg s^{-1} cm^{-2} from which, in turn, we obtain $L_{2-10\,\mathrm{keV}} = 1.8 \cdot 10^{44}$ erg s^{-1}.

The result obtained from the [OIII] flux is in good agreement with the estimate by Malaguti et al., especially regarding the somewhat speculative nature of both methods. However, Bassani et al.'s absorption correction of the $\lambda 5007$ [OIII] flux may suffer from the large slit ($2.7'' \times 4.0''$) used by Dahari & De Robertis (1988). If the Balmer decrement was affected by off-nuclear emission, the reddening could easily be underestimated.

In a private communication to Malaguti et al. (1998), R. Maiolino reports $L^{\mathrm{int}}_{[\mathrm{OIII}]} \approx 6 \cdot 10^{44}$ erg s^{-1}. In the cosmology used by Malaguti et al., this corresponds to a $\lambda 5007$ [OIII] line flux of $1.5 \cdot 10^{-10}$ erg s^{-1} cm^{-2}. This, in turn, yields $L_{2-10\,\mathrm{keV}} \approx 1.5 \cdot 10^{46}$ erg s^{-1}, i.e. a source that is two orders of magnitude brighter than estimated by Malaguti et al.

For our analysis we will use the more conservative luminosity estimate of Malaguti et al. and Bassani et al. by using the average of their estimates and allowing for an uncertainty of 1 order of magnitude. An even higher luminosity, however, can clearly not be ruled out.

NGC 7679: The only available recent hard X-ray data of this object seem to be from Della Ceca et al. (2001) who use archival ASCA data and performed observations with *Beppo*SAX. Their analysis yields $N_{\mathrm{H}} = 2.2^{+1.8}_{-1.4} \cdot 10^{20}$ cm^{-2} and $F_{2-10\,\mathrm{keV}} = 5.6 \cdot 10^{-12}$ erg s^{-1} cm^{-2}, the latter corresponding to $L_{2-10\,\mathrm{kev}} = 3.3 \cdot 10^{42}$ erg s^{-1}.

4.1.3 Further notes on individual objects

In this subsection, I will present additional important information on some targets from our two VISIR samples. While for most objects AGN type, distance, etc. are unambiguous, this is not always the case. Therefore, peculiarities of individual objects have to be discussed here.

NGC 4303: The nucleus of this object is at the borderline between being a Seyfert 2.0 AGN and a low ionisation nuclear emission region (LINER) (Filippenko & Sargent, 1985). Since it is not evident – although very likely – that the nuclear X-ray source is an AGN, we adopt the classification as a LINER, in contrast to Véron-Cetty & Véron (2006).

Cen A: The redshift of Centaurus A is $z = 0.001825$. In our cosmology, this corresponds to a luminosity distance of 7.49 Mpc. However, the recessional movement of the galaxy is mostly peculiar and not due to the Hubble flow. The best available distance estimate toward Cen A is $d = 3.84$ Mpc. It was derived by Rejkuba (2004) using two independent methods: The period-luminosity relation for Mira variables and the luminosity of the tip of the red giant branch. The uncertainty in Cen A's distance together with – by now outdated – different cosmological parameters have led some authors to overestimate the luminosity of this object by more than one order of magnitude.

3C 445: This BLRG is an interesting case: Sambruna et al. (1998) and Shinozaki et al. (2006) both invoke two different absorbing components to fit their respective X-ray spectra. Moreover, the column densities derived from optical reddening and X-ray spectral analysis do not match. This indicates an anomalous gas:dust ratio (Maiolino et al., 2001). Recently, Grandi et al. (2007) observed 3C 445 with XMM-*Newton* and found a complex absorption pattern with 70 % of the nucleus observed through a layer of dense cold gas with $N_{\mathrm{H}} \simeq 4 \cdot 10^{23}$ cm^{-2} and the other 30 % observed through a less dense layer with $N_{\mathrm{H}} \simeq 8 \cdot 10^{22}$ cm^{-2}. Such partial covering of the nucleus may be an alternative to the anomalous gas:dust ratio in explaining the behaviour of the source. Another recent analysis of the same object was performed by Sambruna et al. (2007) who also invoke multiple layers of absorption as well as a reflection component to fit its X-ray spectrum.

NGC 7674: As discussed in subsection 4.1.2, NGC 7674 appears to be a Compton-thick AGN of high luminosity. Strictly speaking, it does not match our target selection criteria as its intrinsic hard X-ray luminosity cannot be inferred with any precision. It

Table 4.2: Characterisation of our galaxy sample for P77. Heliocentric redshifts z were taken from the NED, Seyfert types are according to Véron-Cetty & Véron (2006) and the inclination angles i of the host galaxies on the sky were taken from the Hyperleda database (Paturel et al., 2003). The absorption corrected hard X-ray luminosities and intrinsic column densities have been compiled from the literature (see section 4.1.2 for details). The last column contains the physical scales resolved by VISIR, computed for an angular resolution of $0.35''$, which is a typical value for our observations (see section 4.2).

Object	z	Sy	i	$\log L_{2-10\,\mathrm{keV}}$ [erg/s]	N_{H} [10^{21} cm^{-2}]	Scale [pc]
MCG-01-01-043	0.030	1.0	29.9°	42.50 ± 0.15	$0.327^{+0.274}_{-0.0}$	200
Mrk 590	0.026	1.0	25.9°	43.61 ± 0.25	n/a	175
NGC 1097	0.004	3.0	51.2°	40.80 ± 0.15	$1.3^{+0.4}_{-0.3}$	30
NGC 4303	0.005	3.0*	19.1°	39.16 ± 0.15	n/a	35
NGC 4472	0.003	2.0	50.1°	≤ 39.17	n/a	20
NGC 4507	0.012	1h	34.1°	43.30 ± 0.15	292 ± 23	80
NGC 4698	0.003	2.0	58.7°	39.08 ± 0.30	≤ 4.0	20
NGC 4941	0.004	2.0	53.5°	41.30 ± 0.30	450^{+250}_{-140}	30
IRAS 13197-1627	0.017	1h	55.0°	42.78 ± 0.20	390 ± 40	115
Cen A	0.002	2.0*	49.1°	41.68 ± 0.15	100 ± 30	7*
NGC 5135	0.014	2.0	44.8°	43.00 ± 0.50	> 1000	95
MCG-06-30-015	0.008	1.5	60.6°	42.57 ± 0.20	3.5 ± 1.1	55
NGC 5995	0.025	1.9	41.3°	43.54 ± 0.15	$9.0^{+0.5}_{-0.3}$	170
ESO 141-G55	0.036	1.0	40.0°	43.90 ± 0.15	n/a	240
Mrk 509	0.034	1.5	36.3°	44.10 ± 0.15	n/a	225
NGC 7172	0.009	2.0	57.8°	42.76 ± 0.40	83 ± 2	60
NGC 7213	0.006	3.0	28.6°	42.23 ± 0.15	n/a	40
3C 445	0.056	1.5	36.3°	44.19 ± 0.15	250 ± 136	365
NGC 7469	0.016	1.5	43.0°	43.15 ± 0.10	n/a	110
NGC 7674	0.029	1h	24.0°	44.56 ± 0.50	> 1000	195
NGC 7679	0.017	1.9	58.5°	42.52 ± 0.15	$0.22^{+0.18}_{-0.14}$	115

*Refer to subsection 4.1.3 for details.

is, however, an interesting test case in order to check whether the MIR – hard X-ray correlation holds for Compton-thick objects.

NGC 7679: As NGC 7679 is of Seyfert type 1.9 (broad Hα line but no broad Hβ), one would expect the X-ray spectrum to show a low-energy cutoff typical for absorbed systems. In their analysis, however, Della Ceca et al. (2001) found NGC 7679 to appear as a Seyfert 1 in X-rays. Moreover, they found evidence for a starburst in the nucleus of this object.

4.2 Observations and Data reduction

4.2.1 Observations

The data for this project were taken during ESO periods 75 (Spring 2004) and 77 (Spring 2005) in service mode at the Very Large Telescope (VLT). The instrument used was VISIR, the mid-infrared imager and spectrograph at the VLT (see section 3.2 for details on the instrument). Tables 4.3 and 4.4 show the observing log and resulting measurements for both observing programmes.

We used the standard imaging template of VISIR, with parallel chopping and nodding and a chop throw of $8''$. The parallel chop/nod mode was chosen for two reasons: First of all, having three instead of four beams on the detector facilitates avoiding bad pixels and the region affected by the electronic ghost. Secondly, by adding two beams (see fig. 3.1), we gain a factor $\sqrt{2}$ sensitivity in this double positive beam. For faint targets, this facilitates detection; for bright targets, the signal-to-noise ratio (S/N) achievable with perpendicular and parallel chopping and nodding is the same.

In order to get the best possible angular resolution, the small field camera ($0.075''$ / pixel) was used. Bright AGN were observed in three filters in order to allow a reconstruction of their spectral energy distribution (SED) in the MIR. Due to time constraints, faint objects could only be observed in one filter. All observations were executed in service mode with required observing conditions of clear sky and $0.8''$ seeing or less. The average seeing in the MIR (FWHM of standard stars) was $0.36''$ in P75 and $0.33''$ in P77; the average airmass was 1.15. No observation were executed at an airmass above 1.3. Science targets and photometric standards were all observed within 2 h of each other and with a maximum difference in airmass of 0.25. For most observations, however, differences in both time and airmass are much smaller than these values. For our P77 campaign, we selected guide stars by hand, using the guidecam tool provided by ESO, in order to avoid potential problems with telescope guiding.

Some of the observations had to be repeated due to unstable or unsuitable observational conditions. In these cases, only the data obtained under good conditions have been used for our scientific analysis as well as the characterisation of the average observing conditions. Observations that were later repeated are not listed in tables 4.3 and 4.4.

Table 4.3: Basic observational parameters for all used data from P75: Object name, observing date, used filter, the filter's central wavelengths, standard star name, flux, full width half maximum for standard star and science observations and airmass. As error estimates we use the standard deviation of all contributing beams (see section 4.2.2 details). The FWHM are the average of all beams of one exposure. All science and corresponding STD exposures were obtained with a maximum difference in airmass of 0.15.

Object	Obs. Date	Filter	λ_c [μm]	STD	Flux [mJ]	FWHM ["] STD	Obj	Airmass STD	Obj
Fairall 9	2005-07-21T09:24	SIV	10.49	HD5112	256.2 ± 5.4	0.32	0.35	1.118	1.219
Fairall 9	2005-07-21T09:29	NeIIref1	12.27	HD5112	329.8 ± 18.0	0.38	0.37	1.123	1.216
Fairall 9	2005-07-21T09:38	NeII	12.81	HD5112	305.7 ± 10.4	0.40	0.37	1.128	1.213
Fairall 9	2005-07-21T09:46	SIV	10.49	HD5112	234.9 ± 13.0	0.32	0.34	1.118	1.211
NGC 526a	2005-07-20T09:48	SIV	10.49	HD5112	198.6 ± 25.6	0.41	0.30	1.111	1.020
NGC 526a	2005-07-20T09:57	NeIIref1	12.27	HD5112	275.3 ± 55.0	0.41	0.35	1.115	1.018
NGC 526a	2005-07-20T10:10	SIV	10.49	HD5112	198.6 ± 22.0	0.41	0.32	1.111	1.017
NGC 3783	2005-04-17T01:27	SIV	10.49	HD90957	568.1 ± 46.2	0.29	0.31	1.010	1.064
NGC 3783	2005-04-17T01:32	PAH2ref2	11.88	HD90957	632.2 ± 21.9	0.34	0.35	1.011	1.059
NGC 3783	2005-04-17T01:36	NeIIref1	12.27	HD90957	721.8 ± 67.3	0.34	0.36	1.013	1.055
NGC 4579	2005-04-30T03:07	SIV	10.49	HD108985	67.32 ± 17.30	0.30	0.25	1.240	1.248
NGC 4579	2005-04-30T03:12	PAH2ref2	11.88	HD108985	68.48 ± 13.84	0.33	0.29	1.247	1.255
NGC 4579	2005-04-30T03:24	NeIIref1	12.27	HD108985	60.69 ± 20.60	0.34	0.30	1.254	1.268
NGC 4579	2005-04-30T03:37	SIV	10.49	HD108985	64.24 ± 11.55	0.30	0.32	1.240	1.279
NGC 4593	2005-04-30T04:05	SIV	10.49	HD108985	331.4 ± 28.8	0.30	0.31	1.240	1.126
NGC 4593	2005-04-30T04:14	PAH2ref2	11.88	HD108985	335.4 ± 26.1	0.33	0.33	1.247	1.142
NGC 4593	2005-04-30T04:23	NeIIref1	12.27	HD108985	382.4 ± 73.3	0.34	0.36	1.254	1.160
PKS 2048-57	2005-06-10T08:06	PAH2ref2	11.88	HD169916	883.1 ± 53.0	0.38	0.40	1.101	1.185
PKS 2048-57	2005-06-10T08:10	NeIIref1	12.27	HD169916	1040 ± 63.7	0.41	0.43	1.108	1.185
PKS 2048-57	2005-06-10T08:15	SIV	10.49	HD169916	654.9 ± 27.5	0.37	0.39	1.088	1.184
PG 2130+099	2005-06-10T08:27	PAH2	11.25	HD169916	151.9 ± 7.9	0.39	0.38	1.095	1.227
PG 2130+099	2005-06-10T08:36	SIVref1	9.82	HD169916	114.6 ± 19.9	0.35	0.36	1.082	1.221
PG 2130+099	2005-06-10T08:52	NeII	12.81	HD169916	179.1 ± 30.5	0.41	0.43	1.011	1.218
PG 2130+099	2005-06-10T09:09	PAH2	11.25	HD169916	173.9 ± 16.5	0.39	0.40	1.095	1.220
NGC 7314	2005-07-20T06:02	SIV	10.49	HD178345	74.88 ± 29.4	0.40	0.36	1.121	1.051

Continued on Next Page...

Table 4.3 – Continued

Object	Obs. Date	Filter	λ_c [μm]	STD	Flux [mJ]	FWHM [''] STD	FWHM [''] Obj	Airmass STD	Airmass Obj
NGC 7314	2005-07-20T06:11	PAH2	11.25	HD178345	74.54 ± 22.0	0.36	0.37	1.128	1.036
NGC 7314	2005-07-20T06:27	SIV	10.49	HD178345	86.55 ± 36.5	0.40	0.34	1.121	1.024

Table 4.4: Basic observational parameters for all used data from P77: Object name, observing date, used filter, the filter's central wavelengths, standard star name, flux, full width half maximum for standard star and science observations and airmass. As error estimates we use the standard deviation of all contributing beams (see section 4.2.2 for details). The FWHM are the average of all beams of one exposure. All science and corresponding STD exposures were obtained with a maximum difference in airmass of 0.25.

Object	Obs. Date	Filter	λ_c [μm]	STD	Flux [mJ]	FWHM ["] STD	FWHM ["] Obj	Airmass STD	Airmass Obj
MCG-01-01-043	2006-07-13T09:30	NeII	12.81	HD787	≤ 68.	0.37	–	1.014	1.064
Mrk 590	2006-08-17T09:12	SIV	10.49	HD12524	75.9 ± 20.9	0.29	0.24	1.071	1.094
Mrk 590	2006-08-17T09:16	PAH2	11.25	HD12524	75.0 ± 2.1	0.30	0.27	1.073	1.094
Mrk 590	2006-08-17T09:21	NeII	12.81	HD12524	106.3 ± 13.3	0.33	0.32	1.075	1.094
NGC 1097	2006-08-07T09:08	NeIIref1	12.27	HD787	28.2 ± 6.8	0.32	0.37	1.037	1.051
NGC 4303	2006-04-15T04:07	NeIIref1	12.27	HD107328	≤ 22.	0.40	–	1.155	1.147
NGC 4472	2006-04-18T02:22	NeIIref1	12.27	HD98118	≤ 77.	0.34	–	1.171	1.238
NGC 4507	2006-04-15T02:58	SIV	10.49	HD110458	523.2 ± 24.9	0.32	0.32	1.151	1.052
NGC 4507	2006-04-15T03:02	PAH2	11.25	HD110458	589.5 ± 21.8	0.33	0.32	1.147	1.049
NGC 4507	2006-04-15T03:07	NeIIref1	12.27	HD110458	685.0 ± 50.1	0.34	0.34	1.143	1.047
NGC 4698	2006-04-18T03:29	NeIIref1	12.27	HD98118	≤ 42.	0.34	–	1.171	1.196
NGC 4941	2006-04-19T05:22	NeIIref1	12.27	HD133774	81.3 ± 6.0	0.34	0.35	1.045	1.131
IRAS 13197-1627	2006-04-09T05:26	SIV	10.49	HD133774	527.1 ± 17.1	0.29	0.36	1.012	1.018
IRAS 13197-1627	2006-04-09T05:31	PAH2	11.25	HD133774	674.3 ± 35.8	0.32	0.38	1.012	1.021
IRAS 13197-1627	2006-04-09T05:35	NeIIref1	12.27	HD133774	875.0 ± 45.8	0.34	0.43	1.013	1.023
Centaurus A	2006-04-09T05:07	SIV	10.49	HD133774	642.6 ± 26.6	0.29	0.32	1.012	1.054
Centaurus A	2006-04-09T05:11	PAH2	11.25	HD133774	946.6 ± 29.2	0.32	0.36	1.012	1.055
Centaurus A	2006-04-09T05:16	NeIIref1	12.27	HD133774	1451 ± 73.1	0.34	0.35	1.013	1.056
NGC 5135	2006-04-09T05:45	NeIIref1	12.27	HD133774	122.5 ± 12.2	0.34	0.35	1.013	1.021
MCG-06-30-015	2006-04-14T03:58	SIV	10.49	HD123123	339.2 ± 43.7	0.30	0.32	1.110	1.034
MCG-06-30-015	2006-04-14T04:03	PAH2	11.25	HD123123	392.5 ± 54.1	0.31	0.33	1.103	1.030
MCG-06-30-015	2006-04-14T04:07	NeIIref1	12.27	HD123123	392.7 ± 49.3	0.32	0.35	1.096	1.027
NGC 5995	2006-04-14T04:48	SIV	10.49	HD123123	296.8 ± 30.2	0.30	0.37	1.110	1.195
NGC 5995	2006-04-14T04:52	PAH2	11.25	HD133774	332.9 ± 47.2	0.33	0.37	1.022	1.181
NGC 5995	2006-04-14T04:57	NeII	12.81	HD123123	421.1 ± 60.6	0.37	0.40	1.090	1.169

Continued on Next Page...

Table 4.4 – Continued

Object	Obs. Date	Filter	λ_c [μm]	STD	Flux [mJ]	FWHM ["] STD	FWHM ["] Obj	Airmass STD	Airmass Obj
ESO 141-G55	2006-05-05T09:14	SIV	10.49	HD178345	160.0 ± 21.2	0.37	0.37	1.043	1.206
ESO 141-G55	2006-05-05T09:18	PAH2	11.25	HD178345	169.8 ± 23.9	0.37	0.36	1.045	1.206
ESO 141-G55	2006-05-05T09:23	NeIIref1	12.27	HD178345	169.7 ± 47.1	0.37	0.32	1.046	1.207
Mrk 509	2006-06-14T10:20	SIV	10.49	HD178345	226.5 ± 7.7	0.47	0.32	1.260	1.253
Mrk 509	2006-06-14T10:25	PAH2	11.25	HD178345	235.0 ± 21.4	0.39	0.33	1.282	1.270
Mrk 509	2006-06-14T10:30	NeII	12.81	HD178345	269.0 ± 41.7	0.40	0.38	1.318	1.288
PKS 2048-57	2006-05-05T09:54	SIV	10.49	HD178345	590.6 ± 19.4	0.37	0.38	1.043	1.199
PKS 2048-57	2006-05-05T09:59	PAH2	11.25	HD178345	752.4 ± 45.5	0.37	0.38	1.045	1.196
PKS 2048-57	2006-05-05T10:03	NeIIref1	12.27	HD178345	1035 ± 107.9	0.37	0.43	1.046	1.193
NGC 7172	2006-07-09T10:00	NeIIref1	12.27	HD217902	164.9 ± 27.1	0.37	0.35	1.187	1.188
NGC 7213	2006-07-14T09:58	SIV	10.49	HD787	283.8 ± 6.2	0.35	0.31	1.031	1.272
NGC 7213	2006-07-14T10:03	PAH2	11.25	HD787	264.0 ± 38.5	0.34	0.35	1.034	1.284
NGC 7213	2006-07-14T10:07	NeIIref	12.27	HD787	271.0 ± 26.5	0.32	0.32	1.040	1.298
3C 445	2006-07-10T08:59	SIV	10.49	HD217902	168.4 ± 6.7	0.29	0.31	1.147	1.129
3C 445	2006-07-10T09:04	PAH2	11.25	HD217902	184.6 ± 10.4	0.30	0.32	1.147	1.135
3C 445	2006-07-10T09:08	NeII	12.81	HD217902	205.8 ± 27.8	0.33	0.37	1.148	1.143
NGC 7469	2006-07-12T07:21	SIV	10.49	HD189695	460.0 ± 20.0	0.31	0.38	1.324	1.250
NGC 7469	2006-07-12T07:25	PAH2	11.25	HD189695	487.3 ± 38.6	0.33	0.41	1.334	1.243
NGC 7469	2006-07-12T07:30	NeIIref1	12.27	HD189695	626.9 ± 34.7	0.34	0.37	1.344	1.237
NGC 7674	2006-07-13T08:55	NeII	12.81	HD217902	506.3 ± 29.4	0.38	0.44	1.150	1.199
NGC 7679	2006-07-10T09:21	SIV	10.49	HD217902	42.4 ± 13.0	0.28	0.24	1.147	1.140
NGC 7679	2006-07-10T09:26	PAH2	11.25	HD217902	43.3 ± 6.6	0.30	0.18	1.147	1.143
NGC 7679	2006-07-10T09:30	NeIIref1	12.27	HD217902	45.6 ± 18.3	0.32	0.41	1.147	1.146

4.2.2 Data reduction and calibration

When reducing MIR data, first of all, the appropriate subtractions and additions of all chopping-halfcycles and nodding half-cycles have to be performed. At the same time, bad pixels and cosmic rays have to be removed. The latter are identified by comparing consecutive exposures to each other. In case of VISIR, the detector produces a stripe pattern. Its origin is unknown but the VISIR consortium pipeline (written and kindly provided to us by Eric Pantin) is able to remove it very reliably.

VISIR imaging data is usually not flat-fielded before co-adding the single exposures, as this hardly improves the image quality. For spectroscopic data, some tests imply that flat-fielding actually may have a significant effect on the data quality.

After co-adding all single exposures of one observation, the counts on the detector are converted to ADUs per second. Thus, we can perform photometric measurements of all the images of our scientific target. Despite chopping and nodding, however, a residual background remains on the image. This we removed by fitting a two-dimensional polynomial to all detector areas not "contaminated" by the scientific target.

Unfortunately, this residual background sometimes varies faster than the nodding position is changed. This leads to background variations between consecutive nodding cycles. In order to avert these from compromising our photometry, for sources observed in somewhat unstable conditions, we reduced each nodding cycle separately. This, of course, is only possible, if the target is bright enough to be visible after the exposure time of just one nodding cycle.

Our science targets were all observed with parallel chopping and nodding. With a chop throw of $8''$, this gives us three images of the object, the central one having twice

Table 4.5: VISIR conversion factors for the filters we used. We have analysed the standard stars that were used to calibrate our data and state mean value of the conversion factor and absolute and relative standard deviation.

Filter name	mean conversion [Jy / (ADU/s)]	standard deviation absolute	relative
P 75			
SIVref1	$1.174 \cdot 10^{-5}$	n/a	
SIV	$1.046 \cdot 10^{-5}$	$0.32 \cdot 10^{-6}$	0.031
PAH2	$0.310 \cdot 10^{-5}$	n/a	
PAH2ref2	$0.525 \cdot 10^{-6}$	$2.34 \cdot 10^{-6}$	0.445
NeIIref1	$0.940 \cdot 10^{-6}$	$4.02 \cdot 10^{-6}$	0.427
NeII	$1.216 \cdot 10^{-5}$	$0.64 \cdot 10^{-6}$	0.053
P 77			
SIV	$1.022 \cdot 10^{-5}$	$0.60 \cdot 10^{-6}$	0.055
PAH2	$0.298 \cdot 10^{-5}$	$0.18 \cdot 10^{-6}$	0.062
NeIIref1	$1.091 \cdot 10^{-5}$	$0.58 \cdot 10^{-6}$	0.053
NeII	$1.171 \cdot 10^{-5}$	$1.10 \cdot 10^{-6}$	0.094

the flux of the other ones (see section 3.1 for details on the chop/nod procedure). We can use this to estimate the measurement error: Since noise caused by background variations is much larger than the photon noise, the standard deviation of the three images is a very good error measure. For those objects, for which we reduced each nodding cycle separately we measured the deviation among the images from each nodding cycle instead of using the combined images.

In some cases, unfortunately, we had to drop some of the images. In P75, the reason for this was the close proximity of some images to the edge of the detector and the loss of flux caused by this. In P77, we avoided this problem by rotating the chop/nod – direction by 45°. In several cases, however, this led to one image being centered exactly on a bad pixel and thus useless.

For the flux measurements, we used relatively small apertures with radii of ~ 10 pixels $(= 0.75'')$. This was done to avoid contamination by a residual background. We then corrected the measured fluxes using the radial profiles of bright photometric standard stars.

Four of our targets – MCG-01-01-043, NGC 4303, NGC 4472 and NGC 4698 – were not detected by VISIR. Upper limits for the fluxes of these objects were obtained by measuring the maximum noise-induced signal in those parts of the detector in which we expect the target to be. We consider each pixel within a radius of $1''$ of the centre of the detector for the position of the double positive image. The positions of the two negative images are inferred using the known chop throw and chopping angle. We then determine the maximum co-added signal of all three images, regardless of the sign of each image. After multiplying the result by 3, we obtain a conservative $3\,\sigma$ upper limit on the flux of these sources.

When the photometric data of each image of the object is extracted, we calibrate the flux using photometric standard stars. Here, we found the ADUs-per-second-to-Jansky conversion factor to be very stable. Exceptions are the PAH2ref2 filter and – only during P75 – the NeIIref1 filter. The statistical analysis of the conversion factors that were used for flux calibration is provided in table 4.2.2. Note that the large deviation for the NeIIref1 filter during P75 was caused by one outlier; the conversion factors for all remaining observations agree very well with each other. The important result of this statistical analysis is that our high precision photometry is reliable.

5 Results[1]

> *Everyone knew that stars were points of light. If they weren't, some would be visibly bigger than others. Some were fainter than others, of course, but that was probably due to clouds. In any case, their purpose, according to established Discworld law, was to lend a little style to the night.*

> Terry Pratchett, Ian Stewart & Jack Cohen: The Science of
> Discworld (1999)

In this chapter, I will present the results of our two observing campaigns. First of all, the mid-IR properties as seen with VISIR are put forward. Afterwards, I compare these to *Spitzer* data of the same sources. Finally, the statistical analysis of the mid-IR – hard X-ray correlation is presented. Here, we have to consider two possible error sources: Contamination of IR fluxes and a redshift bias in our data.

5.1 The mid IR properties of individual objects

Out of the 29 AGN observed with VISIR, 25 were detected. The recorded images of objects observed in at least 2 filters are shown in figs. 5.1 to 5.20, sorted by Right Ascension. Objects only observed in one filter are shown in fig. 5.21, except for NGC 1097 which is shown in fig. 5.22. The images are linearly scaled. The minimum (black colour) is set to the mean background value $\langle BG \rangle$. The maximum (white colour) is set to $\langle BG \rangle + 5\,\sigma_{BG}$ where σ_{BG} is the standard deviation of the background.

For the 4 non-detected objects, $3\,\sigma$ upper limits were derived by measuring the flux of the largest noise-induced signal (see section 4.2.2 for details). In Tables 4.3 and 4.4, the flux or flux limit and size of the PSF is listed for each object.

Most objects appear point-like and the torus remains unresolved in all cases. In some cases the observing conditions were good enough to provide us with diffraction limited imaging. In the images of NGC 3783 (5.4), NGC 4507 (5.5) and NGC 4593 (5.7), we clearly see the first Airy ring. It is also barely visible in a number of other images. Slight extension of the central source is visible in IRAS 13197-1627 (fig. 5.8) and NGC 5995 (fig. 5.11). Extranuclear emission is observed in NGC 1097 (fig. 5.22), NGC 5135 (fig. 5.21) and NGC 7469 (fig. 5.19). These objects will be discussed in more detail in subsection 5.1.1.

---

[1] Some of the results presented in this chapter have been published in Horst, Smette, Gandhi, & Duschl (2006) and Horst, Gandhi, Smette, & Duschl (2007).
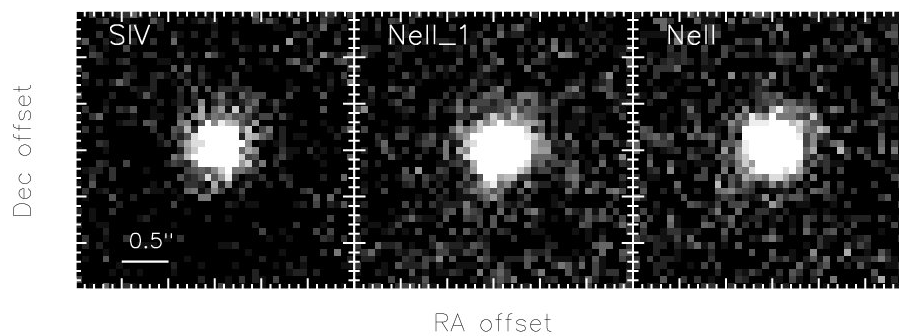
Figure 5.1: VISIR images of Fairall 9, showing the central $3.0'' \times 3.0''$ in three different filters (SIV, NeIIref1, NeII). North is up and East is left. The object is unresolved.
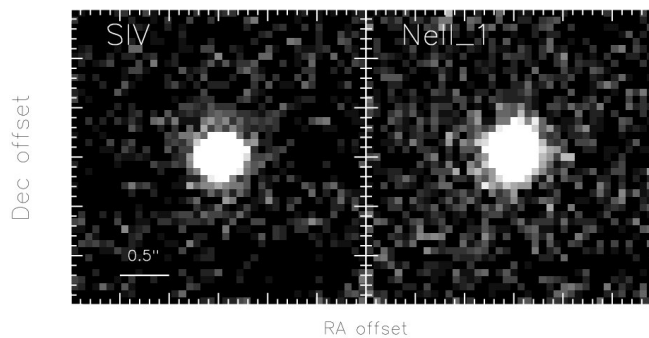
Figure 5.2: VISIR images of NGC 526a, showing the central $3.0'' \times 3.0''$ in two different filters (SIV, NeIIref1). North is up and East is left. The object is unresolved.
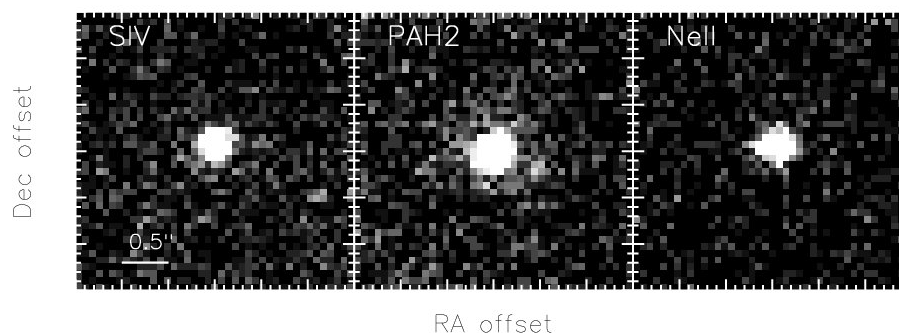
Figure 5.3: VISIR images of Mrk 590, showing the central $3.0'' \times 3.0''$ in three different filters (SIV, PAH2, NeII). North is up and East is left. The object is unresolved.
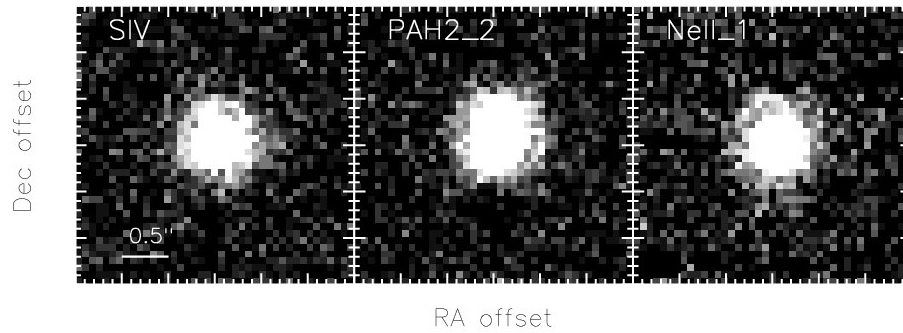
Figure 5.4: VISIR images of NGC 3783, showing the central $3.0'' \times 3.0''$ in three different filters (SIV, PAH2ref2, NeIIref1). North is up and East is left. The object is unresolved and we even see the first Airy ring in the SIV and NeIIref1 filters.
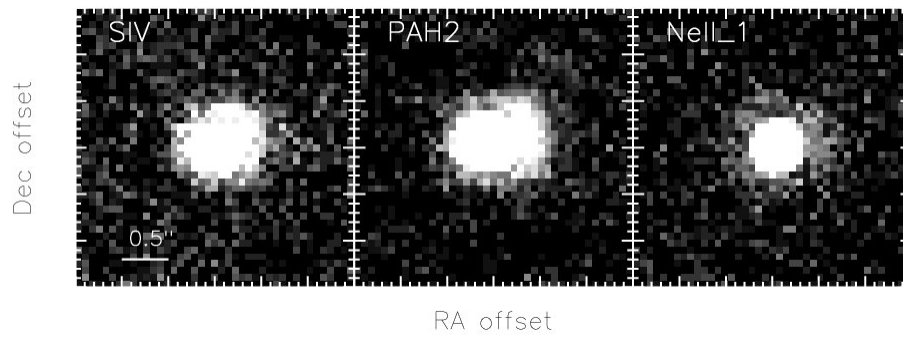
Figure 5.5: VISIR images of NGC 4507, showing the central $3.0'' \times 3.0''$ in three different filters (SIV, PAH2, NeIIref1). North is up and East is left. The object in unresolved. The small dent to the Northwest is the brightest part of the Airy ring.
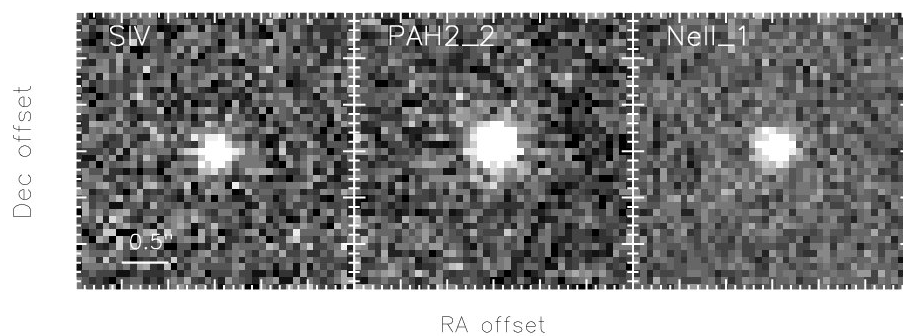
Figure 5.6: VISIR images of NGC 4579, showing the central $3.0'' \times 3.0''$ in three different filters (SIV, PAH2ref2, NeIIref1). North is up and East is left. The object is unresolved.
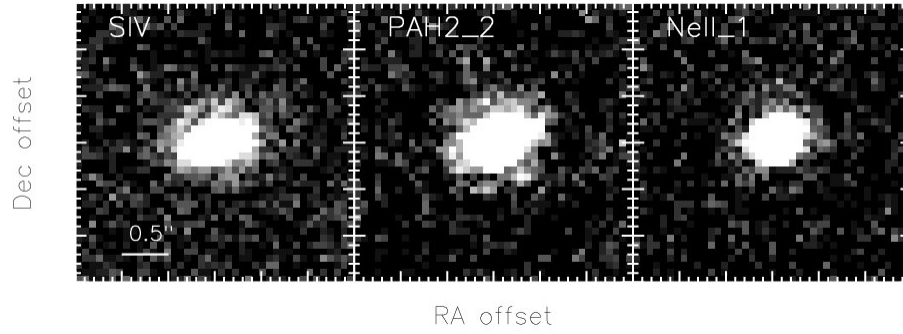
Figure 5.7: VISIR images of NGC 4593, showing the central $3.0'' \times 3.0''$ in three different filters (SIV, PAH2ref2, NeIIref1). North is up and East is left. The object is unresolved and we see the first Airy ring in all three images.
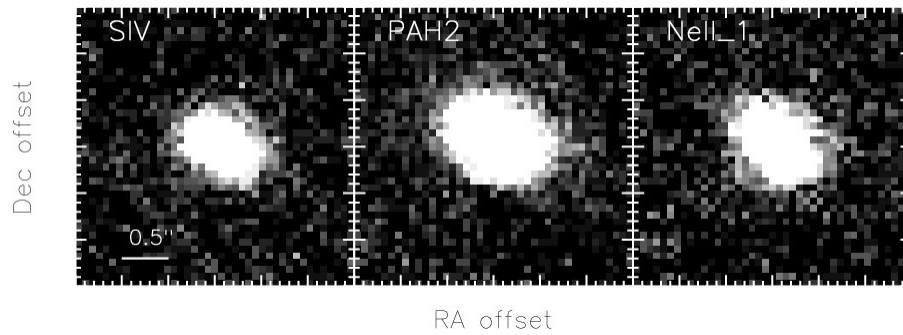
Figure 5.8: VISIR images of IRAS 13197-1627, showing the central $3.0'' \times 3.0''$ in three different filters (SIV, PAH2, NeIIref1). North is up and East is left. The object shows a slight elongation perpendicular to the chop/nod direction, with a PSF that is slightly larger than that of the according standard star (see table 4.4).
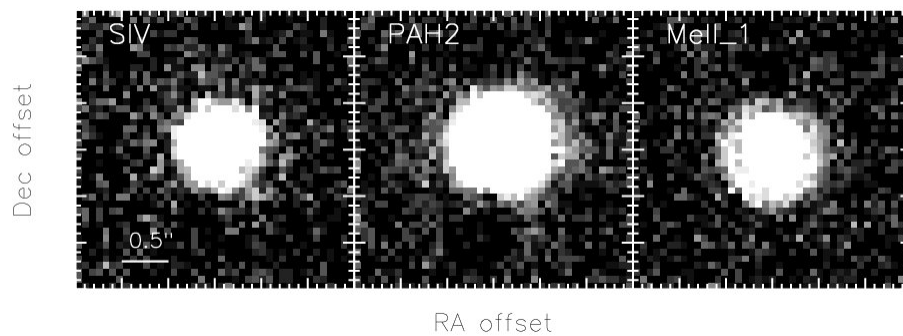
Figure 5.9: VISIR images of Cen A, showing the central $3.0'' \times 3.0''$ in three different filters (SIV, PAH2, NeIIref1). North is up and East is left. The object is unresolved.
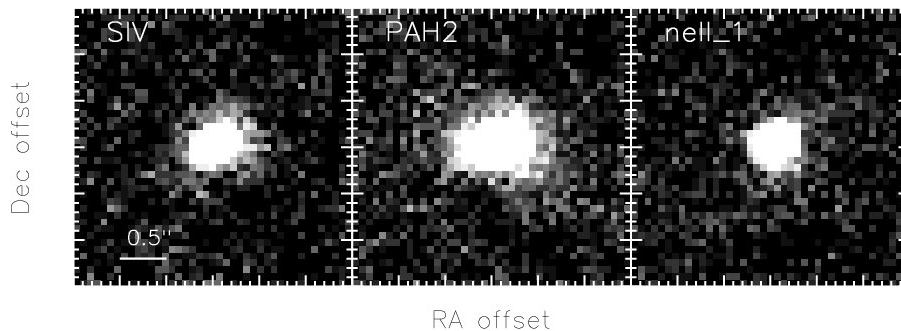
Figure 5.10: VISIR images of MCG-06-30-015, showing the central $3.0'' \times 3.0''$ in three different filters (SIV, PAH2, NeIIref1). North is up and East is left. The object is unresolved.
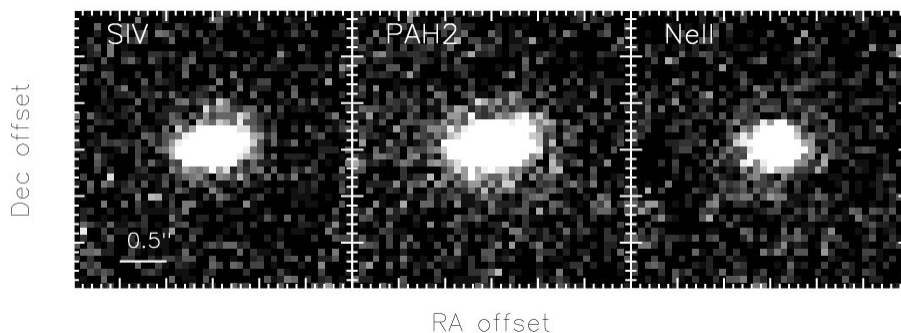
Figure 5.11: VISIR images of NGC 5995, showing the central $3.0'' \times 3.0''$ in three different filters (SIV, PAH2, NeII); North is up and East is left. Morphology in the PAH2 filter and the the size of the PSF (see table 4.4) hint toward a slight extension of the object.
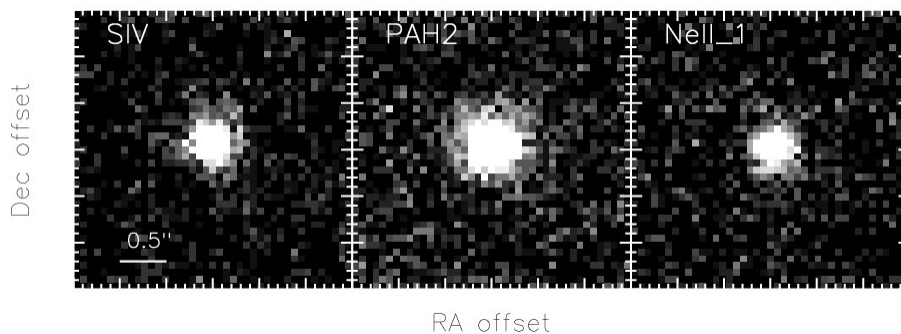
Figure 5.12: VISIR images of ESO 141-G55, showing the central $3.0'' \times 3.0''$ in three different filters (SIV, PAH2, NeIIref1). North is up and East is left. The object is unresolved.
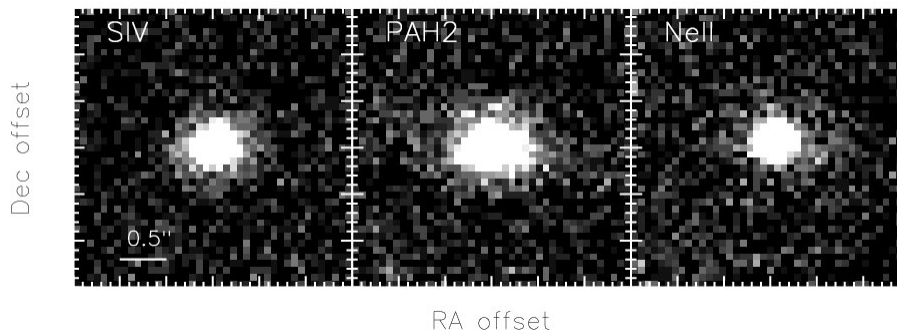
Figure 5.13: VISIR images of Mrk 509, showing the central $3.0'' \times 3.0''$ in three different filters (SIV, PAH2, NeII). North is up and East is left. The object is unresolved.
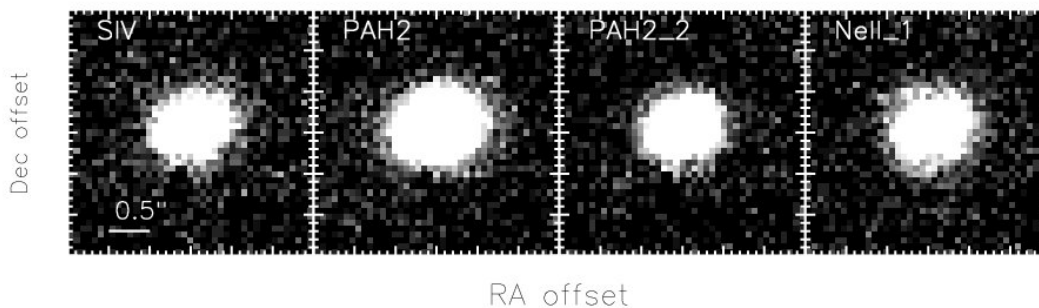
Figure 5.14: VISIR images of PKS 2048-57, showing the central $3.0'' \times 3.0''$ in four different filters (SIV, PAH2, PAH2ref2, NeIIref1). North is up and East is left. The object is unresolved.
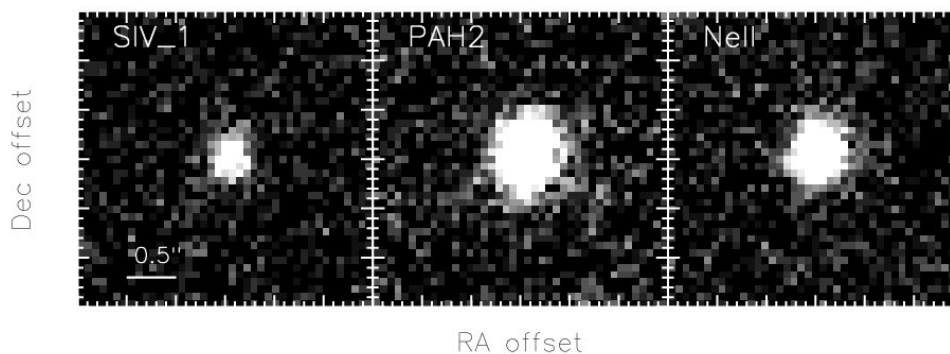
Figure 5.15: VISIR images of PG 2130+099, showing the central $3.0'' \times 3.0''$ in three different filters (SIVref1, PAH2, NeII). North is up and East is left. The object is unresolved.
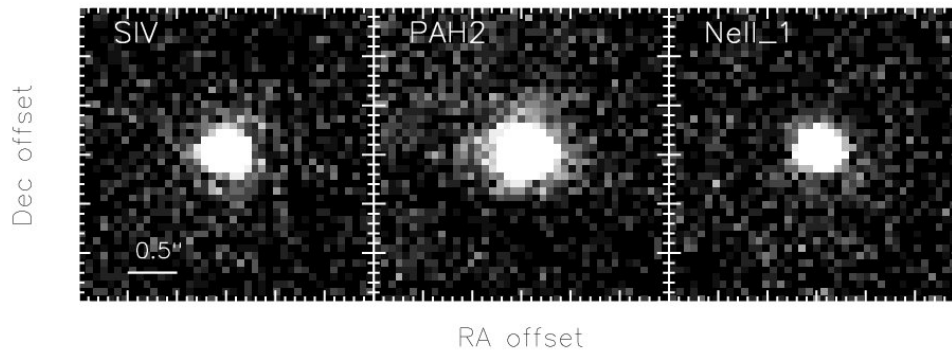
Figure 5.16: VISIR images of NGC 7213, showing the central $3.0'' \times 3.0''$ in three different filters (SIV, PAH2, NeIIref1). North is up and East is left. The object is unresolved.
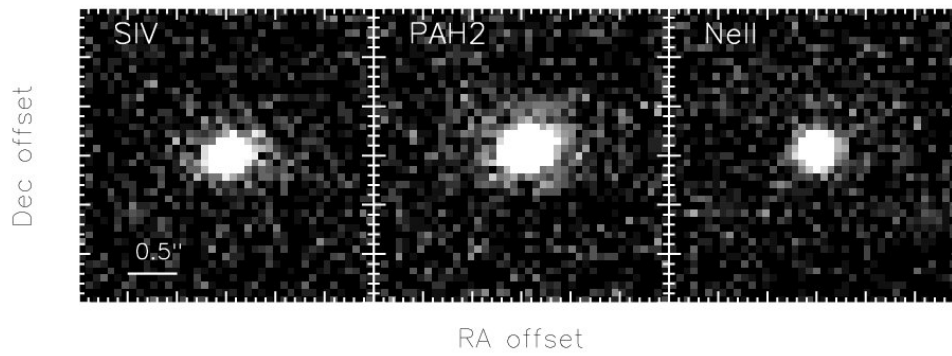
Figure 5.17: VISIR images of 3C 445, showing the central $3.0'' \times 3.0''$ in three different filters (SIV, PAH2, NeII). North is up and East is left. The object is unresolved
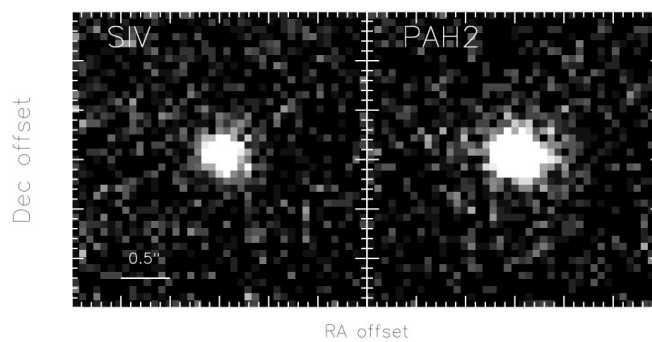
Figure 5.18: VISIR images of NGC 7314, showing the central $3.0'' \times 3.0''$ in two different filters (SIV, PAH2). North is up and East is left. The object is unresolved.
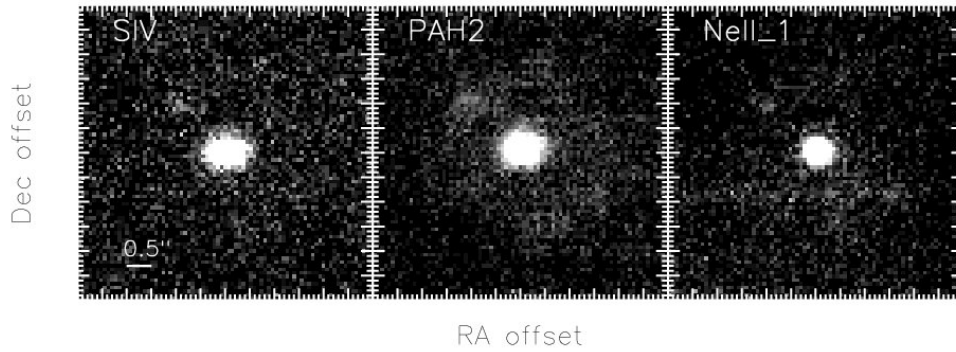
Figure 5.19: VISIR images of NGC 7469. showing the central $6.0'' \times 6.0''$ in three different filters (SIV, PAH2, NeIIref1). North is up and East is left. A diffuse emission component is visible around the nuclear point source; in the PAH2 filter (central panel), a ring of emission knots is discernible.
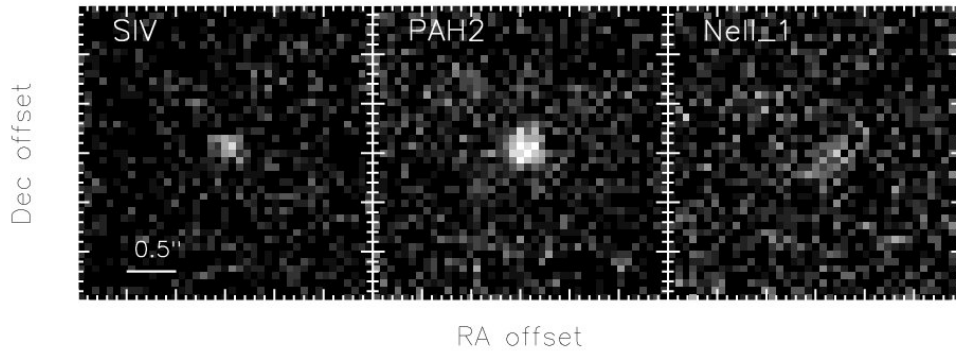
Figure 5.20: VISIR images of NGC 7679, showing the central $3.0'' \times 3.0''$ in three different filters (SIV, PAH2, NeIIref1). North is up and East is left. The object is unresolved.

In figs. 5.23 to 5.25, I have plotted the MIR SEDs of those objects which were observed in two or more different filters. These SEDs are usually inclining longward of 11 μm, but show a large variety of shapes.

Among the type I (Sy types 1.0, 1.2 and 1.5) sources (fig. 5.23), we find several objects (i.e. Mrk 590, NGC 3783, NGC 4593, NGC 7469) with a flat SED between 10 μm and 11 μm and a steep incline toward longer wavelengths. Two objects – Fairall9 and MCG-06-30-015 – exhibit a peak between 10.5 μm and 12 μm, indicative of a shifted 9.7 μm silicate emission feature. A shift of the silicate emission feature toward longer wavelengths with respect to the more commonly observed absorption feature is observed for virtually all objects for which the feature has been detected with *Spitzer* (see Hao et al., 2005; Siebenmorgen et al., 2005; Sturm et al., 2005, or fig. 2.4). Finally, the SEDs of ESO 141-G55, Mrk 509 and PG 2130+099 are remarkably flat. A weak silicate
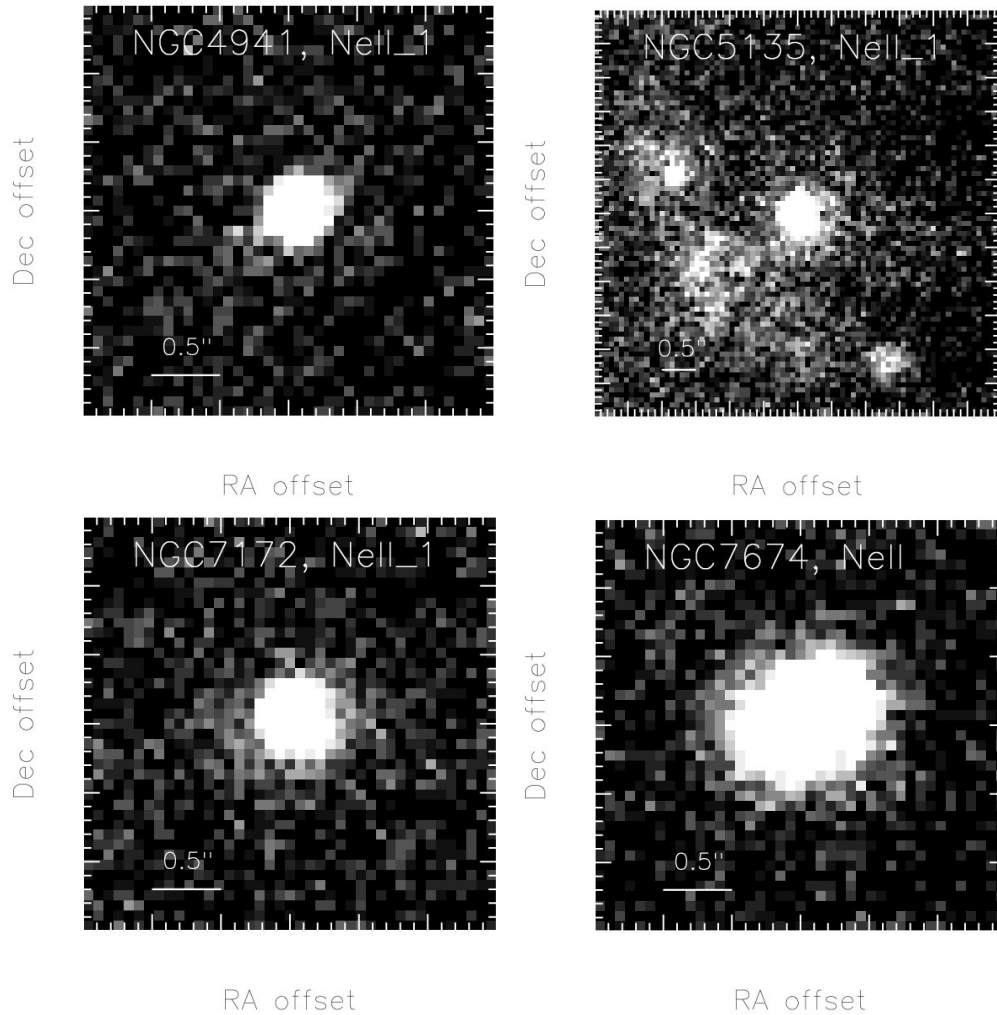
Figure 5.21: VISIR images of all sources that were only observed in one filter, excluding NGC 1097 (see fig. 5.22): NGC 4941, NGC 5135, NGC 7172, NGC 7674. In all images North is up and East is left. Except for NGC 5135, all objects are unresolved. NGC 5135, as well, has a point-like central source, but exhibits several additional sources, arranged in an arc to the Southeast of the nucleus. Please also note that the spatial scaling is different for NGC 5135 than for the other objects.

Figure 5.22: VISIR image of NGC 1097 taken in the NeIIref1 filter, showing the central $16.5'' \times 16.5''$. North is up and East is left. In the Northwestern and Southeastern corner, extra-nuclear emission is visible; these sources belong to the famous starburst ring of NGC 1097.
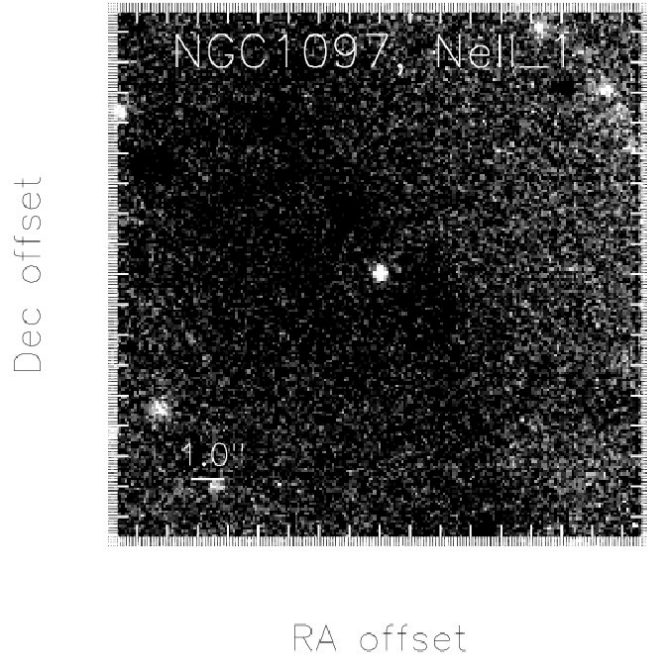
emission feature may be hidden in these SEDs, especially in the case of PG 2130+099 where the energy output inclines between $9.0\,\mu$m and $10.5\,\mu$m.

The type II (Sy types 1.8, 1.9, 2.0 and 1h) objects can also be separated into different groups. First of all, three objects, namely IRAS 13197-1627, Cen A and PKS 2048-57 show a steep rise toward longer wavelengths. This could either be due to a steep rise in the dust continuum emission or because of a deep $9.7\,\mu$m silicate absorption feature. NGC 526a shows the same trend but much less steep. NGC 4507 and NGC 5995 also exhibit SEDs that are indicative of the silicate absorption feature. In both objects, the continuum slope appears to be flat and the silicate feature is rather weak, its red wing not extending beyond $11\,\mu$m. Two objects have SEDs with unexpected shapes: The one of NGC 7679 is completely flat, and the one of NGC 7314 is even declining from $10.5\,\mu$m to $11.2\,\mu$m. NGC 7314 is on of the two objects which do not meet the constraint on host galaxy inclination that we later imposed on our second AGN sample. With an inclination of $70.3°$ the host galaxy might block the line of sight toward the nucleus. Absorption by cold dust would explain the observed spectral shape very well. On the other hand, in NGC 7314 broad lines were detected in the polarised light. This makes obscuration by the host galaxy unlikely. An alternative explanation would be the presence of a weak silicate emission feature. While this would be surprising for a type II AGN, it would support recent models of clumpy tori (see section 2.3.1).

There are two LINER type AGN for which we can compile MIR SEDs from our VISIR data: NGC 4579 and NGC 7213. Both have a declining energy output toward longer wavelengths, with NGC 7213 showing a steeper decline than NGC 4579. Among our sample, only two other objects show similar SEDs: The Sy 1 object ESO 141-G55 and the Sy 1h AGN NGC 7314.
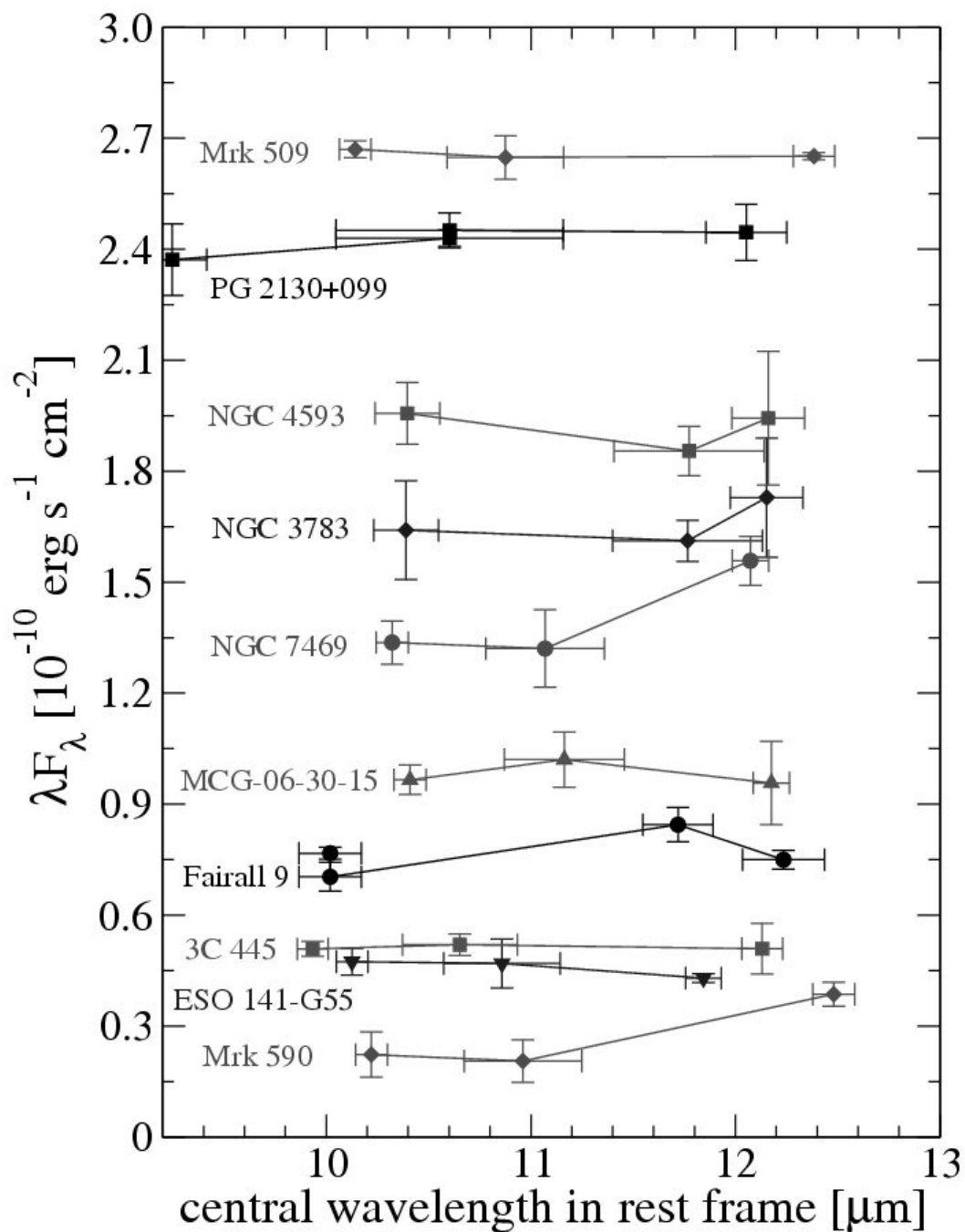
Figure 5.23: VISIR SEDs of the 10 type I AGN with photometric data in 2 or more filters. Three objects have been offset for clarity: NGC 4593 by $1.0 \cdot 10^{-10}$ erg s^{-1} cm^{-2} and Mrk 509 and PG 2130+099 by $2.0 \cdot 10^{-10}$ erg s^{-1} cm^{-2}.
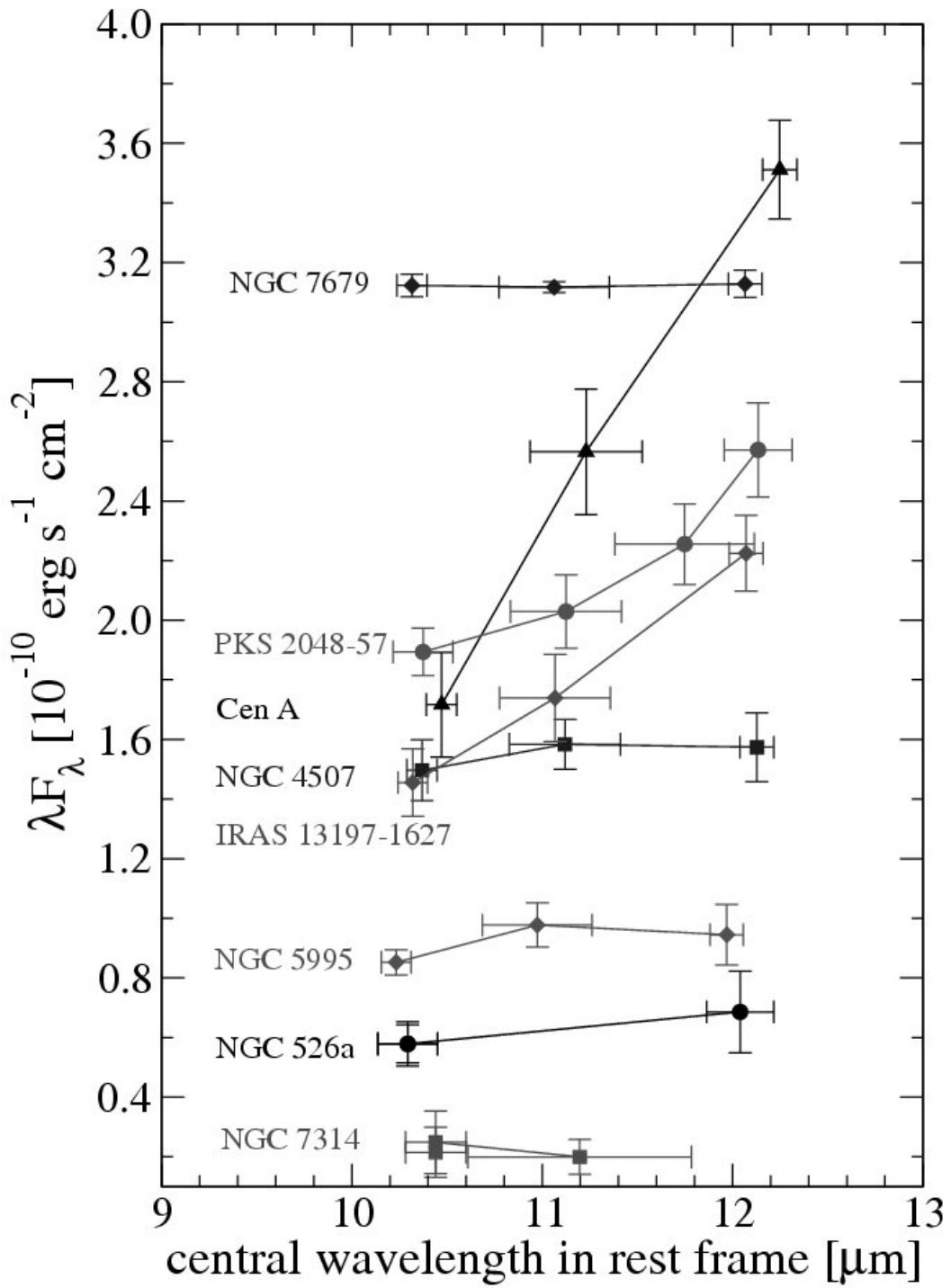
Figure 5.24: VISIR SEDs of the 8 type II AGN with photometric data in 2 or more filters. For clarity, NGC 7679 was offset by $3.0 \cdot 10^{-10}$ erg s^{-1} cm^{-2}.
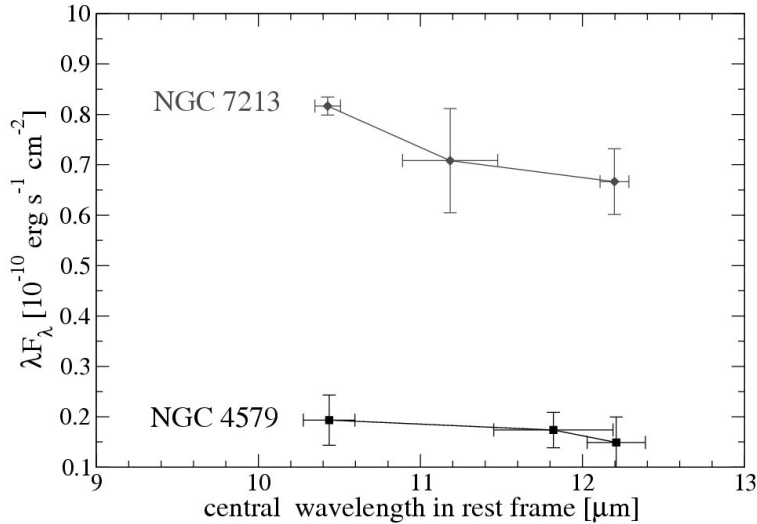
Figure 5.25: VISIR SEDs of the 2 LINER AGN with photometric data in 2 or more filters.

5.1.1 Morphology of extra-nuclear emission

Three of the sources in our sample show extended extra-nuclear emission: NGC 1097, NGC 5135 and NGC 7469. In all three cases, we see distinct knots of star formation (SF) around the nucleus. Typical distances between SF knots and the AGN are $8.2''$ (~ 700 pc) in NGC 1097, $1.5''$ (~ 400 pc) in NGC 5135 and $1.3''$ (~ 400 pc) in NGC 7469. In the latter two objects the proximity of the SF components to the AGN as well as the presence of a weak diffuse component does not allow us to rule out a significant contribution of SF to the measured flux of the central point source. We have estimated this contribution by assuming that the flux of the SF component on top of the AGN does not exceed the flux of the brightest distinct SF knot. In the NeIIref1 filter, this yields a maximum contamination of 15 % for NGC 5135 and 10 % for NGC 7469, respectively. These uncertainties have been added to the photometric error and are accounted for in our subsequent statistical analysis.

The SF we observe in **NGC 1097** (fig. 5.22) is part of the well-known starburst ring of this galaxy. Unfortunately, the field of view VISIR has in the high resolution mode does not allow for imaging of the whole ring. Moreover, as the chop throw is of the same order of magnitude as the separation between the AGN and the SF regions, positive and negative images of different structures become intermingled. Therefore, we are not able to study the MIR properties of the starburst in NGC 1097.

In **NGC 5135**, we see an arc of star formation at a distance of ~ 400 pc from the AGN. In fig. 5.26, I show an overlay of optical and our MIR data. The optical image was taken with the WFPC2 instrument aboard the *Hubble* Space Telescope (HST), using the F606W filter. The MIR contours correspond to the NeIIref1 image, smoothed over 5 pixels. Alternating solid and dashed-dotted lines have been used for the contours in order to avoid confusion between different morphological features. The HST image shows the spiral structure of the host galaxy, with the AGN residing in the central bar. To the South, we find a very active SF region. Here, optical and mid-infrared morphologies are very similar. Two other MIR sources – one to the East and one to the Southwest of the nucleus, however, have only weak or no optical counterparts. In both cases, we likely

see SF that is embedded in thick layers of dust. The dust absorbs the emission of the hidden young stars and thermally re-emits in the MIR regime. It is interesting to note that the region of SF is neither aligned to the spiral arms of the galaxy, nor does it show the characteristic ring-like structure often found around AGN.

Such a ring of SF is found in **NGC 7469** as can be seen in fig. 5.27, where I show an overlay of an optical HST image and a VISIR NeIIref1 image. This overlay has been made in the same way as the one for NGC 5135. Again, we only find a partial coincidence of optical and MIR morphologies. Some of the less bright optical knots are strong MIR emitters, indicating SF covered by dust. It should be noted, however, that the S/N in the starburst ring is rather low, not allowing for a detailed matching of morphological features.

5.2 Comparison to Spitzer data

We have browsed the *Spitzer* science archive for low (spectral) resolution spectra of our sources, taken with the *Infrared Spectrograph* (IRS) (Houck et al., 2004) aboard the *Spitzer* Space Telescope. With its 85 cm mirror, the angular resolution of *Spitzer* is about 10 times less than the one of the VLT. On the other hand, space-born IR observatories are superior in terms of sensitivity and spectral coverage.

AGN have been among the primary targets for *Spitzer*. Therefore, many local AGN have been observed and IRS spectra are available in the archive. Such spectra allow us to look for mid-infrared emission lines and compare the spectral shapes and flux levels of our data to the spatially less resolved *Spitzer* observations. To this end, we downloaded reduced data and extracted the spectra with SPICE 2.0.4, using the "point source with regular extract" generic template. The absolute flux calibration was done by matching fluxes measured in different spectral settings for the same wavelengths. With this method, we achieved an absolute flux uncertainty of ~ 50 mJy. Especially large discrepancies between different spectral settings were found for Cen A, MCG-06-30-15 and NGC 3783. For NGC 4579 and NGC 5995, observations in only one spectral setting could be obtained.

In figs. 5.28, 5.29 and 5.30, we show IRS spectra and our VISIR photometry for all objects which we had observed in two or more different filters and for which IRS spectra were publicly available. We compare *Spitzer* and VISIR data of 9 type I AGN (fig. 5.28), 8 type II AGN (fig. 5.29) and 2 LINERs (fig. 5.30). The wavelength scale in all panels is in rest-frame, dotted vertical lines depict the positions of common mid-infrared emission lines: $7.7\,\mu$m PAH, $8.99\,\mu$m [ArIII], $9.67\,\mu$m H_2 (0-0)S3, $10.5\,\mu$m [SIV], $11.3\,\mu$m PAH and $12.81\,\mu$m [NeII].

Among the type I AGN, we find a good agreement between *Spitzer* and VISIR data, despite the difference in resolution by a factor of 10. The flux level is in significant disagreement only for Mrk 590, Mrk 509 and NGC 7469. Presumably, in these cases the IRS spectra contain contribution from SF around the nucleus. In NGC 7469, *Spitzer* is not able to resolve the SF ring we see with VISIR. The strong PAH and [NeII] emission lines in this object indicate the strong contribution of SF to the measured flux. In a number of other objects, *Spitzer* reveals the presence of H_2, PAH and [NeII] emission lines. In addition, Fairall 9, Mrk 590 and, especially, 3C 445 show pronounced silicate
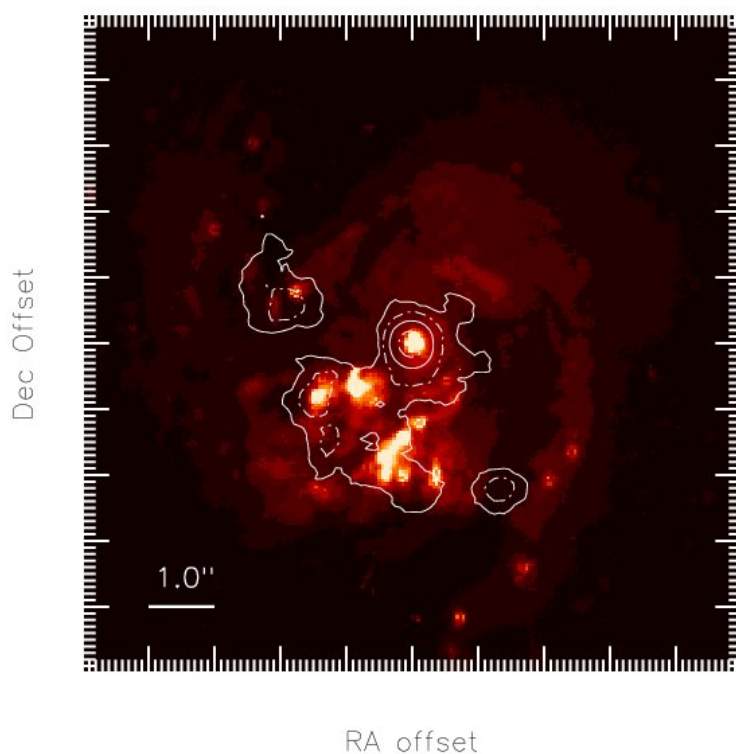
Figure 5.26: Overlay graphics, showing an HST image at 606 nm of NGC 5135 with over-plotted VISIR contours (NeIIref1 filter). The contour levels are displayed as alternating solid and dashed-dotted lines. The image shows the central $10'' \times 10''$, North is up and East is left. The VISIR contours only cover the central $6'' \times 6''$ of the displayed region.
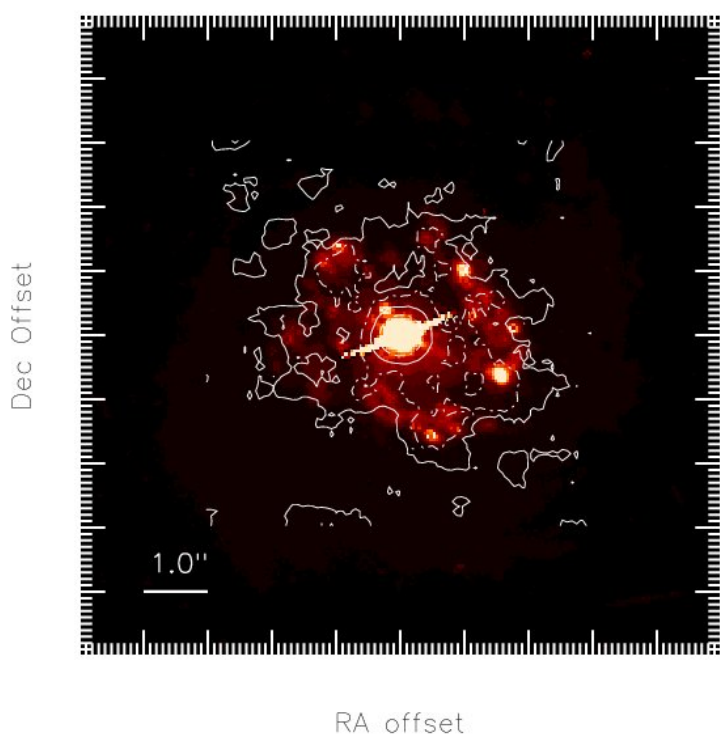
Figure 5.27: Overlay graphics, showing an HST image at 606 nm of NGC 7469 with over-plotted VISIR contours (NeIIref1 filter). The contour levels are displayed as alternating solid and dashed-dotted lines. The image shows the central $10'' \times 10''$, North is up and East is left. The VISIR contours only cover the central $6'' \times 6''$ of the displayed region.
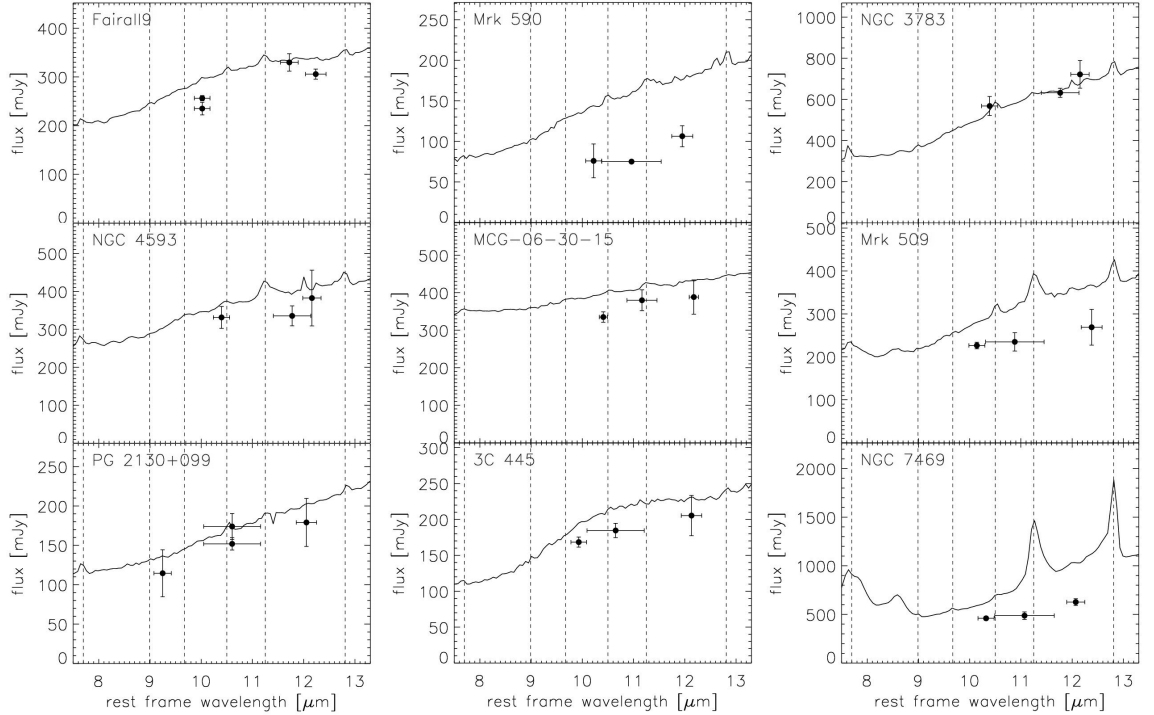
Figure 5.28: Comparison of low resolution *Spitzer* IRS spectra (solid lines) and our VISIR photometry (filled circles) for the Sy 1 AGN among our sample for which both datasets are available. Horizontal error bars correspond to the filter pass band. The absolute flux uncertainty of the IRS spectra is about 50 mJy. Dotted lines denote the position of common emission lines: $7.7\,\mu$m PAH, $8.99\,\mu$m [ArIII], $9.67\,\mu$m H$_2$ (0-0)S3, $10.5\,\mu$m [SIV], $11.3\,\mu$m PAH and $12.81\,\mu$m [NeII].

emission features. For the latter two objects, these are not present in the VISIR data and are, therefore, probably an extra-nuclear phenomenon. For MCG-06-30-015, the situation is reversed: The VISIR SED is indicative of a silicate emission feature while it is hardly present in the IRS spectrum.

For our type II sources, the IRS spectra show emission lines in every object. Especially remarkable is the spectrum of NGC 7679 which resembles the one a of starburst galaxy rather than an AGN. The VISIR photometry, however, does not appear to be significantly affected by SF as we do not find any indication for the presence of the $11.3\,\mu$m PAH line which is very strong in the IRS spectrum. For NGC 526a, IRAS 13197-1627, Cen A and PKS 2048-57, the shape of the VISIR SED had led us to assume that a pronounced silicate absorption feature is observed toward these objects. This seems to be true only for Cen A where the unusual spectral shape between $10\,\mu$m and $12\,\mu$m is caused by a superposition of a rising continuum and rather strong silicate absorption feature. In IRAS 13197-1627, PKS 2048-57, NGC 5995 and NGC 7314, the feature is only weakly pronounced. All other objects do not show it at all. Please note that in case of NGC 4507, a re-examination of the *Spitzer* dataset has shown that this observation was slightly
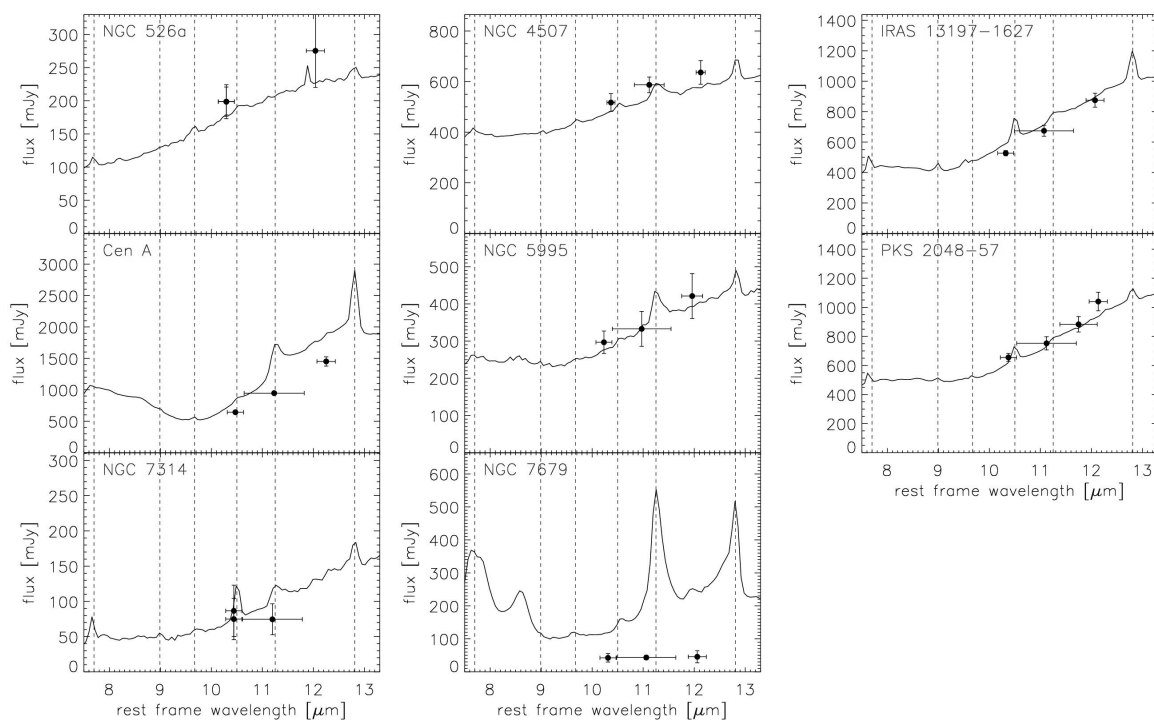
Figure 5.29: Comparison of low resolution *Spitzer* IRS spectra (solid lines) and our VISIR photometry (filled circles) for the Sy 2 AGN among our sample for which both datasets are available. Horizontal error bars correspond to the filter pass band. The absolute flux uncertainty of the IRS spectra is about 50 mJy. Dotted lines denote the same emission lines as in fig. 5.28.
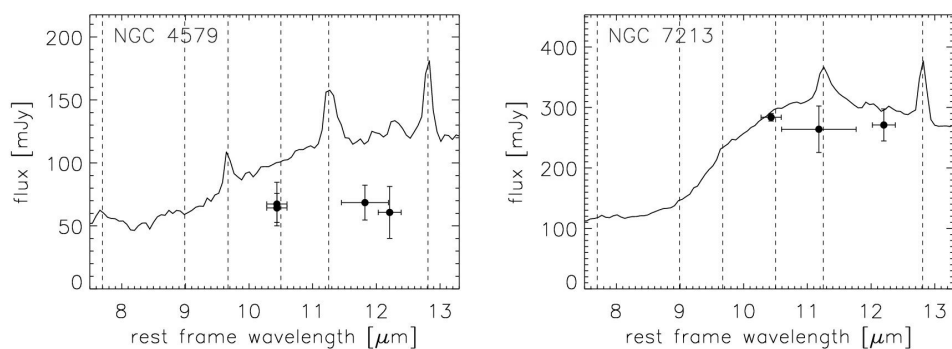
Figure 5.30: Comparison of low resolution *Spitzer* IRS spectra (solid lines) and our VISIR photometry (filled circles) for the LINER AGN among our sample for which both datasets are available. Horizontal error bars correspond to the filter pass band. The absolute flux uncertainty of the IRS spectra is about 50 mJy. Dotted lines denote the same emission lines as in fig. 5.28.

mis-pointed (M. Haas, private communication). Thus, the actual nuclear spectral shape might be different than shown in fig. 5.29. This would also explain why the VISIR fluxes are slightly larger than the IRS ones. It seems possible that the same has happened for PKS 2048-57 for which the fluxes measured with VISIR are slightly larger than the ones observed with IRS, as well.

The two LINERs in our sample appear quite differently in VISIR and *Spitzer* observations. The IRS spectrum of NGC 4579 shows a continuum that is rising toward the red while the VISIR measurements show a flat continuum. The strong [ArIII], PAH and [NeII] lines indicate the presence of active SF. Cold dust in the outer parts of a deeply embedded SF region could also explain the red continuum colour. In the case of NGC 7213, the continuum levels measured with VISIR and *Spitzer* are in agreement with each other. In the IRS spectrum, a silicate emission feature is superimposed onto the strong rise toward longer wavelengths. This feature appears to be absent in the VISIR photometry.

While a quantitative analysis of the difference in flux between IRS spectra and VISIR photometry is difficult due to the above mentioned problems with the flux calibration of the IRS data, we do find that in some cases the disagreement is significant. In some objects from our sample, e.g. in Mrk 590, NGC 7469, NGC 7679 and NGC 4579, roughly 50 % of the IRS continuum flux cannot be accounted for with VISIR and, thus, very likely originates in circumnuclear SF or other extra-nuclear phenomena. The case of Mrk 590 is of particular interest in this respect as the IRS spectrum does not exhibit strong emission lines indicative of star formation (i.e. PAH, [NeII]). The difference in flux is marginally compatible with the flux calibration uncertainty of the IRS and probably real. This would mean that the absence of such lines does not necessarily imply a spectrum to be free of contaminating, extra-nuclear emission.

5.3 Sample properties

After having presented the MIR properties of the individual targets in our sample, I will now present the properties of the whole sample. Before the statistical analysis of our results is put forward, I will discuss contamination of our MIR photometry. Finally, we have to explore the possibility of a redshift bias affecting our statistical results.

5.3.1 Possible contamination of our VISIR fluxes

A potential problem for our study is contamination by extra-nuclear emission. This is primarily important in the mid-infrared. AGN of moderate to high luminosities should always dominate their hosts in the 2-10 keV band. In the mid-infrared, on the other hand, star formation and also Narrow Line Region (NLR) clouds can significantly contribute to the total flux. The comparison between VISIR and *Spitzer* measurements shows that the contamination of IR fluxes can be of the same order as the AGN flux.

First of all, the high angular resolution (see Tables 4.1 and 4.2 for the physical scales we resolve) cuts away most of the star formation. As discussed in section 5.1, in three objects we find resolved star formation around the nucleus. In all cases, the separation between the nucleus and the SF regions is such that it would be resolved even in our most distant targets. Therefore, we are confident that emission from SF regions does
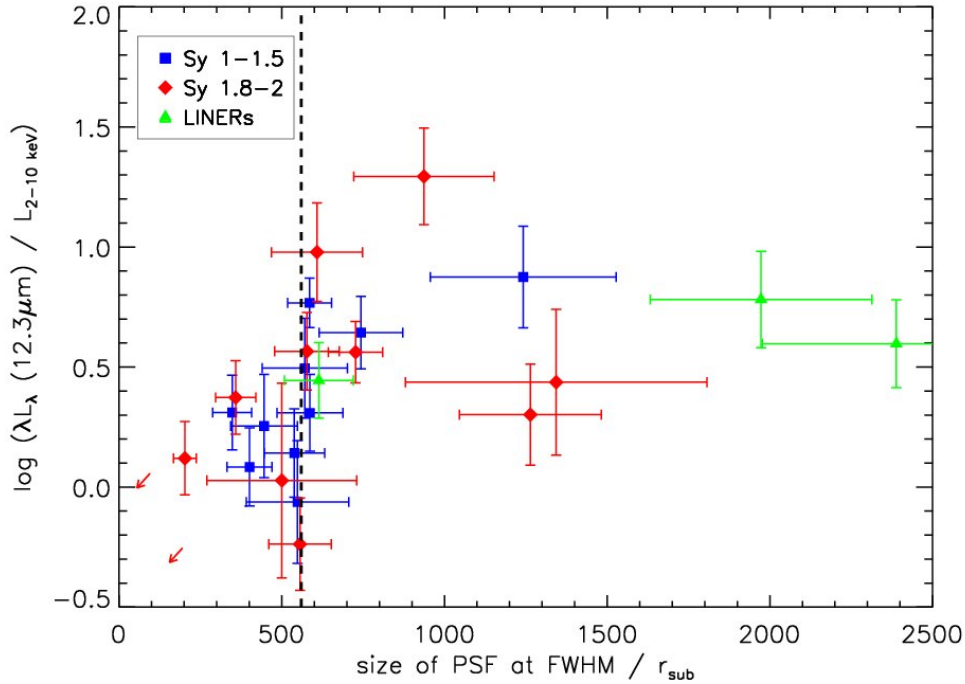
Figure 5.31: Luminosity ratio $L_{\mathrm{MIR}}/L_{\mathrm{X}}$ *vs* resolved scale in units of r_{sub}. Blue squares are type I Seyferts, red diamonds are type II Seyferts; green triangles are LINERS. Compton-thick objects are displayed as red arrows, non-detections in the infrared have been omitted. They would be positioned outside of the displayed region, toward higher luminosity ratios. The vertical dashed line indicates a resolution of $560 \cdot r_{\mathrm{sub}}$ above which the luminosity ratio rises.

not heavily affect our measurements. For NGC 5135 and NGC 7469, we inferred upper limits for such contamination of 15 % and 10 % of the measured flux, respectively. This is of the same order of magnitude as the photometric error.

Another potential source of contamination is the NLR which, in most of our sources, cannot be separated from the nucleus. The case of NGC 1068 shows that this may be a problem, as very accurate MIR photometry of this object (Galliano et al., 2005) show the NLR clouds to contribute almost 50 % of the nuclear MIR emission. Fortunately, three of our detected sources, namely NGC 4579, NGC 1097 and, most importantly, Cen A, are at comparable or even smaller distances than NGC 1068 and do not show any additional nuclear components. In addition, the high flux contribution of 50 % of the NLR in the NeII filter, measured by Galliano et al. (2005) seems to be mainly due to [NeII] line emission. In other filters, the level of contamination appears to be lower.

In order to test whether less resolved sources are affected by extra-nuclear emission, in fig. 5.31 we have plotted the MIR / X-ray luminosity ratio versus the resolved physical scale, expressed in units of the dust sublimation radius $r_{\mathrm{sub}} \propto L_{\mathrm{bol}}^{1/2}$ (see eq. 2.3). Here, we assume the accretion disc's bolometric luminosity to be $L_{\mathrm{bol}} = 10 \cdot L_{\mathrm{X}}$ which is a typical value for Seyfert galaxies (Vasudevan & Fabian, 2007). Interestingly, for observations

for which the size of the PSF at FWHM (in pc) is less than $560 \cdot r_{\mathrm{sub}}$, there is no case with $L_{\mathrm{MIR}}/L_{\mathrm{X}} > 0.4$, while this is the case for all but two objects with FWHM (pc) $> 560\, r_{\mathrm{sub}}$. We therefore use this resolution to separate our sample into well resolved and less resolved sources[1]. The mean luminosity ratios for the well resolved and the less resolved sources are (0.11 ± 0.19) and (0.65 ± 0.27), respectively. This difference indicates that some of our less resolved sources are, indeed, affected by contamination despite our high angular resolution.

Unsurprisingly, both IRAS 13197-1627 and NGC 5995 – the two objects which appear slightly extended in our VISIR images (see section 5.1 for details) – belong to the less resolved sources. Interestingly, this is also the case for all three LINERs in our sample.

5.3.2 Statistical analysis

In order to analyse the correlation between intrinsic hard X-ray and mid-infrared luminosity, for each object we have taken the photometry done closest to our reference wavelength of $12.3\,\mu$m in rest-frame and then converted to said wavelength by assuming the SED to be flat in this part of the spectrum. This wavelength was chosen as it is close to the peak of the MIR SED in AGN. In addition, is only affected by emission or absorption in one of the silicate features at $9.7\,\mu$m and $18\,\mu$m if these are particularly strong. Fortunately, we find indications for particularly strong silicate absorption only in Cen A. For this object, we cannot rule out that the measured continuum flux is slightly too low. All other objects exhibit only weak silicate features or none at all (see sections 5.1 and 5.2 for details).

The resulting monochromatic MIR luminosities, as well as the intrinsic 2-10 keV luminosities and hydrogen column densities are shown in table 5.1. Both luminosities are then plotted against each other in fig. 5.32. Please note that the X-ray error bars in this figure depict the uncertainty / variability of the respective sources as discussed in section 4.1 and are not measurement errors. The correlation between the two luminosities is of high statistical significance. After excluding non-detections and Compton-thick objects, the Spearman rank coefficient (Spearman, 1904) is $\rho = 0.90$ at a significance level of $7.3 \cdot 10^{-9}$. We can, therefore, safely reject the null hypothesis of no intrinsic correlation. We fitted a power-law to the data and excluded NGC 526a and NGC 7314 because of the large inclination angles of their host galaxies. Thus, the fit includes 10 type 1s, 10 type 2s and 3 LINERs. The best power-law fit obtained for this sample is $\log L_{\mathrm{MIR}} = (-1.61 \mp 1.85) + (1.04 \pm 0.04) \log L_{\mathrm{X}}$. For all objects not detected with VISIR, the 3σ flux limits are compatible with this correlation, including the two low luminosity objects NGC 4303 and NGC 4698.

In order to ensure that this result is not affected by contamination of our VISIR fluxes, as discussed in section 5.3.1, we have recalculated the mid IR – hard X-ray correlation, only using well resolved objects with FWHM (pc) / $r_{\mathrm{sub}} \leq 560$ (encircled objects in fig. 5.32). The resulting $\log L_{\mathrm{MIR}} = (-3.89 \mp 3.68) + (1.09 \pm 0.09) \log L_{\mathrm{X}}$ is in very good agreement with the correlation found for the whole sample. This method allows us to say with some confidence that objects situated close to this fit (dashed line in fig. 5.32) are not affected by contamination.

---

[1]It is important to note that in all cases, the torus itself remains unresolved. The term "well resolved" has to be understood in terms of the nuclear region of the host galaxy, not the AGN itself.

Table 5.1: Mid-IR, hard X-ray luminosities, intrinsic hydrogen column densities and resolved scale for our combined AGN sample. The $12.3\,\mu$m luminosities have been computed from the fluxes given in tables 4.3 and 4.4; the hard X-ray luminosities and hydrogen column densities have been compiled from the literature (see section 4.1 for details). The resolved scale was computed using the values given in tables 4.3 and 4.4 together with eq. 2.3.

Object Name	$\log \mathrm{L_{2-10keV}}$ [erg/s]	$\log \lambda \mathrm{L}_\lambda$ at $\lambda = 12.3\,\mu$m [erg/s]	N_H [10^{21} cm^{-2}]	Scale [r_sub]
MCG-01-01-043	42.50 ± 0.15	≤ 44.52	$0.327^{+0.274}_{-0.0}$	2249
Fairall 9	43.87 ± 0.15	44.51 ± 0.01	0.3 ± 0.02	743
NGC 526a	43.14 ± 0.10	43.70 ± 0.08	1.33 ± 0.14	726
Mrk 590	43.61 ± 0.25	43.55 ± 0.05	n/a	558
NGC 1097	40.80 ± 0.15	41.40 ± 0.10	$1.3^{+0.4}_{-0.3}$	2389
NGC 3783	43.21 ± 0.15	43.52 ± 0.04	n/a	348
NGC 4303	39.16 ± 0.15	≤ 42.40	n/a	18412
NGC 4472	≤ 19.17	≤ 41.62	n/a	n/a
NGC 4507	43.30 ± 0.15	43.67 ± 0.03	292 ± 23	358
NGC 4579	41.10 ± 0.15	41.88 ± 0.13	≤ 0.2	1973
NGC 4593	42.93 ± 0.20	43.18 ± 0.08	0.169	446
NGC 4698	39.08 ± 0.30	≤ 42.54	≤ 4.0	11536
NGC 4941	41.30 ± 0.50	41.74 ± 0.05	450^{+250}_{-140}	1343
IRAS 13197-1627	42.78 ± 02.0	44.07 ± 0.02	390 ± 40	937
Cen A	41.68 ± 0.15	41.80 ± 0.03	100 ± 30	202
NGC 5135	43.00 ± 0.50	43.06 ± 0.04	> 1000	601
MCG-06-30-015	42.57 ± 02.0	43.07 ± 0.05	3.5 ± 1.1	469
NGC 5995	43.54 ± 0.15	44.11 ± 0.06	$9.0^{+0.5}_{-0.3}$	577
ESO 141-G55	43.90 ± 0.15	44.04 ± 0.11	n/a	539
Mrk 509	44.10 ± 0.15	44.18 ± 0.06	n/a	401
PKS 2048-57	42.84 ± 0.20	43.82 ± 0.04	237 ± 20	608
PG 2130+099	43.65 ± 0.20	44.53 ± 0.07	n/a	1242
NGC 7172	42.76 ± 0.40	42.79 ± 0.07	83 ± 2	500
NGC 7213	42.23 ± 0.15	42.67 ± 0.05	n/a	614
3C 445	44.19 ± 0.15	44.50 ± 0.06	250 ± 136	541
NGC 7314	42.20 ± 0.15	41.96 ± 0.12	7.2 ± 1.0	556
NGC 7469	43.15 ± 0.10	43.92 ± 0.02	n/a	585
NGC 7674	44.56 ± 0.50	44.31 ± 0.02	> 10000	205
NGC 7679	42.52 ± 0.15	42.82 ± 0.15	$0.22^{+0.18}_{-014}$	1264
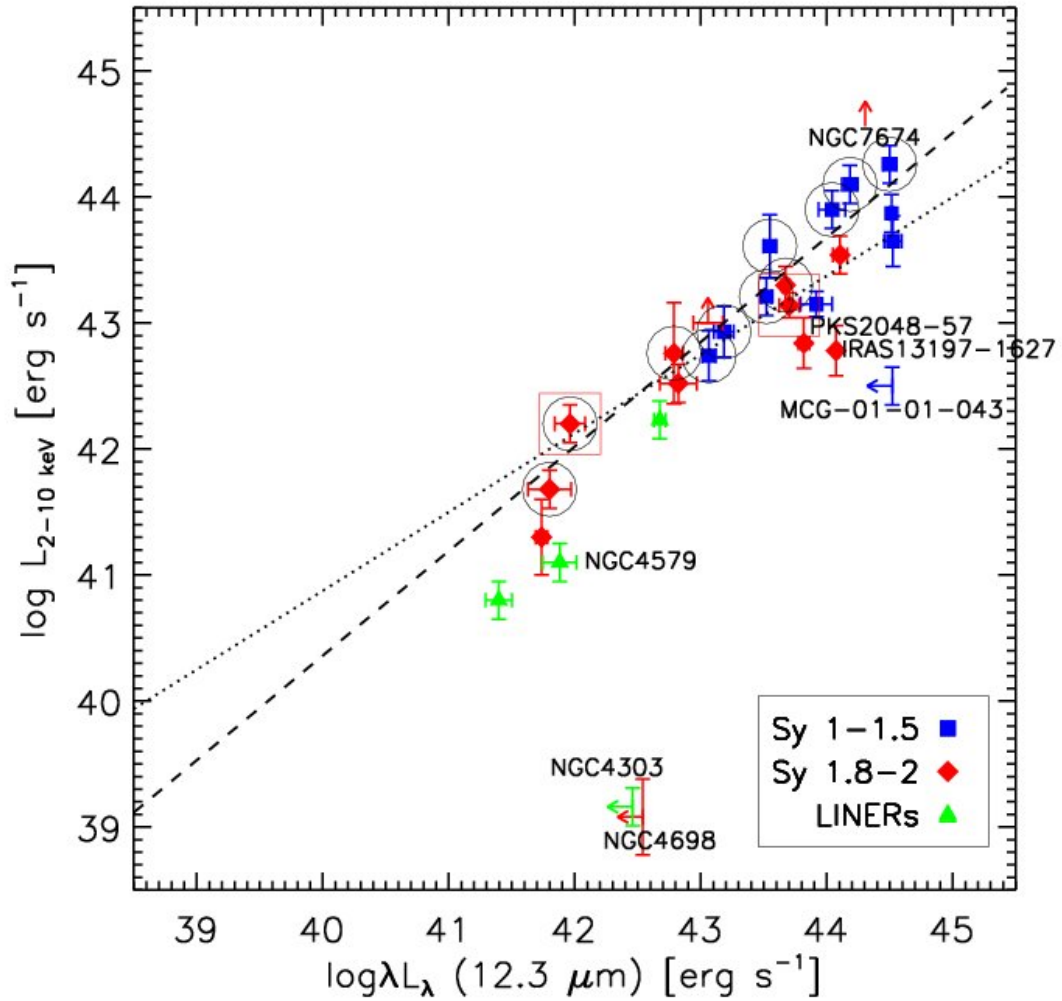
Figure 5.32: Correlation of MIR and absorption-corrected hard X-ray luminosities for our VISIR
sample. Blue squares are type I Seyferts (type 1.5 or smaller), red diamonds are type II Seyferts;
green triangles are LINERs. The two galaxies with large inclination angles (see section 4.1) are
marked by a red square. Well resolved objects (see section 5.3.1 for details) are marked by a
black circle. These have been used for the displayed power-law fit (dashed line); the dotted line
is the best fit to our first sample, as discussed in Horst et al. (2006). Arrows indicate either
upper limits to the MIR luminosity or lower limits to the X-ray luminosity; the arrows' colour
code corresponds to the one of the other symbols. Note that NGC 4472 is not shown here since
neither its X-ray nor MIR luminosities could be determined.

Figure 5.33: Luminosity ratio $L_{\mathrm{MIR}}/L_{\mathrm{X}}$ *vs* intrinsic column density N_{H}. Symbols and colours are as in fig. 5.31. Compton-thick objects are displayed as red arrows, non-detections in the infrared have been omitted. They would be positioned outside of the displayed region, toward higher luminosity ratios. Objects with no measured intrinsic absorption have been placed at $N_{\mathrm{H}} = 10^{19.5}$ cm^{-2} for clarity.

We also plotted the best fit correlation to our first sample of 8 objects, as published in Horst et al. (2006), into fig. 5.32. It is important to note that the slope of the correlation has changed considerably. After excluding NGC 4579 due to its peculiar nature, our first sample yielded $L_{\mathrm{MIR}} \propto L_{\mathrm{X}}^{1.60\pm0.22}$ which is consistent with our new slope at the 3σ level. The discrepancy in slope is caused by our first sample being small and containing some objects (i.e. PKS 2048-57) which are off the correlation for the enlarged sample. The latter agrees well with the results of the earlier studies by Krabbe et al. (2001) and Lutz et al. (2004).

In fig. 5.33 we show the luminosity ratio $L_{\mathrm{MIR}}/L_{\mathrm{X}}$ *vs* the intrinsic column density N_{H} toward the AGN. There is no correlation discernible between the two displayed quantities. Neither do we find a significant dependence of the luminosity ratio on Seyfert type: $\langle \log L_{\mathrm{MIR}} - \log L_{\mathrm{X}} \rangle$ is (0.38 ± 0.31) for type Is, (0.44 ± 0.45) for type IIs and (0.61 ± 0.17) for the three detected LINERs in our sample. We tested for a possible dependence of luminosity ratio on column density by computing the Spearman rank coefficient for it. With a result of $\rho = 0.13$ at a significance level of 0.54, we find no evidence for a correlation between the two quantities. Furthermore, we performed a Kolmogorov-Smirnov test for the luminosity ratios of type I and type II Seyferts. The maximum difference in the cumulative distribution function is 0.2 and the significance level 0.97 which means both samples very likely originate from the same parent distribution. These

Figure 5.34: Correlation of MIR and hard X-ray fluxes. Symbols and colours are as in fig. 5.32. Compton-thick objects and MIR non-detections are indicated by arrows; these have the same colour code as the symbols.

numbers imply that type Is and type IIs follow the same $L_{\mathrm{MIR}} - L_{\mathrm{X}}$ correlation and have the same average luminosity ratio.

5.3.3 Physical Significance of the $L_{\mathrm{MIR}} - L_{\mathrm{X}}$ correlation

One concern with correlations between luminosities is that they may be caused by a redshift bias in the data. In most AGN samples, more luminous objects are more distant, too. This is due to selection effects on one hand (low luminosity sources can only be detected if they are relatively nearby) and cosmic evolution on the other hand. In observational studies we have to infer the luminosity of each object from its flux and its distance. If the more distant objects are also more luminous, the multiplication of uncorrelated fluxes with the same luminosity-dependent distances can mimic a correlation between the luminosities. We tested for this possibility in two ways. First of all, we analysed the formal correlation between MIR and hard X-ray fluxes, shown in fig. 5.34. The resulting Spearman rank coefficient is $\rho = 0.52$ at a significance level of 0.01. This means that the correlation is rather weak but, nevertheless, highly significant.

Interestingly, for the well resolved sources (encircled objects in fig. 5.34), we find the correlation between the measured fluxes to be much stronger than for the complete sample. Its Spearman rank is $\rho = 0.92$ and the significance level = $5 \cdot 10^{-4}$. This is another indication that these fluxes are mostly free of contamination.

Secondly, we tried to reproduce the observed correlation between luminosities with randomly generated mock data. For this, we assumed X-ray and MIR flux values to be uniformly distributed over the range of observed ones, for the distances we tried both a uniform and a normal distribution with no significant change in the result: After generating 10^4 mock datasets of 25 objects each, a rank coefficient of $\rho > 0.89$ for the MIR – hard X-ray correlation was found with a frequency of less than 0.1 %, a significance level of less than $7.4 \cdot 10^{-9}$ with a frequency of less than 0.15 %. A histogram of Spearman
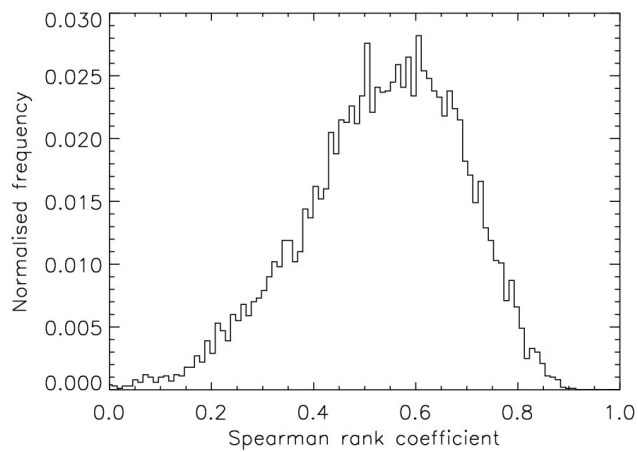
Figure 5.35: Spearman rank coefficients resulting from random data. 10 000 datasets with 25 pairs of X-ray and MIR fluxes each, were analysed. The Spearman coefficient of the observed data is 0.90.

coefficients resulting from random data is shown in fig. 5.35.

The combination of both results – the high significance of the flux – flux correlation and the low probability of reproducing the observed luminosity – luminosity correlation with non-correlated data – implies that we can safely assume the correlation to be real and not caused by a redshift bias in our data.

6 Discussion

When a scientist doesn't know the answer to a problem, he is ignorant. When he has a hunch as to what the result is, he is uncertain. And when he is pretty damn sure of what the result is going to be, he is still in some doubt. We have found it of paramount importance that in order to progress, we must recognize our ignorance and leave room for doubt. Scientific knowledge is a body of statements of varying degrees of certainty – some most unsure, some nearly sure, but none absolutely certain.

Richard P. Feynman: What Do You Care What Other People
Think? (1988)

In the previous chapter, I have presented the results of our observational campaign, both on individual objects and on the properties of the whole sample. In this chapter, I will now discuss these results, first with respect to similar studies by other groups and then in terms of the physical and geometrical properties of the obscuring tori in AGN.

In section 6.1, I will discuss the impact of angular resolution on IR studies and then compare our results to those of other authors. Then, in section 6.2, I will present the implications of our findings, first of the similarity in the appearance of type I and type II AGN (section 6.2.1), then of the slope we find in the mid-IR – hard X-ray correlation (6.2.2). In section 6.2.3, I will present some other aspects of our results with respect to AGN unification.

6.1 Comparison of our work with related studies

6.1.1 The impact of angular resolution on AGN studies in the MIR

One of the main improvements of our project compared to earlier studies of the MIR – hard X-ray correlation is the increase in angular resolution. The resolution of our VISIR images are ~ 5 times better than the data of Krabbe et al. (2001) and ~ 80 times better than the ISOPHOT spectra of Lutz et al. (2004). Thus, for the first time, we can perform such a study with sub-arcsecond resolution in MIR.

The tradeoff for the high resolution is a reduced sensitivity and spectral coverage when compared with the capabilities of IR space missions, in particular the *Spitzer* Space Telescope. *Spitzer* IRS spectra are available for many AGN and some authors have used

these to perform similar studies as our own (Buchanan et al., 2006). Others (Lutz et al., 2004; Ramos Almeida et al., 2007) even used archival ISO data for similar purposes. Therefore, we have to test whether our approach is justified and can generate results one could not have obtained with data from IR space observatories.

A major motivation for our work was a statement by Lutz et al. (2004) that the large scatter they observed for the MIR – hard X-ray correlation may be due to contamination in their large $24'' \times 24''$ aperture. Such contamination, in turn, could mask a difference in the nuclear $L_{\mathrm{MIR}}/L_{\mathrm{X}}$ ratio for different Seyfert types. The SF regions we find in three of our objects, as well as the implications of fig. 5.31 illustrate the need for high angular resolution MIR studies for testing AGN models. Even using 8m-class telescopes, a good sample selection is crucial to avoid contamination by non-AGN emission. This indicates that the large scatter found by Lutz et al. may, indeed, be caused by the poor angular resolution of their ISOPHOT data.

To less extent, the same problem applies to studies with ISOCAM or *Spitzer*. As we have seen in section 5.2, the MIR appearance of AGN can, indeed, be quite different for angular resolutions of $3.0''$ (*Spitzer*) and $0.35''$ (VISIR). For the two cases of NGC 5135 and NGC 7469, we find that within $3''$ from the nucleus, SF contributes at least 43 % and 45 % of the total continuum flux at $12.3\,\mu$m, respectively. For NGC 7469, this number is also in good agreement with the difference in flux level between IRS and VISIR data as shown in fig. 5.28. Figures 5.28 to 5.30 also show that not only may the AGN continuum flux be overestimated in poorly resolved IR observations, even spectral features can be misinterpreted. By now, it has been widely accepted that strong emission lines as PAH and [NeII] usually originate in the circumnuclear region rather than the AGN itself. A more serious problem is the change in appearance of the silicate feature, for instance in 3C 445 or NGC 7213. These cases raise the question whether detailed comparison between IR spectra recorded with *Spitzer* and radiative transfer calculations for dust tori (as has been done e.g. by Fritz et al., 2006; Levenson et al., 2007) can lead to anything more than very general insights into the geometry of the obscuring medium. It does not appear reasonable to use potentially heavily contaminated data to constrain the properties of the torus itself. Therefore, while the benefits of *Spitzer* data for exploring the properties of nuclear regions in active galaxies cannot be overestimated, I do believe that a high angular resolution approach is necessary for assessing the properties of the AGN itself.

6.1.2 Results from other studies

A couple of groups have done work along similar lines as the present one and it is, of course, important to compare the results of these authors with our own. As has been mentioned, the mid-infrared – hard X-ray correlation we find is in good agreement with the results of Krabbe et al. (2001) and Lutz et al. (2004). Actually, both groups do not perform a least-square fit to their data but simply assume the slope of the correlation to be 1. In any case, this is very close to our result $\log L_{\mathrm{MIR}} \propto (1.04 \pm 0.04)\log L_{\mathrm{X}}$. Furthermore, in both studies, no difference in the $L_{\mathrm{MIR}}/L_{\mathrm{X}}$ ratio was found for different Seyfert types. This, again, is in very good agreement with our results. The main difference between our results and those obtained by Lutz et al. is the reduced scatter in the correlation of our data. As discussed in the previous section, this is likely to be an effect
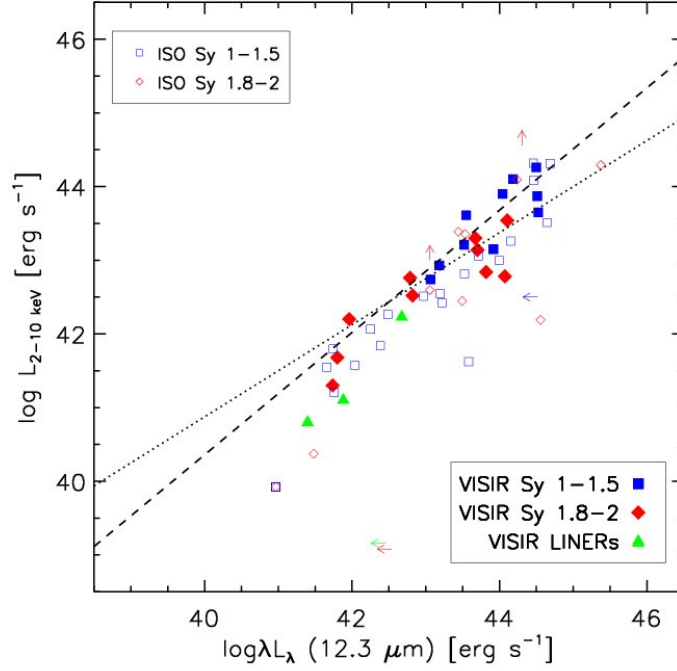
Figure 6.1: Comparison of VISIR and ISOPHOT data on the mid IR – hard X-ray correlation. Open symbols denote data taken from Lutz et al. (2004), filled symbols are the results of the present work. Blue squares are type I AGN, red diamonds are type II AGN and green triangles are LINERs. Arrows indicate either Compton-thick objects or non-detections in the MIR; they have the same colour coding as the symbols. The dashed line is the best-fit to our whole dataset (see section 5.3.2 for details), the dotted line is the best fit to our first sample, as discussed in Horst et al. (2006).

of the improved angular resolution in our study. In addition, we applied much stricter target selection criteria than Lutz et al did. In fig. 6.1, we show our own data together with the one obtained by Lutz et al. Both datasets seem to follow the same trend with a tendency of the ISOPHOT data to exhibit larger MIR luminosities and to have more outliers. These differences can be well explained by the difference in angular resolution (e.g. see fig. 5.31).

Very recently, Ramos Almeida et al. (2007) published a work on ISOCAM data first published by Clavel et al. (2000) and the X-ray data that was compiled by Lutz et al. (2004). For MIR observations taken at $6.75\,\mu$m, they find $\log L_{\mathrm{MIR}} \propto 1.25 \log L_{\mathrm{X}}$ (no error stated) and, furthermore, report to have found a difference in $L_{\mathrm{MIR}}/L_{\mathrm{X}}$ for Seyfert 1 and Seyfert 2 galaxies. They find $\langle \log L_{\mathrm{MIR}} - \log L_{\mathrm{X}} \rangle = 1.62 \pm 0.35$ for type Is and $\langle \log L_{\mathrm{MIR}} - \log L_{\mathrm{X}} \rangle = 1.19 \pm 0.67$ for type IIs and state that "both distributions appear significantly different according to the Kolmogorov-Smirnov test". With the 1σ (?) errors of both ratios overlapping, however, the difference can be marginal at best.

Ramos-Almeida et al. perform a brightness profile decomposition of their data to extract the nuclear fluxes. However, as discussed above, with a resolution of $\sim 4.3''$ they
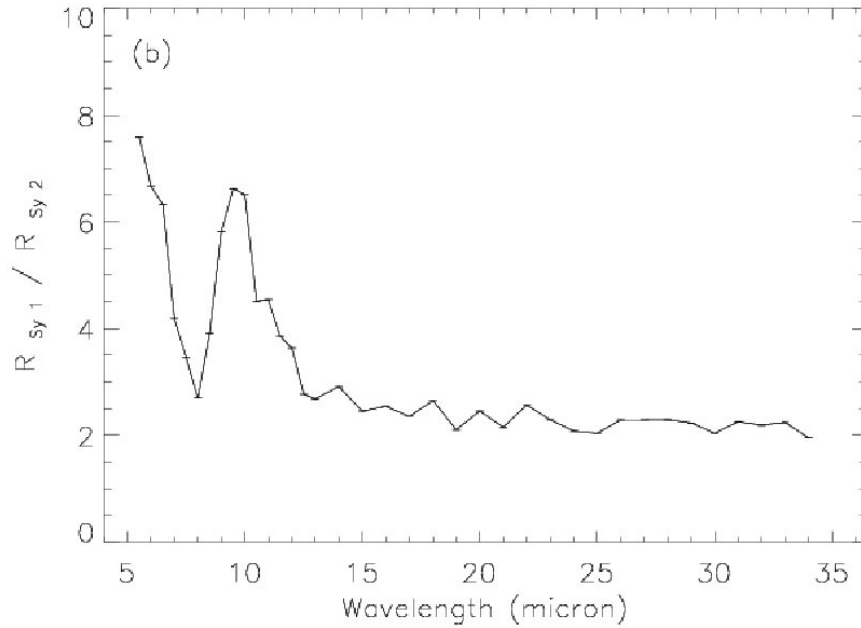
Figure 6.2: Difference in $R = \log F_{\mathrm{MIR}} / \log F_{8.4\mathrm{GHz}}$ between type I and type II AGN, plotted over MIR wavelength. This figure has been reproduced from Buchanan et al. (2006).

are simply not able to distinguish between emission from the AGN and a circumnuclear star forming region. Furthermore, the fact that the luminosity ratios Ramos Almeida et al. (2007) derive are ~ 8 times larger than what we find for our well resolved objects – and despite their shorter observing wavelength in the IR and MIR SEDs of AGN generally rising toward longer wavelengths – indicates that they are probably affected by contamination and the MIR fluxes they report are likely not dominated by torus emission.

A similar claim as the one by Ramos-Almeida et al. was made by Buchanan et al. (2006). As a measure for the intrinsic luminosity of the AGN, these authors use 8.4 Ghz radio continuum instead of absorption corrected hard X-rays. They find a difference in the $F_{\mathrm{MIR}}/F_{8.4\mathrm{GHz}}$ flux ratio between Sy 1 and Sy 2 galaxies for all MIR wavelengths. As they note themselves, however, the statistical significance of this difference is small (no number stated) at wavelengths longer than $\sim 12\,\mu$m. In fig. 6.2, I reproduce panel b) of their fig. 16. Here, it is apparent that the luminosity ratios mainly differ at short MIR wavelengths and around the $9.7\,\mu$m silicate feature. At $12.3\,\mu$m, their results are roughly consistent with ours. They are, however, in disagreement with the ones by Lutz et al. (2004). Buchanan et al. (2006) argue that this is probably due to the larger aperture of ISOPHOT compared to their *Spitzer* spectra (an argument that I repeat here with respect to their own data when compared to ours) as well as different systematic effects in both studies.

We can conclude that the results of other studies do either agree or marginally disagree with the ones presented here. In the latter cases, a lack of angular resolution in the ISO

or *Spitzer* data makes it seem likely that their nuclear IR fluxes are contaminated by non-AGN emission and, thus, the obtained flux ratios are not representing the intrinsic properties of the dusty torus.

6.2 Implications for the state of the torus

In the previous section, I have established the validity of our results. Thus, having set the stage, we can now interpret our findings in terms of the physical and geometrical properties of the torus. First of all, the fact that we find a close correlation between L_{MIR} and L_{X} with little intrinsic scatter is in agreement with the prediction that every AGN contains a molecular and dusty torus and, thus, is an affirmation of the orientation-based unification scheme for AGN. In the following, I discuss the meaning of the properties of the correlation.

6.2.1 $L_{\mathrm{MIR}} - L_{\mathrm{X}}$ for Sy 1s and Sy 2s

In section 5.3.2, I have shown that the average luminosity ratios $L_{\mathrm{MIR}}/L_{\mathrm{X}}$ for Sy 1 and Sy 2 galaxies do not significantly differ from each other. Furthermore, $L_{\mathrm{MIR}}/L_{\mathrm{X}}$ shows no dependence on N_H – and so over 4 orders of magnitude in N_H (see fig. 5.33). Even the two Compton-thick objects in our sample, NGC 5135 and NGC 7674, seem to have roughly the same value of $L_{\mathrm{MIR}}/L_{\mathrm{X}}$ as the rest of our sample. For these objects, however, strong conclusions cannot be drawn, as their X-ray luminosities can only be estimated to an uncertainty of one order or magnitude.

This result is in clear disagreement with theoretical predictions for smooth dust tori. For an optically thick smooth torus, a much higher $L_{\mathrm{MIR}}/L_{\mathrm{X}}$ is expected for Sy 1s than for Sy 2s. Pier & Krolik (1993) expect a difference of one order of magnitude for a change of N_{H} from $\sim 10^{20}$ cm^{-2} to $\sim 10^{24}$ cm^{-2}. The reason for this effect is that in Sy 2s the observer sees the emission from the cold dust in the outer part of the torus, while in Sy 1s he has a line of sight toward its hot inner part as well.

It is important to note that the similarity between Sy types still holds if we only regard objects with FWHM (pc) / $r_{\mathrm{sub}} \leq 560$ (see section 5.3.1 for details). For these, we find $\langle \log L_{\mathrm{MIR}} - \log L_{\mathrm{X}} \rangle$ to be (0.15 ± 0.15) for type 1s and (0.07 ± 0.25) for type 2s.

Models of clumpy tori (Nenkova et al., 2002; Dullemond & van Bemmel, 2005; Hönig et al., 2006) at $12\,\mu$m, do not predict such a difference in $L_{\mathrm{MIR}}/L_{\mathrm{X}}$ between different Sy types. In particular, Hönig et al. (2006), using 3D radiative transfer modeling, showed that clumpy tori can appear as optically thin in the MIR with most of the radiation originating in the innermost part of the torus. In their model, individual clouds are optically thick but their volume filling factor is small. Our observational results prefer this kind of models to smooth ones.

Please note, that clumpy torus models are not contradicted by the results of Buchanan et al. (2006). In fact, Buchanan et al. themselves state that their findings prefer clumpy models as well: Outside of the silicate feature the measured difference in $F_{\mathrm{MIR}}/F_{8.4\mathrm{GHz}}$ for type I and type II sources is much less than predicted e.g. by Pier & Krolik (1993). For the silicate feature and wavelengths shorter than $\sim 5\,\mu$m, on the other hand, even clumpy models predict anisotropy.

Thus, the isotropic appearance of AGN in the mid infrared regime that we find, gives support to clumpy torus models instead of smooth ones and adds to the evidence presented in section 2.3. Furthermore, the volume filling factor of clouds in the torus has to be low to make the torus appear as optically thin in the MIR. This also means that the height of the torus is likely supported by the dynamics of the individual dust clouds (Beckert & Duschl, 2004) and not mainly by radiation pressure (Pier & Krolik, 1992; Krolik, 2007).

6.2.2 Interpreting the slope of the correlation

As discussed in section 2.3.4, MIR and hard X-ray luminosities have a close physical connection. The hard X-ray luminosity is a good proxy for the bolometric luminosity of the accretion disc (see Vasudevan & Fabian, 2007, for a recent account on bolometric corrections). And as the mid-IR radiation is accretion disc emission reproduced by the dusty torus, L_{MIR} and L_{X} are directly linked to each other. If we can assume the torus to appear as optically thin in the MIR which is implied by the results discussed above, the relation between the two quantities is:

$$L_{\mathrm{MIR}} \propto f_C L_{\mathrm{X}}, \tag{6.1}$$

where f_C is the covering factor of the torus in terms of solid angle.

Thus, our best-fit result implies $f_C \propto L_{\mathrm{X}}^{0.04 \pm 0.04}$. This means that we do not find any dependence of f_C and hence $L_{\mathrm{MIR}}/L_{\mathrm{X}}$ on L_{X} which is also illustrated by fig. 6.3. This result does not match the expectations from the receding torus model (Lawrence, 1991) for which Simpson (2005) found the fraction of type 2 AGN f_2 to depend on AGN luminosity as $f_2 \propto L_{\mathrm{X}}^{-0.27}$ for $L_{\mathrm{X}} \gtrsim L_0 \approx 7 \cdot 10^{43}$ erg s^{-1} (see section 2.3.3). The basic assumption of the unified scenario is that $f_2 \approx f_C$. The dependence derived by Simpson would, thus, yield a correlation $f_C \propto L_{\mathrm{X}}^{-0.27}$ which disagrees with the slope we find by more than 7σ. Note, however, that we do not probe the Quasar regime of luminosities, i.e. for a break luminosity $L_0 \gtrsim 10^{45}$ erg s^{-1} the receding torus model would, again, agree with our results.

For the luminosity range covered by our observations, we find a constant covering factor f_C. With eq. 2.5, we then find that the flaring parameter $\alpha \approx 1$ and the scale height $h(r)/r$ is constant. Thus, qualitatively, the torus has the geometry depicted in panel c) of fig. 2.3.

One possibility to reconcile our findings with the obvious dependence of the type I fraction on AGN luminosity (Simpson, 2005, and references therein) would be that a significant number of Compton-thick AGN at moderate luminosities ($L_{2-10\mathrm{keV}} = 10^{43} \sim 10^{44}$ erg s^{-1}) have been missed in hitherto existing X-ray surveys. Such a population would affect the observed type I / type II ratio but not our own results. We would only have to change our interpretation of the slope of the MIR – hard X-ray correlation if Compton-thick AGN had a $L_{\mathrm{MIR}}/L_{\mathrm{X}}$ ratio that significantly differs from the luminosity ratio of other AGN. So far, we see no indication for that (see fig. 5.33). In an observing programme that is currently being executed at the VLT, we aim to put tighter constraints on the MIR / hard X-ray ratio of Compton-thick AGN; for more details on this programme, consult section 8.3.
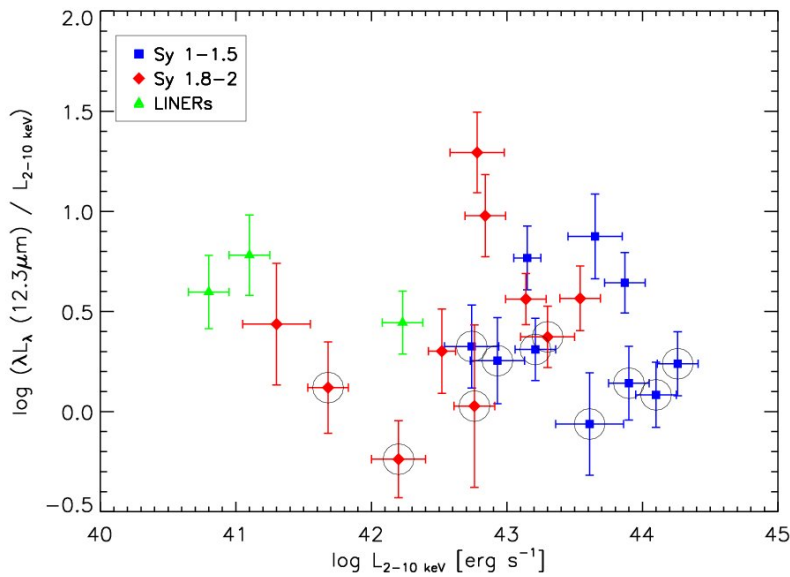
Figure 6.3: Luminosity ratio $\log(L_{\mathrm{MIR}}/L_{\mathrm{X}})$ *vs* hard X-rax luminosity $\log L_{\mathrm{X}}$. Colours and symbols are as in Fig. 6.1. Black circles mark well resolved sources with FWHM(pc) / $r_{\mathrm{sub}} \leq 560$ (see section 5.3.1 and fig. 5.31). Compton-thick objects and MIR non-detections have been omitted.

The existence of a population of Compton-thick AGN has also been suggested by recent X-ray surveys (e.g. the COSMOS survey, Hasinger et al., 2007), X-ray background synthesis (e.g. Gilli et al., 2007; Gandhi et al., 2007) and IR surveys (Martínez-Sansigre et al., 2005). Such a population can be constrained by observations of the X-ray background and we know that the number of very luminous Compton-thick objects has to be low (see e.g. Treister et al., 2006). The margin for less luminous objects, however, is much larger and a significant population could exist without radiating in excess of the observed background.

Very recently, Ueda et al. (2007) randomly selected two AGN out of those first detected by *Swift* to be observed with *Suzaku* and found both of them to be highly obscured. This is another indication for the existence of a large population of Compton-thick AGN at moderate luminosities.

6.2.3 Other aspects of AGN unification

Dust tori at low luminosities   In section 2.2.3, I noted that, incidentally, the two very different torus models by Elitzur & Shlosman (2006) and Hönig & Beckert (2007), both predict that AGN tori are not stable at bolometric AGN luminosities below $L_{\mathrm{low}} \approx 5 \cdot 10^{42}$ erg s^{-1}. From this prediction we would expect low luminosity AGN to appear differently in the IR. The naive expectation is for the $L_{\mathrm{MIR}}/L_{\mathrm{X}}$ ratio to decrease as the IR emitting torus is missing. In fig. 5.32, we indeed see a weak tendency for objects with $L_{\mathrm{X}} \lesssim 5 \cdot 10^{42}$ erg s^{-1} to deviate from the correlation. They, however, show an increase in $L_{\mathrm{MIR}}/L_{\mathrm{X}}$

rather than a decrease. I should note that none of these low luminosity objects belongs to the well resolved objects discussed in section 5.3.1 which means that their deviation from the correlation could simply be caused by contamination of the observed MIR flux. Moreover, as we can see in fig. 6.3, the deviation of these low luminosity objects does not exceed the scatter among other contaminated objects.

An interesting test case for the behavior of low luminosity AGN is the well studied LINER NGC 4579 (highlighted in fig. 5.32). Contini (2004) analysed emission line ratios in the optical spectrum of this object and came to the conclusion that the MIR continuum of NGC 4579 is dominated by thermal emission of the shock heated ISM in the vicinity of the AGN. First of all, this supports the hypothesis that the deviation from the correlation is caused by contamination – in this case emission from the ISM. Nevertheless, if we would find this kind of contamination in all low luminosity AGN, this would imply a physical connection between the absence of a obscuring torus and gas outflows from the AGN. At the moment, however, our data is not sufficient to constrain the properties of this class of objects. Future observations are required to settle this question.

The role of LINERs LINERs are one of the more enigmatic classes of AGN. For a long time, it has been unclear whether they are predominantly powered by AGN or starburst activity. Some LINERs – among them NGC 4579 – exhibit broad optical emission lines, indicative of accretion activity in their centres. Others contain X-ray sources which are too luminous to be X-ray binaries and thus have to be AGN as well. Apart from the erroneously selected NGC 4472, all LINERs in our sample belong to this class of objects.

Recent X-ray studies of local LINERs by Flohic et al. (2006) and González-Martín et al. (2006) have found proof for the existence of an AGN in $\sim 60\%$ of all observed objects. The remaining LINERs might contain Compton-thick AGN, but are probably powered by star formation. Sturm et al. (2006) have investigated the MIR properties of a sample of LINERs with *Spitzer* and found the population to be separated into IR-faint LINERs which are probably powered by an AGN and IR-bright LINERs which have an additional source of power. According to their analysis, the MIR SEDs of AGN powered LINERs are much bluer than the ones of IR-bright LINERs. Furthermore, the PAH flux ratios significantly differ. Interestingly, when looking at fig. 5.30, the VISIR photometry of NGC 4579 and NGC 7213, in both cases, shows a much bluer SED than the *Spitzer* IRS spectra. This could mean that with VISIR we see an AGN dominated LINER while *Spitzer* observes a contaminated object. The interpretation of the IRS spectra being contaminated would, however, require the absolute flux calibration of the spectrum of NGC 7213 to be wrong. This is not likely but possible as the mis-pointing in the case of NGC 4507 shows.

Even in LINERs that do contain AGN, Flohic et al. (2006) find that the ionising luminosities of these AGN, in many cases, are not sufficient to power the observed optical emission lines. They suggest that the line emission is either powered by radiation from hot stars or by a mechanical interaction with the AGN. The latter possibility, in turn, would agree nicely with the detailed analysis of NGC 4579 by Contini (2004).

Another LINER that has been extensively studied is NGC 1097. Mason et al. (2006) observed this AGN in the MIR with the Gemini South telescope. Their flux measurement

exceed ours roughly by a factor of 2. This is probably due to the larger photometric aperture (3″) they use. They compare their near- and mid-IR photometry to calculations based on the clumpy torus model by Nenkova et al. (2002) and come to the conclusion that the AGN is too weak to have a torus that could account for the observed IR emission. Please note that this result would still hold if our photometry was used. Mason et al. (2006) interpret the excess emission as originating in a starburst. Interestingly, they do not detect the $3.3\,\mu$m PAH feature in the nucleus even though it is detected in the larger aperture of *Spitzer*. This implies that either the UV radiation of the young stars destroys the PAH molecules close to the nucleus or that the MIR continuum in that location is not emitted by dust but by shock heated gas as in NGC 4579.

Our observations support the interpretation that LINERs are a mixed bag of differently powered sources. The most luminous LINER in our sample – NGC 7213 – lies very close to the correlation in fig. 5.32 and has the appearance of a regular Sy galaxy. The two less luminous objects NGC 1097 and NGC 4579, on the other hand, deviate significantly. As discussed above, their location in the $L_{\mathrm{MIR}} - L_{\mathrm{X}}$ diagram are consistent with the deviation caused by contamination. If this contaminating emission is, at least in parts, caused by mechanical interaction with the AGN as indicated by the results of Contini (2004) and Flohic et al. (2006), the AGN in these low luminosity sources may be intrinsically different from the more luminous Seyfert type AGN.

7 Work on related projects

> *Knowledge is indivisible. When people grow wise in one direction, they are sure to make it easier for themselves to grow wise in other directions as well. On the other hand, when they split up knowledge, concentrate on their field, and scorn and ignore other fields, they grow less wise – even in their own field.*

Isaac Asimov: The Roving Mind (1983)

During the three years I have spent working on the mid-IR – hard X-ray correlation in AGN, I got involved in a couple of other projects as well. Those that are of importance in the context of this work will be briefly presented and discussed in this chapter.

7.1 High resolution mid IR spectroscopy of Seyfert 2 nuclei[1]

7.1.1 Context

As has been laid out in section 2.3.1, comparing the results of radiative transfer calculations with observed MIR spectra of AGN is an important test for torus models. The clumpy model of Hönig et al. (2006) proved to be successful in reproducing the IR SED of NGC 1068 (fig. 2.5). Since, however, the model was designed with the spectral appearance of this prototypical Seyfert 2 galaxy in mind, it is important to test it against observations of other AGN, as well.

So far, only for very few AGN groundbased MIR spectroscopy have been published. In section 6.1.1, I discussed the importance of high angular resolution for torus studies. As we aim for a detailed modeling of mid -IR spectra of AGN, we could not rely on archival *Spitzer* spectra. Instead, we decided to observe a small sample of type II AGN using the VISIR instrument at the VLT (see section 3.2).

In order to get information unaffected by effects of the host galaxy, we selected objects that are nearby ($z < 0.01$), have a host galaxy that is seen face-on and are bright in the MIR. With these criteria plus the obvious observability constraint, we ended up with three sources: NGC 2110, ESO 428-G14 and MCG-05-23-016.

---

[1]This section is based on work that will be published in Hönig, Horst, Smette, Beckert, Duschl, Gandhi, & Weigelt (2008).

Table 7.1: Parameters of used settings for N-band spectroscopy. We list covered wavelength range, central wavelength, spectral resolution for an $1''$ slit and the spectral dispersion.

λ range [μm]	λ_c [μm]	resolution	dispersion [pixels/μm]
7.7 – 9.3	8.5	300 – 390	160.02
9.0 – 10.6	9.8	305 – 360	160.05
10.34 – 12.46	11.4	185 – 220	119.94
11.34 – 13.46	12.4	215 – 250	119.96

7.1.2 Observations and data reduction

The observations for this project were carried out during ESO period P78, between Octobre 2006 and March 2007. For the spectroscopic part of the programme, we observed each object with VISIR in four low spectral resolution settings that, put together, cover the whole N-band (see table 7.1). In addition, we performed N-band imaging to flux calibrate the spectra. Moreover, Q-band imaging with VISIR and J, H, K', M' -band imaging with NaCo was obtained. These observations served to reconstruct the whole IR SED as far as it is accessible with ground-based telescopes. Unfortunately, since our programme was one of medium priority, not all of the NaCo observations and the Q-band imaging was carried out by ESO. Furthermore, the observations in one of the spectroscopic settings for NGC 2110 was not executed. Here, I present all obtained N-band data.

The N-band imaging was carried out and reduced in the same way as described in section 4.2. Here, we were able to use the knowledge we had gained during our two VISIR imaging campaigns, both for the preparation of the observations and the data reduction. For the spectroscopy, we used 4 different settings (parameters listed in table 7.1) which, combined, cover the entire N-band. For the reduction, we used the ESO VISIR pipeline as well as IDL routines written by ourselves. The absolute flux of the spectra was then scaled to the N-band photometry.

In order to complement our small sample, we re-reduced archival low spectral resolution VISIR spectra of NGC 1068 that had been recorded during the VISIR Science Verification programme. For this object, no corresponding VISIR photometry was available and, thus, we had to rely on the absolute flux calibration of the spectroscopy.

7.1.3 Results and discussion

The torus simulations for NGC 2110, ESO 428-G14 and MCG-05-23-016 are still underway. Therefore, I have to restrict myself to presenting the results of the observations themselves. The recorded spectra – as well as the archival spectrum of NGC 1068 – are shown in figs. 7.1 to 7.4. For comparison, we have also plotted archival *Spitzer* IRS spectra for NGC 2110 and ESO 428-G14 and the Gemini spectrum of NGC 1068 from Mason et al. (2006). For MCG-05-23-016, no comparison spectrum was available.

In all figures, we have highlighted two strong and variable atmospheric bands. In these

shaded parts of the spectrum, the S/N ratio drops and features seen there are probably not real.

The spectral shapes of NGC 1068, ESO 428-G14 and MCG-05-23-016 are quite similar. In all three objects we see a $9.7\,\mu$m silicate absorption feature of moderate (NGC 1068) or weak strength and a continuum that is rising toward longer wavelength. The continuum shape in NGC 2110 is flatter than that of the other objects. In addition, it does not exhibit the silicate feature. NGC 2110 is also the only object that does not have any emission lines in the MIR. The other three objects show [ArIII], [SIV] and [NeII] lines of differing strengths. Interestingly, none of the objects show emission in the $11.3\,\mu$m PAH line. This is a good indication for the observed spectra to be largely free of contamination from SF regions. The atomic lines likely originate in the NLR of the AGN. Since they are relatively weak, the VISIR spectra are probably good representations of the pure torus spectra of these AGN.

In fig.s 7.2 and 7.3, we have also plotted archival IRS spectra of NGC 2110 and ESO 428-G14, respectively. It is obvious that these spectra look quite different than ours. First of all, the IRS spectra show very strong [SIV], PAH and [NeII] lines – and the PAH line is a good indicator for active star formation. Secondly, the spectral slope also varies. In both cases, the continuum observed with *Spitzer* has a steeper rise toward longer wavelengths than the one measured with VISIR. This means that *Spitzer* sees an additional, cooler dust component that is likely associated with SF regions. In addition, in ESO 428-G14, the IRS spectrum exhibits a slightly stronger silicate feature than the VISIR one. The differences in continuum slope and silicate absorption strength between IRS and VISIR spectra adds to the doubt I put forward in section 6.1.1 whether detailed comparisons between AGN torus models and *Spitzer* spectra of Seyfert galaxies can produce meaningful results.

For the three objects with detected emission lines, we find evidence for the presence of the "Baldwin effect". The Baldwin effect, an anti-correlation between continuum luminosity and emission line equivalent width, was first found for the broad Ly_α and CIV lines in QSOs (Baldwin, 1977). The physical origin of the effect is still unclear but usually it is attributed to a change in the continuum slope with luminosity. According to a theoretical work by Korista et al. (1998), the continuum gets softer as the luminosity increases. This means that, relative to the total continuum power, the number of ionising and effectively exciting photons decreases. In turn, this results in reduced equivalent widths of the broad emission lines.

In the MIR, the Baldwin effect was first observed by Keremedjiev & Hao (2006) in a sample of 68 AGN, observed with the *Spitzer* Space Telescope. Their analysis, however, was obstructed by the low spatial resolution of their data, as they note themselves. In our sample we clearly find the effect for the three sources that show MIR emission lines. In table 7.2, we list the emission line equivalent widths W_λ and $12\,\mu$m continuum luminosities λL_λ of these objects. We then plot the anti-correlation between W_λ and $\log \lambda L_\lambda$ in fig. 7.5. We clearly detect the Baldwin effect in the [ArIII], [SIV] and [NeII] lines. The best fit slope to all emission lines is -0.6. It should be noted that our sample is small. Therefore, the value for the slope is of low statistical significance.

NGC 2110 which is omitted in both table 7.2 and fig. 7.5 has a $12\,\mu$m luminosity of $0.96 \cdot 10^{43}$ erg s^{-1}. Thus, from the $W_\lambda - \lambda L_\lambda$ anti-correlation among the other three objects, we would expect to detect emission lines in the spectrum of NGC 2110. Unfortunately,
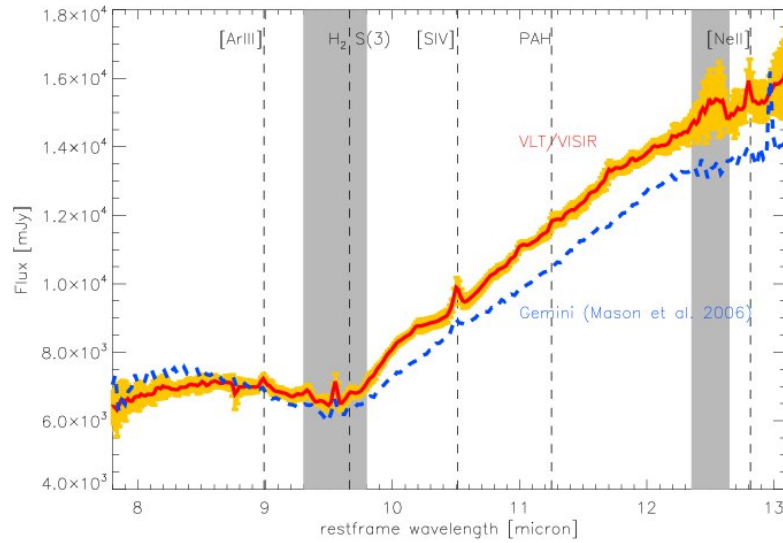
Figure 7.1: N-Band VISIR spectrum of NGC 1068. The red line is the VISIR spectrum, error bars are in yellow. The blue dashed line is a Gemini spectrum (Mason et al., 2006) that we plot for comparison. The grey shaded areas mark regions with strong and variable sky lines. Vertical dashed lines denote the position of common MIR emission lines with names given at the top.
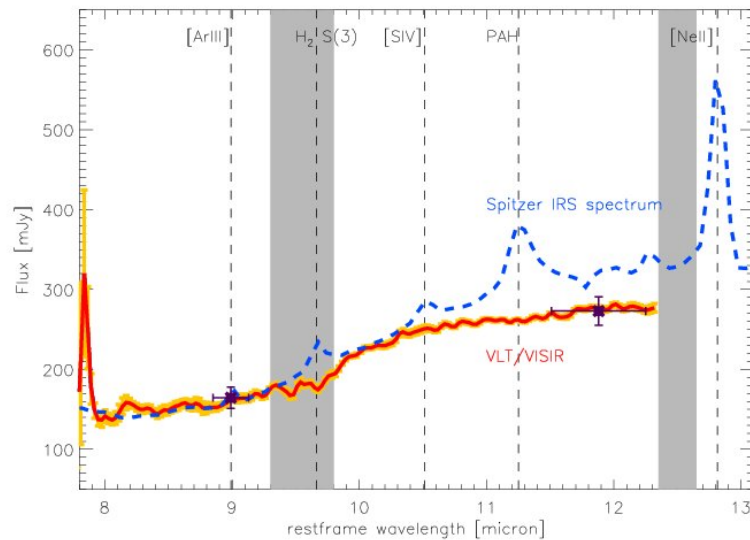
Figure 7.2: N-band VISIR spectrum of NGC 2110. The red line is the VISIR spectrum, error bars are in yellow. Purple crosses mark VISIR photometry that was used for the flux calibration of the spectrum, the horizontal error bars depict the respective filter band width. Here, we compare the VISIR spectrum to an archival *Spitzer* IRS spectrum (blue dashed line). Observations in spectroscopic setting that covers the [NeII] line are missing.
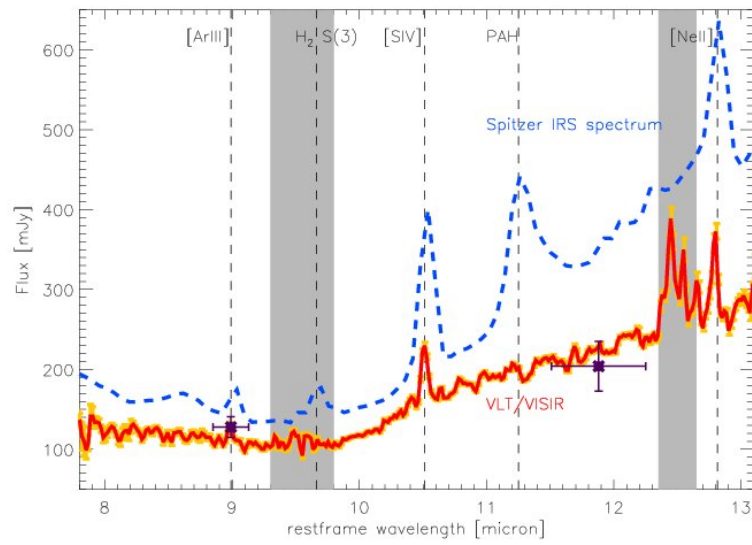
Figure 7.3: N-Band VISIR spectrum of ESO 428-G14. All symbols are as in fig. 7.2.
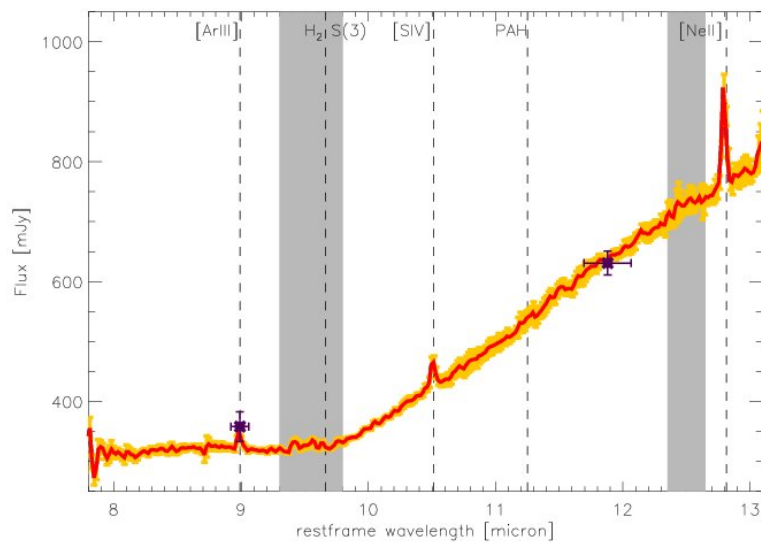
Figure 7.4: N-Band VISIR spectrum of MCG-05-23-016. All symbols are as in fig. 7.1. A comparison spectrum was not available.

Table 7.2: Emission line equivalent widths W_λ for our VISIR sample. In order to illustrate the presence of the Baldwin effect, we also state the $12\,\mu$m continuum luminosities λL_λ. NGC 2110 is omitted in this table since we did not detect any MIR emission lines in this object.

Object	λL_λ [10^{43} erg/2]	W_λ [Ar III] [μm]	W_λ [S IV] [μm]	W_λ [Ne II] [μm]
ESO 428-G14	0.33	0.0095 ± 0.0008	0.0259 ± 0.0014	0.0181 ± 0.0011
NGC 1068	6.81	0.0023 ± 0.0006	0.0034 ± 0.0005	0.0024 ± 0.0003
MCG-05-16-023	2.10	0.0030 ± 0.0003	0.0047 ± 0.0001	0.0098 ± 0.0011

the observation in the spectroscopic setting that covers the [Ne II] line was not executed for this object due to scheduling problems. Thus, we do not know whether the line is emitted in the nucleus or in the more extended region observed by *Spitzer*. The [Ar III] and [S IV] lines, on the other hand, are clearly absent from the spectrum.

The MIR lines we detect are narrow and, thus, likely originate in the NLR. As the NLR can be very extended, the physical origin of broad lines and narrow lines may be quite different (Shields, 2007, and references therein). On the other hand, the high angular resolution of our spectroscopy confines the recorded spectra to those parts of the NLR closest to the central engine. Therefore, it seems reasonable to assume that the excitation of the ions we see in emission is caused by the radiation from the accretion disc. Since the accretion disc also heats the torus, we expect the MIR continuum to scale with the accretion disc emission. The MIR – hard X-ray correlation actually demonstrates that this is, indeed, the case. Therefore, the Baldwin effect in the MIR may be caused by the same mechanism as for the optical broad lines: The ionising continuum softens with luminosity. A problem for this interpretation is the slope. In broad lines, the typical slope for the Baldwin effect is ~ -0.2 instead of -0.6 which we find among our sample. This discrepancy might be caused by the low number statistics of our sample.

We summarise the first results that we draw from this spectroscopic campaign: The nuclear spectra of type II AGN probably show less variation than expected from the analysis of *Spitzer* spectra of lower angular resolution. The strength of the $9.7\,\mu$m silicate feature as well as the slope of the continuum vary among the objects in our sample; the overall shape of the MIR SED, however, is rather similar. Weak [Ar III], [Ne II] and [S IV] lines are found in three of four observed objects. They probably originate in the NLR and show a significant Baldwin effect. The presence of the Baldwin effect in the MIR indicates a close physical connection between accretion disc and torus. Taking into account the main result of this thesis – the MIR – hard X-ray correlation – it seems natural that MIR emission lines show a similar Baldwin effect as broad lines.
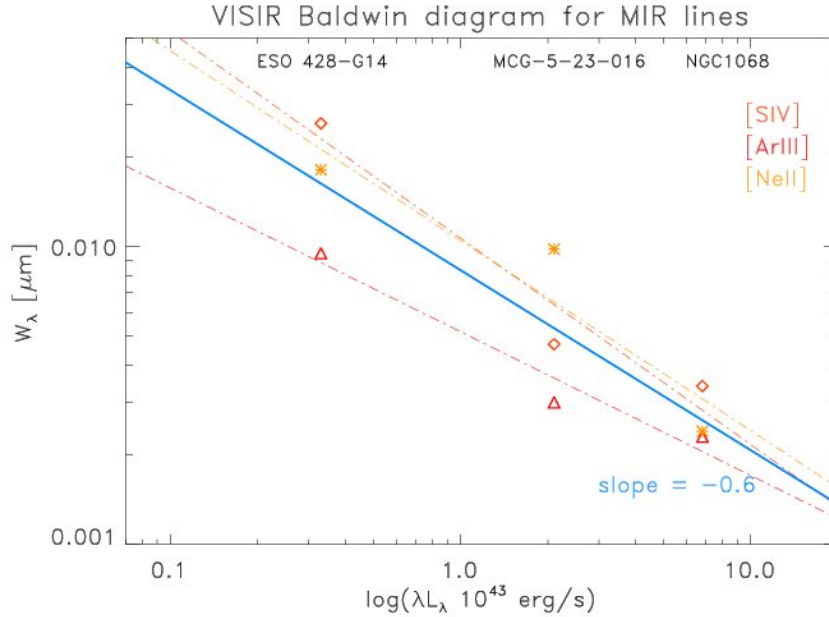
Figure 7.5: Emission line equivalent widths W_λ *vs.* MIR luminosity $\log \lambda L_\lambda$. Triangles denote [ArIII], diamonds denote [SIV] and stars denote [NeII]. The dashed-dotted lines are the the best-fit linear fits to the data. The solid blue line is the best linear fit to all emission lines.

7.2 Nuclear dust emission and the Seyfert 2 dichotomy[2]

7.2.1 Context

The cornerstone evidence for the unified scenario for type I and type II AGN is the existence of broad lines in the polarised spectrum of many Sy 2 objects. So far, about half of the Sy 2s show such evidence for a hidden broad line region (HBLR) and half of them do not (e.g. compilation by Gu & Huang, 2002; Moran, 2007). Such a dichotomy between HBLR and non-HBLR Sy 2s could either (1) result from the existence of real Sy 2s without intrinsic BLR or (2) be due to an observational bias. In order to establish the origin of the Seyfert 2 dichotomy, numerous studies have been performed, but with controversial results.

Theoretical studies suggests that there are limits to the existence of a BLR, in particular at low AGN luminosities (Nicastro, 2000; Nicastro et al., 2003). At the extreme end of the Sy 1 population, some sources show rather narrow H_β lines (FWHM < 2000 km/s). For these narrow line Seyfert 1 galaxies (NLS1s), a few type II counterparts have been found (e.g. by Nagar et al., 2002; Dewangan & Griffiths, 2005; Zhang & Wang, 2006). Since NLS1s constitute less than 15% of the optically selected Sy 1 population, some but not all of the non-HBLR Sy 2s may be misoriented NLS1s.

---

[2]This section is based on work published in Haas, Siebenmorgen, Pantin, Horst, Smette, Käufl, Lagage, & Chini (2007).

Arguments for an origin of the Seyfert-2 dichotomy as an observational bias are numerous. There is no doubt that dust lanes may obscure not only the nucleus but also the scattering mirror necessary for the detection of a HBLR. Hence, only under favorable circumstances one may expect detectable scattered light at all from a hidden AGN (Miller & Goodrich, 1990; Heisler et al., 1997; Gu et al., 2001). And, although still half of the most nearby Sy 2s resist HBLR detection even with Keck spectropolarimetry, such sensitive observations are revealing broad lines in sources which were previously classified as non-HBLRs using smaller telescopes. This reminds us to take care when interpreting spectropolarimetric non-detections of broad lines (Moran, 2007).

With his Lick-Palomar spectropolarimetric survey of the CfA and $12\,\mu$m Seyfert samples Tran (2001, 2003) found that, compared to HBLRs, the non-HBLRs show lower [OIII] luminosities, lower [OIII]/ H$_\beta$ excitation ratios and cooler IRAS $25\,\mu$m / $60\,\mu$m colours with $F_{25}/F_{60} < 0.25$. Most Seyfert galaxies exhibit warm F_{25}/F_{60}, but some have cool colours. Guided by the widespread belief that cool F_{25}/F_{60} indicates a lack of adequate nuclear dust emission, Tran naturally concluded that most if not all non-HBLRs are pure Sy 2s and not misaligned Sy 1s. The host galaxies, however, have a size of about $1'$ so that nuclei and hosts are not separated by the IRAS beam. Hence, nuclear optical properties were compared with extended infrared ones possibly dominated by the host so that the conclusions about the missing nuclear dust torus in non-HBLRs should be checked using adequate nuclear data.

Here, we combine new nuclear MIR $11.25\,\mu$m observations from VISIR at the VLT with published nuclear $10 - 12\,\mu$m photometry of several Seyfert type samples, and compare them with [OIII] literature data as reference quantity. The [OIII] emission arises from the moderately extended narrow-line region (NLR) and we assume that the [OIII] emission can be regarded with little reservation as an isotropic measure of the intrinsic AGN power so that it can be used for suitable normalisation. As has been mentioned earlier, this method has some specific problems. Using the 2-10 keV luminosity instead would have been preferable. Unfortunately, X-ray data of sufficient quality was not available for a large portion of the sample. We find, however that the main result of our study (see below) is robust against extinction correction of the measured [OIII] flux. This implies that we are not affected by a systematic mis-determination of the Balmer decrement due to aperture effects.

The aim here is to check whether there exist naked, i.e. dust free, nuclei among Seyfert galaxies, and in particular among non-HBLRs. As the IR emitting dust would be missing, we expect that the $L_{\mathrm{MIR}}/L_{[\mathrm{OIII}]}$ ratio of a naked nucleus lies below the distribution of that ratio found in most Sy 1s or HBLR Sy 2s. If we would find such objects among non-HBLRs, this would be evidence for them to not host a BLR.

7.2.2 Sample selection and database

For this project, we combined VISIR observations from the Science Verification Program which was conducted between Oct. 2004 and Feb. 2005 with data from a program led by R. Siebenmorgen and our observations on the mid IR – hard X-ray correlation. Since the samples of Siebenmorgen et al. and Horst et al. had been selected with different aims in mind, some of the observed objects are not suitable for the present goal. Therefore, we supplement the VISIR sample with literature data. So far, no data base

Table 7.3: Sample parameters for the Sy 2 dichotomy study. For the stated mean fluxes and luminosities, 3σ upper limits were treated as detections

	Sy 1[a]		Sy 2[b]	HBLR	non-HBLR
Total number of sources	34	(4)	17	29	20
thereof used	17	(2)	12	21	16
mean $\log L_{\text{[OIII]}}$ [erg/s]	40.76		39.73	40.78	40.37
Nuclear $\log L_{12\,\mu\text{m}}$ [$L_\odot$]	9.34		8.22	9.41	8.81
$\log L_{\text{FIR}}$ [$L_\odot$][c]	9.93		9.96	10.25	10.29
Nuclear $F_{12\,\mu\text{m}}$ / $F_{\text{[OIII]}}$ [Jy / erg/s/cm^2]	11.94		11.84	11.99	11.78
Nucl./Gal. $F_{12\,\mu\text{m}}$[d]	0.32		0.08	0.29	0.13

[a] number of NLS1s listed in brackets
[b] without spectropolarimetry
[c] L_{FIR} = luminosity at $60\,\mu\text{m}$ & $100\,\mu\text{m}$
[d] only cool sources with F_{25} / $F_{60} < 0.25$

with homogeneously observed spectropolarimetry and high-resolution MIR photometry exists for a well-defined complete Seyfert sample.

We selected our sample by starting with all Sy 2 sources having spectropolarimetric information (Heisler et al., 1997; Lumsden et al., 2001, 2004; Moran et al., 2000, 2001; Moran, 2007; Tran, 2003). These were mostly drawn from the local ($cz < 3100$ km/s, Ulvestad & Wilson, 1984), the CfA (Huchra & Burg, 1992) and the $12\,\mu\text{m}$ (Rush et al., 1993) Seyfert samples. We included all Sy 1 galaxies from these samples as well as the remaining Sy 2s without spectropolarimetry in order to compare them with HBLRs and non-HBLRs.

We cross-correlated this optical data-base with high-resolution (FWHM $\lesssim 1''$) imaging observations at $10-12\,\mu\text{m}$ (Gorjian et al., 2004; Siebenmorgen et al., 2004; Galliano et al., 2005), as well as $10\,\mu\text{m}$ photometer measurements with $\sim 5''$ aperture (Maiolino et al., 1995, and references therein). We did not scale the MIR fluxes to a common wavelength, since such corrections would be small and rely on assumptions about the spectral slope of the observed objects. As we have seen in section 5.1, dust-enshrouded starbursts may contribute to the nuclear MIR emission. Furthermore, we have discussed in section 5.3.1 that for a $5''$ aperture, such contamination can be significant. Nevertheless, compared to the resolution of $1'$ IRAS had at $12\,\mu\text{m}$, the present study is a major improvement. Therefore, our analysis should be much less affected by contamination than the one by Tran.

We complemented and interpolated missing IRAS $12-100\,\mu\text{m}$ photometry – as far as available – by ISO and *Spitzer* photometry. We excluded sources without data in the far-IR (i.e. lying in sky areas not scanned/observed by IRAS/ISO/*Spitzer*), sources with LINER spectra, and double nuclei with unknown location of the MIR data. This results in 34 Sy 1s (Sy types 1.0 – 1.5) and 66 Sy 2s (types 1.8 – 2.0), 29 with and 20 without detected hidden broad lines and 17 without spectropolarimetry. Table 7.3 lists the sample parameters; for details on the individual objects, consult Haas et al. (2007).

7.2.3 Results and discussion

Figure 7.6 shows the nuclear $12\,\mu$m flux normalised by the corresponding [OIII] flux plotted against the IRAS $25\,\mu$m / $60\,\mu$m colours. All along the range of IRAS colours the bulk of Sy sources lies in the same $F_{12\,\mu m}/F_{[OIII]}$ range. This is also the case for the different Sy types. We note that the few narrow-line Sy 1s of our sample fall in the same range covered by Sy 1s. Three sources – Cen A, Circinus and MCG-06-30-015 – show exceptionally high $F_{MIR}/F_{[OIII]}$ ratios. These objects are suspected to harbour strong dust-enshrouded starbursts close to the nucleus and we decided to exclude them from the present analysis[1]. It is important to note that this decision does not affect our conclusions.

The statistics for the $F_{MIR}/F_{[OIII]}$ distributions are listed in table 7.3. We do not find statistically significant evidence that any of the Seyfert types shows a differing $F_{MIR}/F_{[OIII]}$ distribution. In fig. 7.6 the dotted horizontal lines illustrate the $3\,\sigma$ range around the mean flux ratio for HBLRs. Only one source (NGC 7682) lies slightly below this $3\,\sigma$ range. Remarkably it is a HBLR indicating that the unified model is compatible with rather low $F_{MIR}/F_{[OIII]}$ values and that naked AGN may have to be looked for at $F_{MIR}/F_{[OIII]} \ll 10^{11}$ Jy / erg/s/cm^2. NGC 5427, for which we used the $12\,\mu$m upper flux limit of 10 mJy inferred from *Spitzer*, shows relatively little nuclear dust emission. But even when taking the VISIR upper limit of 2.3 mJy, the evidence for NGC 5427 being a naked Sy 2 is still marginal. To our knowledge this source has not yet been observed by spectropolarimetry. For comparison and to get an impression where a naked Sy might be located in fig. 7.6, we have indicated the position of M 87 whose MIR flux is dominated by jet emission.

While the statistical root mean square (rms) of the MIR and [OIII] measurements is of the order of 10-30%, we here adopted a factor 3 as uncertainty for $F_{MIR}/F_{[OIII]}$ in order to also account for systematic effects. For example, we used the [OIII] fluxes as observed and neither extinction nor aperture corrected since such corrections are uncertain and depend on assumptions on source geometry. Nevertheless, we have performed several tests to correct for extinction in the [OIII] fluxes on the basis of the H_α / H_β ratio. With and without extinction correction the studied distributions are quite broad and do not reveal any reliable trends which would be different from those we see in fig. 7.6. One reason for the apparent "failure" of [OIII] extinction corrections using H_α / H_β ratios may be that the published fluxes refer to observed values. With respect to [OIII] flux losses due to small slit widths, we did not find any trends of $F_{MIR}/F_{[OIII]}$ with distance. This suggests that aperture effects are similar for all sources and largely cancel out in the flux ratios. We also find the nuclear dust emission to be independent of the IRAS $25\,\mu$m / $60\,\mu$m colour of the host galaxy.

In order to understand the Seyfert 2 dichotomy we try to disentangle the AGN and host contributions to the IR spectral SEDs and to explore the origin of the cool IRAS $25\,\mu$m / $60\,\mu$m colours. Therefore, we here consider the nuclear MIR flux concentration and show it in fig. 7.7, plotted over the IRAS $25\,\mu$m / $60\,\mu$m colour. The main features of this plot are (1) that sources with warm F_{25}/F_{60} also have high MIR concentration

---

[1] Actually, I would have preferred to keep these objects for the statistical analysis. After all, both Cen A and MCG-06-30-015 do not deviate from the MIR – hard X-ray correlation in fig. 5.32. This indicates that the MIR fluxes of these objects are not contaminated by SF regions.
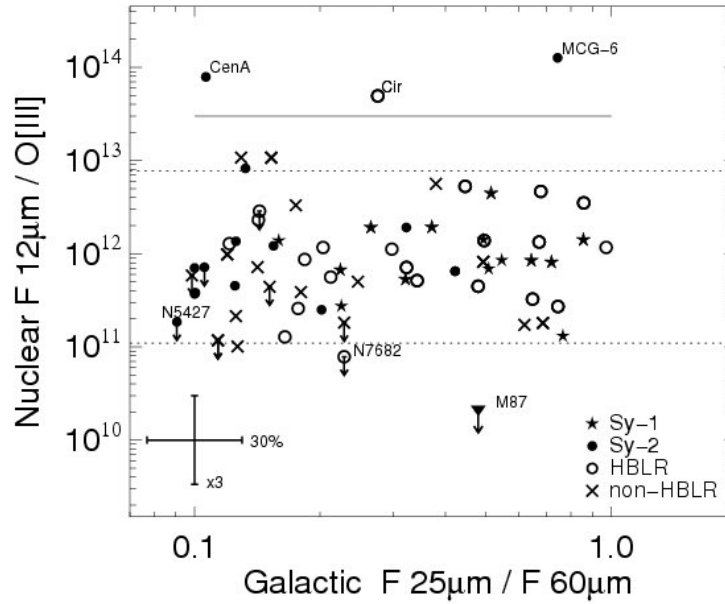
Figure 7.6: Nuclear $12\,\mu$m flux normalised by $F_{\mathrm{[OIII]}}$ versus IRAS $F_{25\,\mu\mathrm{m}}/F_{60\,\mu\mathrm{m}}$. $F_{12\,\mu\mathrm{m}}/F_{\mathrm{[OIII]}}$ is in units Jy / 10^{-16} erg/s/cm^2. Symbols with arrows denote $3\,\sigma$ upper limits. The dotted horizontal lines mark the $3\,\sigma$ range around the mean flux ratio for HBLRs. The solid horizontal line (at y $= 3 \cdot 10^{13}$) marks the transition to sources with the highest MIR / [OIII] ratio. These are suspected to be contaminated by strong dust enshrouded starbursts and excluded from the present analysis.

($>$20%) and (2) that sources with low MIR concentration have cool F_{25}/F_{60} and fall into the lower left corner of fig. 7.7. These two populations can be understood in a simple scheme: (1) a powerful AGN dominates the MIR emission of the host galaxy and causes warm F_{25}/F_{60} if it can also heat a substantial amount of dust in the host galaxy. (2) A nucleus which is faint relative to the cool host, has both a low MIR concentration and a cool F_{25}/F_{60} ratio.

If we now look at the distribution of different Sy types in fig. 7.7, we find the following: All Sy 1s and virtually all (18/20) HBLR Sy 2s emit more than 20% of their total MIR flux in the nucleus. The non-HBLR Sy 2s tend to have both cooler F_{25}/F_{60} and less concentration of MIR flux, reaching down to about 1%. The Sy 2s not yet observed by spectropolarimetry are spread over the entire range of HBLRs and non-HBLRs. While it is known that warm Seyferts exhibit a higher nuclear flux concentration than cool Seyferts (e.g. Roche et al., 1991), our diagram also shows the overall difference in the distribution of HBLRs and non-HBLRs: The latter either have a low AGN / host contrast or cool F_{25}/F_{60}. This indicates that these objects host AGN that are either intrinsically weak or obscured by cold dust within the host galaxy.

To summarise, we do not find any significant difference in the nuclear $F_{12\,\mu\mathrm{m}}/F_{\mathrm{[OIII]}}$ ratio between different Sy types. If non-HBLR Sy 2s were naked AGN, we would expect

Figure 7.7: Nuclear MIR flux concentration versus IRAS $25\,\mu$m / $60\,\mu$m colours. Symbols with arrows denote $3\,\sigma$ upper limits. The vertical dotted line marks the separation between cool and warm sources.
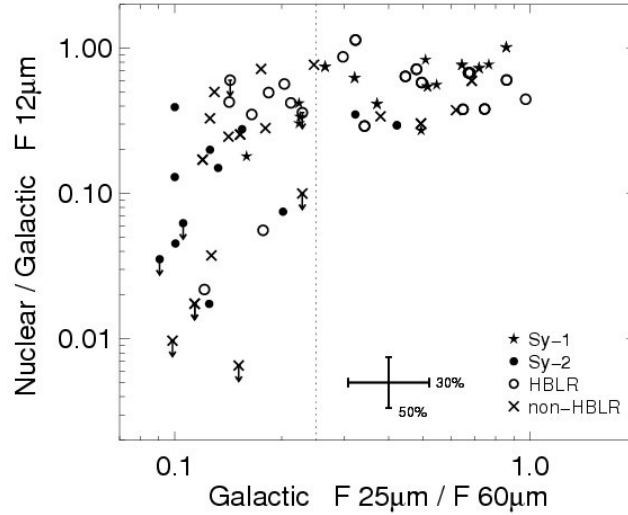
them to have less dust than regular Seyferts and, therefore, exhibit a lower $F_{\mathrm{MIR}}/F_{\mathrm{[OIII]}}$. There is no indication at all, for this effect. Instead, we find that non-HBLRs are preferentially intrinsically weak or obscured by cold dust within the host galaxy. Both effects impose a strong bias against the detection of hidden broad lines. This means that it is very likely that the Seyfert 2 dichotomy is mainly due to observational difficulties and not due to a fundamental physical difference between HBLRs and non-HBLRs.

8 Conclusions and outlook

Es ist entschieden, nun ist's gut – und schnell
Bin ich geheilt von allen Zweifelsqualen,
Die Brust ist wieder frei, der Geist ist hell:
Nacht muß es sein, wo Friedlands Sterne strahlen.
Mit zögerndem Entschluß, mit wankendem Gemüt
Zog ich das Schwert, ich tat's mit Widerstreben,
Da es in meine Wahl noch war gegeben!
Notwendigkeit ist da, der Zweifel flieht,
Jetzt fecht ich für mein Haupt und für mein Leben.

Friedrich Schiller: Wallensteins Tod (1799)

In the following I will summarise the results of our work. Afterwards I will draw the picture of AGN unification and tori as it has been emerging during the last few years. Finally, as there is always one more step to go in research, I will give a brief outlook on present and future projects I am involved in.

8.1 A summary of our results

The red line of this work has undoubtly been "angular resolution" and its impact on IR studies of AGN. As we have seen in sections 5.3.1 and 6.1.1, angular resolution is indeed crucial if we wish to constrain the properties of the dust torus in AGN. Contamination by extra-nuclear IR emission is a serious problem that seems to be underestimated by many authors. In our sample of Seyfert galaxies, we found that SF can contribute up to $\sim 50\%$ of the MIR flux in the innermost $3''$ (and these are not ULIRGs!). We have also seen that spectral appearance can depend significantly on angular resolution. In particular, modeling of the $9.7\,\mu$m silicate feature requires high resolution data to be compared to. This problem is also highlighted by the VISIR spectroscopy presented in section 7.1. The work laid out in 7.2 presents another example of how poorly resolved IR data can lead to incorrect conclusions when applied to the nuclear properties of AGN.

Therefore, in this work, we have examined the correlation between MIR and hard X-ray luminosities by using high resolution VISIR images of local ($z < 0.1$) AGN and archival hard X-ray data. We find a strong and highly significant correlation between the rest frame $12.3\,\mu$m and absorption corrected 2-10 keV luminosities with $\log L_{\mathrm{MIR}} = (-1.61 \mp 1.85) + (1.04 \pm 0.04)\log L_{\mathrm{X}}$. We have performed statistical tests to ensure that the correlation is not caused by a redshift bias in our sample and can reject this possibility with 99 % confidence (see section 5.3.3). Furthermore, we have carefully

examined possible effects of contamination on our results and found the correlation to be robust against excluding possibly contaminated objects. We are, thus, very confident that sources situated close to the best-fit correlation in fig. 5.32 are largely free of contamination. In fact, proximity to the correlation might even serve as an indicator for a low level of IR contamination.

We have also looked for a possible dependence of the $L_{\mathrm{MIR}}/L_{\mathrm{X}}$ ratio on Seyfert type or absorbing column and found neither. With a probability of 97%, the type I and type II sources in our sample have the same mean mid-infrared to hard X-ray luminosity ratio. No evidence was found for a correlation of $L_{\mathrm{MIR}}/L_{\mathrm{X}}$ with N_{H}.

At the low luminosity end of the Seyfert population ($L_{\mathrm{X}} < 10^{42}$ erg s^{-1}), we find a weak tendency for higher $L_{\mathrm{MIR}}/L_{\mathrm{X}}$ ratios compared to the more luminous objects. This deviation, however, is not significant and may simply be caused by contamination of our IR flux measurements.

We interpret these findings in the following way:

- The intrinsic scatter of the mid-IR – hard X-ray correlation is low. Large deviations are primarily caused by contaminating, extra-nuclear IR emission. This agrees well with the prediction that a dust torus exists in every Seyfert galaxy.

- The torus consists of discrete clumps of gas and dust. The volume filling factor of these clumps within the torus is low and the torus appears as optically thin in the mid-IR, in agreement with the theoretical results by Hönig et al. (2006).

- The covering factor f_C of the torus does not depend on AGN luminosity, at least within the luminosity range probed by our study ($10^{40.5}$ erg s$^{-1} \lesssim L_{\mathrm{X}} \lesssim 10^{44.5}$ erg s^{-1}). This also implies the opening angle θ of the torus to be constant with luminosity. This contradicts the prediction of the receding torus model (e.g. Simpson, 2005) and implies that the flaring parameter $\alpha \approx 1$.

- In order to reconcile this with the dependence of the type I fraction f_1 found in X-ray surveys, we suggest the existence of a significant population of Compton-thick AGN at moderate luminosities. The same suggestion has emerged from recent X-ray surveys (e.g. Hasinger et al., 2007), X-ray background synthesis (e.g. Gilli et al., 2007; Gandhi et al., 2007) and IR surveys (Martínez-Sansigre et al., 2005).

- With the present dataset, we are not able to test the predictions by Elitzur & Shlosman (2006) and Hönig & Beckert (2007) that dust tori do not exits in AGN with bolometric luminosities below $L_{\mathrm{low}} \approx 5 \cdot 10^{42}$ erg s^{-1}. We see some indication for a different behavior at low luminosities, but no compelling evidence. The results on NGC 4579 by Contini (2004) and other LINERs by Flohic et al. (2006) suggest that outflows may play an energetically significant role in these low luminosity objects.

In our VISIR spectroscopy campaign (section 7.1), we have found the Baldwin effect for MIR emission lines. Taking into account the MIR – hard X-ray correlation, we can interpret this as an indication that the narrow lines in the MIR are excited by the same radiation field as the broad lines. Furthermore, the presence of the Baldwin effect in the MIR underlines the close physical connection between torus and accretion disc.

In the project described in section 7.2, we have used high resolution MIR imaging and photometry data to reassess the question whether non-HBLR Sy 2 nuclei are intrinsically different than Sy 1 and HBLR Sy 2 objects. We found non-HBLR Sy 2 AGN to have the same ratio of MIR luminosity to nuclear optical emission as all other Sy types. This is a strong argument for these objects to also host the same amount of dust. This, in turn, means that non-HBLR Sy 2s are likely normal Sy nuclei that are either intrinsically weak or suffer from an unfavorable obscuring geometry that prevents us from detecting broad lines in the polarised spectrum. Moreover, we found non-HBLR objects to reside in host galaxies with cool IRAS colors and have a low nucleus / host contrast in the IR. This is further supporting that HBLR and non-HBLR Sy 2s are separated by an observational bias rather than different physics governing the emission processes.

8.2 The emerging picture

All of our results indicate that the unified scenario for AGN works very well. There still remains some doubt concerning the behavior of low luminosity AGN, but for objects with hard X-ray luminosities of $L_{\rm X} \gtrsim 10^{42}$ erg s^{-1}, the picture of an accretion disc and a BLR being surrounded by an obscuring torus seems to hold. Information on the detailed properties of this torus is still sparse but slowly building up.

For the three very nearby and bright AGN NGC 1068, Circinus and Cen A, detailed interferometric observations have been undertaken. In the case of NGC 1068, speckle (at the SAO 6m telescope, Weigelt et al., 2004) and long baseline (with VLTI/MIDI, Jaffe et al., 2004; Wittkowski et al., 2004) interferometry resolve an elongated, compact MIR emitter with a size of roughly 1.5×3.0 pc. This matches the expectations from eq. 2.3 and compact torus models i.e. by Beckert & Duschl (2004); Hönig et al. (2006). For Circinus, using MIDI, Tristram et al. (2007) find a warm IR emitter of 0.4 pc size and a cooler component with $r = 2$ pc and identify these as different parts of the torus. Again, the size of the source matches expectations. Further evidence along these lines comes from SINFONI integral field spectroscopy of NGC 3227 (Davies et al., 2006) where an ordered velocity field of molecular gas is found on the scales expected for the obscuring torus.

In case of Cen A, Meisenheimer et al. (2007) find no evidence for a extended source in the MIR and attribute the emission to the base of the jet instead. While this would mean that Cen A would be a "naked" Seyfert 2 (which may, however, be absorbed by the prominent dust lane in front of the nucleus), the are some doubts regarding the validity of Meisenheimer et al.'s interpretation. Cen A is a weak AGN and, therefore, the torus may be too small to be resolved with the MIDI observation used. Meisenheimer et al. (2007) state a resolution of < 10 milli arcseconds (mas) while from eq. 2.3, we expect $r_{\rm sub}$ to be equivalent to $\lesssim 1$ mas. Meisenheimer et al. plan to observe Cen A with MIDI again and shed some light on this issue.

Recently, Ballantyne et al. (2006) compared radiative transfer calculations for the obscuring tori of AGN with observations and came to the conclusion that the obscuring medium has a typical distance of $r \approx 10$ pc which is a surprisingly high value when compared to compact torus models. Ballantyne et al. (2006), however, did not account for clumpiness of the medium and, thus, neglect self-shielding within the torus which can

lead to cool dust residing in its inner parts. This effect was also found observationally by Tristram et al. (2007). Therefore, the emitting radii of AGN tori may very well be of the order of $\lesssim$ a few parsecs.

Evidence for the torus to be clumpy is building up. Several examples have already been presented in section 2.3. Further support comes from our own work as well as the result by Buchanan et al. (2006). In detailed studies of individual AGN, Tristram et al. (2007) and Mueller Sánchez et al. (2006) find evidence for clumpiness in Circinus and Davies et al. (2006) in NGC 3227. If the torus is clumpy, it is natural to assume a close physical connection to the BLR which is also assumed to be clumpy. In fact, torus and BLR may simply be the cooler and hotter parts, respectively, of the same medium. Evidence for this comes from IR reverberation measurements by Suganuma et al. (2006). They find the measured IR radii to be upper bounds to the measured broad line radii. Furthermore, they find the sizes of broad line regions to scale as $L^{1/2}$ – exactly as expected for the dust sublimation radius.

The likely physical connection of BLR and torus raises an interesting question: What is the size distribution of clumps in the torus? Current model calculations (Nenkova et al., 2002; Dullemond & van Bemmel, 2005; Hönig et al., 2006) assume the clumps to be large and have a well defined surface but this is not what we find in the BLR. Several attempts have been made to detect the kinematical signature of clumpiness as little wiggles in the line profile of broad AGN emission lines (e.g. Arav et al., 1998; Dietrich et al., 1999; Laor et al., 2006) but without any positive result. This has given support to models of fractal cloud distributions such as the one by Bottorff & Ferland (2001). It will be important to test if the same is true for the torus or whether we find the large clouds predicted by most models. In the next section, I will briefly present our own efforts to tackle this question.

Since dusty tori are probably the interface between AGN and the nuclear regions of their respective host galaxies, they are expected to vary in appearance, depending on their environment. Indirect evidence for this is given by the finding that the type II fraction depends on redshift (e.g. Treister & Urry, 2006; Ballantyne et al., 2006). The close correlation we find for L_{MIR} and L_{X}, however, indicates that at least for the local ($z < 0.1$) AGN population, the nuclear geometry is quite similar for most AGN. Peculiarities of individual objects are probably often due to absorption and/or emission in the circumnuclear region.

The evolution of the type II fraction with redshift is likely caused by an evolution of the dust content in the host galaxies. In a recent study of type II QSOs, Polletta et al. (2007) found roughly half of the observed sources to be obscured by dust in the host galaxy rather than the torus. Such obscuration by the host galaxy could explain the results of Treister & Urry (2006) and Ballantyne et al. (2006). This would also be in qualitative agreement with the fact that star formation (in cold, dusty clouds) is closely linked to BH growth in QSOs (Merloni et al., 2004).

Despite all these new results, of course many questions remain open. Many of them concern unification across accretion rate and cosmic time. And as explained above, we still don't know whether low luminosity LINERs consist of the same building blocks as regular Seyferts.

For objects of moderate to high luminosity, we can state that the unified scenario for AGN has been remarkably successful in recent years. Current observing methods now

allow us to imply the physical properties of the obscuring material. Some results are already available and start to form a more or less coherent picture.

8.3 Outlook on present and future projects

Despite all the effort my Ph.D. advisors, my collaborators and I put into the research presented here, it is but a small step in the understanding of AGN tori. Therefore, some of the next steps are already being taken, others are being planned. In the following, I give a brief description of current and future activities.

In order to extend our research of the mid-IR – hard X-ray correlation to Compton-thick sources, we have started another VISIR imaging campaign – this time on highly obscured AGN with inferred hard X-ray luminosities. This has been made possible thanks to observations at very high energies with INTEGRAL, *Swift* and *Suzaku*. For the current interpretation of our results, it will be an important test whether these results still hold for the most heavily obscured sources. Incidentally, many of the selected AGN also have low luminosities so that the programme may also enable us to determine whether the MIR – hard X-ray correlation persists at low AGN luminosities. The observations for this project are being carried out during the current ESO period (P80) and will be finished in March 2008.

Another programme along similar lines is planned: We wish to observe a few objects from our – by then 3 – VISIR samples with *Suzaku*. For highly obscured sources it can be difficult to infer their intrinsic 2-10 keV luminosities with high precision. These difficulties can be overcome by observing at very high X-ray energies which is possible with *Suzaku*. Furthermore, with respect to the timescales of radiative transfer from the accretion disk to the torus, these observations will be quasi-simultaneously to our VISIR observations which can be advantageous for objects with a significant long-term variability.

Encouraged by the interesting results of our VISIR spectroscopy campaign of local type II AGN (section 7.1), we have started a very similar programme for local type I AGN. We selected three Sy 1 galaxies and will perform low resolution N-band spectroscopy as well as N- and Q-band imaging with VISIR. A detailed modeling of both the type I and the type II samples will follow. These observations are also being carried out during the current ESO period and will be finished during March 2008. For the next two periods we have applied for even more observing time on VISIR. We wish to carry out a large spectroscopic campaign of local Seyfert nuclei. If the observing time is granted we will obtain N-band spectra with high angular resolution for 20 additional AGN. This will enable us to, for the first time, study a statistically significant sample of AGN with high quality MIR spectra available.

While evidence for tori to be clumpy rather than smooth has been building up the question has not been decided, yet. Furthermore, nothing is known about the size distribution of the putative clumps. Therefore, we carried out high angular and spectral resolution spectroscopy of a molecular emission line in NGC 1068 in order to look for the kinematic signature of clumpiness. This experiment is similar to the ones conducted to look for clumpiness in the BLR – as yet without success. For our programme, we observed the $2.122\,\mu$m H_2 1-0S(1) line with CRIRES (Käufl et al., 2004), the high reso-

lution IR spectrometer at the VLT. The observations and the basic data reduction have been finished. Since our goal is a demanding one, the data analysis is difficult so that at the time of writing of this thesis it is still ongoing. As a first result, we can state that we resolve the outer parts of the torus of NGC 1068 and see H_2 line emission on both sides of the nucleus with the line on one side being redshifted with respect to the line on the other side. This appears to be the spectroscopic signature of the rotation of the molecular gas around the SMBH – something that on such small scales has been observed for the first time.

Finally, for another programme that is being executed during the present ESO period, we will observe the nearest type I AGN, NGC 3783 with VLTI/MIDI. Such observations already exist but have produced puzzling results: We do not find evidence for the $9.7\,\mu$m silicate feature and the inferred size of the MIR emission region is much larger than expected for a compact dusty torus. The fact that NGC 3783 perfectly falls onto the mid IR – hard X-ray correlation (see section 5.3.2), on the other hand, indicates that it does have the same kind of torus as other AGN. Therefore, we will observe this object with some additional VLTI baselines and then, hopefully, be able infer the nature of its MIR emission.

We hope that these observations, combined with modeling efforts along the lines of Hönig et al. (2006), will make it possible to constrain the physical state of the torus in more detail than has been possible so far.

Bibliography

References are listed alphabetically, sorted after authors names.

Akylas, A., I. Georgantopoulos, A. Georgakakis, S. Kitsionas & E. Hatziminaoglou (2006). XMM-*Newton* and *Chandra* measurements of the AGN intrinsic absorption: dependence on luminosity and redshift. *Astronomy & Astrophysics 459*, 693–701.

Antonucci, R. R. J. (1982). Optical polarization position angle versus radio source axis in radio galaxies. *Nature 299*, 605–606.

Antonucci, R. R. J. (1984). Optical spectropolarimetry of radio galaxies. *The Astrophysical Journal 278*, 499–520.

Antonucci, R. R. J. (1993). Unified models for active galactic nuclei and quasars. *Annual Review of Astronomy & Astrophysics 31*, 473–521.

Antonucci, R. R. J. & J. S. Miller (1985). Spectropolarimetry and the nature of NGC 1068. *The Astrophysical Journal 297*, 621–632.

Antonucci, R. R. J. & J. S. Ulvestad (1984). Blazars can have double radio sources. *Nature 308*, 617–619.

Arav, N., T. A. Barlow, A. Laor, W. L. W. Sargent & R. D. Blandford (1998). Are AGN broad emission lines formed by discrete clouds? Analysis of Keck high-resolution spectroscopy of NGC 4151. *Monthly Notices of the Royal Astronomical Society 297*, 990–998.

Awaki, H., H. Murakami, Y. Ogawa & K. M. Leighly (2006). Variability Study of Seyfert 2 Galaxies with XMM-*Newton*. *The Astrophysical Journal 645*, 928–939.

Baldwin, J. A. (1977). Luminosity Indicators in the Spectra of Quasi-Stellar Objects. *The Astrophysical Journal 214*, 679–684.

Ballantyne, D. R., Y. Shi, G. H. Rieke, J. L. Donley, C. Papovich & J. R. Rigby (2006). Does the AGN Unified Model Evolve with Redshift? Using the X-ray Background to Predict the Mid-Infrared Emission of AGNs. *The Astrophysical Journal 653*, 1070–1088.

Barnes, J. E. & L. E. Hernquist (1996). Transformations of galaxies. II. Gasdynamics in merging disk galaxies. *The Astrophysical Journal 471*, 115–142.

Barthel, P. D. (1989). Is every quasar beamed? *The Astrophysical Journal 336*, 606–611.

Barvainis, R. (1987). Hot Dust and the Near-Infrared Bump in the Continuum Spectra of Quasars and Active Galactic Nuclei. *The Astrophysical Journal 320*, 537–544.

Bassani, L., M. Dadina, R. Maiolino, M. Salvati, G. Risaliti, R. della Ceca, G. Matt & G. Zamorani (1999). A Three-dimensional Diagnostic Diagram for Seyfert 2 Galaxies: Probing X-Ray Absorption and Compton Thickness. *The Astrophysical Journal Supplement Series 121*, 473–482.

Beckert, T. & W. J. Duschl (2004). The dynamical state of a thick cloudy torus around an AGN. *Astronomy & Astrophysics 426*, 445–454.

Beckert, T., W. J. Duschl & B. Vollmer (2004). Torus models for obscuration in type 2 AGN. In S. N. A. Merloni & R. Sunyaev (Eds.), *Growing Black Holes held in Garching, Germany, June 21-25, 2004*.

Beckmann, V., N. Gehrels & C. R. Shrader (2006). The First *INTEGRAL* AGN Catalog. *The Astrophysical Journal 638*, 642–652.

Begelman, M. C. (2003). AGN Feedback Mechanisms. *astro-ph 0303040*.

Bianchi, S., G. Matt, I. Balestra, M. Guainazzi & G. C. Perola (2004). X-ray reprocessing in Seyfert galaxies: Simultaneous XMM-*Newton*/BeppoSAX observations. *Astronomy & Astrophysics 422*, 65–76.

Blandford, R. D. & A. Konigl (1979). Relativistic jets as compact radio sources. *The Astrophysical Journal 232*, 34–48.

Blandford, R. D. & M. J. Rees (1978). Some comments on radiation mechanisms in Lacertids. In A. M. Wolfe (Ed.), *Pittsburgh Conference on BL Lac Objects, Pittsburgh, Pa., April 24-26, 1978, Proceedings. (A79-30026 11-90) Pittsburgh, Pa., University of Pittsburgh, 1978. NATO-supported research*, pp. 328–341.

Blustin, A. J., G. Branduardi-Raymontand E. Behar, J. S. Kaastra, S. M. Kahn, M. J. Page, M. Sako & K. C. Steenbrugge (2002). Multi-wavelength study of the Seyfert 1 galaxy NGC 3783 with XMM-Newton. *Astronomy & Astrophysics 392*, 453–467.

Bottorff, M. & G. Ferland (2001). Fractal Quasar Clouds. *The Astrophysical Journal 549*, 118–132.

Buchanan, C. L., J. F. Gallimore, C. P. O'Dea, S. A. Baum, D. J. Axon, A. Robinson, M. Elitzur & M. Elvis (2006). *Spitzer* IRS spectra of a Large Sample of Seyfert Galaxies: A Variety of Infrared Spectral Energy Distributions in the Local Active Galactic Nucleus Population. *The Astronomical Journal 132*, 401–419.

Camenzind, M. (1995). Magnetic Fields and the Physics of Active Galactic Nuclei. *Reviews in Modern Astronomy 8*, 201–234.

Cappi, M., F. Panessa, L. Bassani, M. Dadina, G. DiCocco, A. Comastri, R. D. Ceca, A. V. Filippenko, F. Gianotti, L. C. Ho, G. Malaguti, J. S. Mulchaey, G. G. C. Palumbo, E. Piconcelli, W. L. W. Sargent, J. Stephen, M. Trifoglio & K. A. Weaver

(2006). X-ray Spectral Survey with XMM–Newton of a Complete Sample of Nearby Seyfert Galaxies. *Astronomy & Astrophysics 446*, 459–470.

Carr, B. J. (1975). The primordial black hole mass spectrum. *The Astrophysical Journal 201*, 1–19.

Clavel, J., B. Schulz, B. Altieri, P. Barr, P. Claes, A. Heras, K. Leech, L. Metcalfe & A. Salama (2000). 2.5-11 micron spectroscopy and imaging of AGNs. Implication for unification schemes. *Astronomy & Astrophysics 357*, 839–849.

Contini, M. (2004). The complex structure of low-luminosity active galactic nuclei: NGC 4579. *Monthly Notices of the Royal Astronomical Society 454*, 675–683.

Dadina, M. (2007). *Beppo*SAX observations in the 2-100 keV band of the nearby Seyfert galaxies: an atlas of spectra. *Astronomy & Astrophysics 461*, 1209–1252.

Dahari, O. & M. M. De Robertis (1988). A statistical study of properties of Seyfert and starburst galaxies. *The Astrophysical Journal Supplement Series 67*, 249–277.

Davies, R. I., J. Thomas, R. Genzel, F. Mueller Sánchez, L. J. Tacconi, A. Sternberg, F. Eisenhauer, R. Abuter, R. Saglia & R. Bender (2006). The star-forming torus and stellar dynamical black hole mass in the Seyfert 1 nucleus of NGC 3227. *The Astrophysical Journal 646*, 754–773.

Della Ceca, R., S. Pellegrini, L. Bassani, V. Beckmann, M. Cappi, G. G. C. Palumbo, G. Trinchieri & A. Wolter (2001). Unveiling the AGN powering the "Composite" Seyfert/Star-forming galaxy NGC 7679: *Beppo*SAX and ASCA results. *Astronomy & Astrophysics 375*, 781–790.

Dewangan, G. C. & R. E. Griffiths (2005). Type 2 Counterparts of Narrow-Line Seyfert 1 Galaxies. *The Astrophysical Journal 625*, L31–L34.

Dewangan, G. C., R. E. Griffiths, T. Di Matteo & N. J. Schurch (2004). Iron Kα Emission from the Low-Luminosity Active Galaxies M81 and NGC 4579. *The Astrophysical Journal 607*, 788–793.

Dietrich, M., S. J. Wagner, T. J.-L. Courvoisier, H. Bock & P. North (1999). Structure of the broad-line region of 3C 273. *Astronomy & Astrophysics 351*, 31–42.

Draine, B. T. & H. M. Lee (1984). Optical properties of interstellar graphite and silicate grains. *The Astrophysical Journal 285*, 89–108.

Dullemond, C. P. & I. M. van Bemmel (2005). Clumpy tori around active galactic nuclei. *Astronomy & Astrophysics 436*, 47–56.

Duschl, W. J., P. A. Strittmatter & P. L. Biermann (2000). A note on hydrodynamic viscosity and selfgravitation in accretion disks. *Astronomy & Astrophysics 357*, 1123–1132.

Ebisawa, K., G. Bourban, A. Bodaghee, N. Mowlavi & T. J. L. Courvoisier (2003). High-energy sources before INTEGRAL. INTEGRAL reference catalog. *Astronomy & Astrophysics 411*, L59–L62.

Efstathiou, A. & M. Rowan-Robinson (1995). Dusty discs in active galactic nuclei. *Monthly Notices of the Royal Astronomical Society 273*, 649–661.

Elitzur, M. & I. Shlosman (2006). The AGN obscuring torus - end of the "doughnut" paradigm. *The Astrophysical Journal 648*, L101–L104.

Evans, D. A., R. P. Kraft, D. M. Worrall, M. J. Hardcastle, C. Jones, W. R. Forman & S. S. Murray (2004). *Chandra* and XMM-*Newton* Observations of the Nucleus of Centaurus A. *The Astrophysical Journal 612*, 786–796.

Evans, I. N., H. C. Ford, A. L. Kinney, R. R. J. Antonucci, L. Armus & S. Caganoff (1991). HST imaging of the inner 3 arcseconds of NGC 1068 in the light of forbidden O III 5007 A. *The Astrophysical Journal 369*, L27–L30.

Fabian, A. C., S. Vaughan, K. Nandra, K. Iwasawa, D. R. Ballantyne, J. C. Lee, A. De Rosa, A. Turner & A. J. Young (2003). A long hard look at MCG-6-30-15 with XMM-Newton. *Monthly Notices of the Royal Astronomical Society 335*, L1–L5.

Fanaroff, B. L. & J. M. Riley (1974). The morphology of extragalactic radio sources of high and low luminosity. *Monthly Notices of the Royal Astronomcal Society 167*, 31P–36P.

Ferrarese, L. & D. Merritt (2000). A Fundamental Relation between Supermassive Black Holes and Their Host Galaxies. *The Astrophysical Journal 539*, L9–L12.

Filippenko, A. V. & W. L. W. Sargent (1985). A search for "'dwarf"' Seyfert 1 nuclei. I. The initial data and results. *The Astrophysical Journal Supplement Series 57*, 503–522.

Flohic, H. M. L. G., M. Eracleous, G. Chartas, J. C. Shields & E. C. Moran (2006). The Central Engines of 19 LINERs as Viewed by Chandra. *The Astrophysical Journal 647*, 140–160.

Francis, P. J., P. C.Hewett, C. B. Foltz, F. H. Chaffee, R. J. Weymann & S. L. Morris (1991). A high signal-to-noise ratio composite quasar spectrum. *The Astrophysical Journal 373*, 465–470.

Fritz, J., A. Franceschini & E. Hatziminaoglou (2006). Revisiting the infrared spectra of active galactic nuclei with a new torus emission model. *Monthly Notices of the Royal Astronomical Society 366*, 767–786.

Galliano, E. & D. Alloin (2002). Near-IR 2D-spectroscopy of the 4" × 4" region around the Active Galactic Nucleus of NGC 1068 with ISAAC/VLT. *Astronomy & Astrophysics 393*, 43–56.

Galliano, E., D. Aloin, E. Pantin, P.-O. Lagage & O. Marco (2005). Mid-infrared imaging of active galaxies. Active nuclei and embedded star clusters. *Astronomy & Astrophysics 438*, 803–820.

Galliano, E., E. Pantin, D. Alloin & P. O. Lagage (2005). Mid-infrared imaging of NGC1068 with VISIR at the VLT. *Monthly Notices of the Royal Astronomical Society 363*, L1–L5.

Gallo, L. C. (2006). Investigating the nature of narrow-line Seyfert 1 galaxies with high-energy spectral complexity. *Monthly Notices of the Royal Astronomical Society 368*, 479–486.

Gallo, L. C., I. Lehmann, W. Pietsch, T. Boller, W. Brinkmann, P. Friedrich & D. Grupe (2006). *XMM-Newton* observations of bright ROSAT selected active galactic nuclei with low intrinsic absorption. *Monthly Notices of the Royal Astronomical Society 365*, 688–698.

Gandhi, P., A. C. Fabian, T. Suebsuwong, J. Malzac, G. Miniutti & R. J. Wilman (2007). Constraints on light bending and reflection from the hard X-ray background. *Monthly Notices of the Royal Astronomical Society in press, astro-ph 0709.1984,*.

Gebhardt, K., R. Bender, G. Bower, A. Dressler, S. M. Faber, A. V. Filippenko, R. Green, C. Grillmair, L. C. Ho, J. Kormendy, T. R. Lauer, J. Magorrian, J. Pinkney, D. Richstone & S. Tremaine (2000). A Relationship between Nuclear Black Hole Mass and Galaxy Velocity Dispersion. *The Astrophysical Journal 539*, L13–L16.

Georgantopoulos, I. & I. E. Papadakis (2001). RXTE observations of Seyfert 2 galaxies: evidence for spectral variability. *Monthly Notices of the Royal Astronomical Society 322*, 218–230.

Gilli, R., A. Comastri & G. Hasinger (2007). The synthesis of the cosmic X-ray background in the Chandra and XMM-Newton era. *Astronomy & Astrophysics 463*, 79–96.

Gondoin, P., D. Lumb, H. Siddiqui, M. Guainazzi & N. Schartel (2001). XMM-Newton observation of the Seyfert 1 galaxy Fairall 9. *Astronomy & Astrophysics 373*, 805–815.

Gondoin, P., A. Orr & D. Lumb (2003). XMM-*Newton* observations of the Seyfert 1 galaxy ESO 141-G55. *Astronomy & Astrophysics 398*, 967–973.

González-Martín, O., J. Masegosa, I. Márquez, M. A. Guerrero & D. Dultzin-Hacyan (2006). X-ray nature of the LINER nuclear sources. *Astronomy & Astrophysics 460*, 45–57.

Gorjian, V., M. W. Werner, T. H. Jarrett, D. M. Cole & M. E. Ressler (2004). 10 Micron Imaging of Seyfert Galaxies from the 12 Micron Sample. *The Astrophysical Journal 605*, 156–167.

Grandi, P., M. Fiocchi, C. G. Perola, C. M. Urry, L. Maraschi, E. Massaro, G. Matt, A. Preite-Martinez, H. Steinle & W. Collmar (2003). *Beppo*SAX Observations of Centaurus A: The Hard Continuum and the Iron-Line Feature. *The Astrophysical Journal 593*, 160–168.

Grandi, P., M. Guainazzi, M. Cappi & G. Ponti (2007). XMM-*Newton* unveils the type 2 nature of the BLRG 3C 445. *Monthly Notices of the Royal Astronomical Society 381*, L21–L25.

Grogin, N. A., C. J. Conselice, E. Chatzichristou, D. M. Alexander, F. E. Bauer, A. E. Hornschemeier, S. Jogee, A. M. Koekemoer, V. G. Laidler, M. Livio, R. A. Lucas,

M. Paolillo, S. Ravindranath, E. J. Schreier, B. D. Simmons & C. M. Urry (2005). AGN Host Galaxies at z 0.4-1.3: Bulge-dominated and Lacking Merger-AGN Connection. *The Astrophysical Journal 627*, L97–L100.

Gu, Q. & J. Huang (2002). Seyfert 2 Galaxies with Spectropolarimetric Observations. *The Astrophysical Journal 579*, 205–213.

Gu, Q., R. Maiolino & D. Dultzin-Hacyan (2001). Nuclear obscuration and scattering in Seyfert 2 galaxies. *Astronomy & Astrophysics 366*, 765–770.

Guainazzi, M., A. C. Fabian, K. Iwasawa, G. Matt & F. Fiore (2005). On the transmission-dominated to reprocessing-dominated spectral state transitions in Seyfert 2 galaxies. *Monthly Notices of the Royal Astronomical Society 356*, 295–308.

Haas, M., R. Siebenmorgen, E. Pantin, H. Horst, A. Smette, H.-U. Käufl, P.-O. Lagage & R. Chini (2007). VISIR / VLT mid-infrared imaging of Seyfert nuclei : nuclear dust emission and the Seyfert-2 dichotomy. *Astronomy & Astrophysics 473*, 369–376.

Hao, L., H. W. W. Spoon, G. C. Sloan, J. A. Marshal, L. Armus, A. G. G. M. Tielens, B. Sargent, I. M. van Bemmel, V. Charmandaris, D. W. Weedman & J. R. Houck (2005). The detection of silicate emission from quasars at 10 and 18 microns. *The Astrophysical Journal 625*, L75–L78.

Hao, L., D. W. Weedman, H. W. W. Spoon, J. A. Marshall, N. A. Levenson, M. Elitzur & J. R. Houck (2007). The Distribution of Silicate Strength in Spitzer Spectra of AGNs and ULIRGs. *The Astrophysical Journal 655*, L77–L80.

Hasinger, G., N. Cappelluti, H. Brunner, M. Brusa, A. Comastri, M. Elvis, A. Finoguenov, F. Fiore, A. Fraceschini, R. Gilli, R. E. Griffiths, I. Lehmann, V. Mainieri, G. Matt, I. Matute, T. Miyaji, S. M. S. Paltani, D. B. Sanders, N. Scoville, L. Tresse, C. M. Urry, P. Vettolani & G. Zamorani (2007). The XMM-Newton Wide-Field Survey in the COSMOS Field. I. Survey Description. *The Astrophysical Journal Supplement Series 172*, 29–37.

Heckman, T. M., A. Ptak, A. Hornschemeier & G. Kauffmann (2005). The Relationship of Hard X-Ray and Optical Line Emission in Low-Redshift Active Galactic Nuclei. *The Astrophysical Journal 634*, 161–168.

Heisler, C. A., S. L. Lumsden & J. A. Bailey (1997). Visibility of scattered broad-line emission in Seyfert 2 galaxies. *Nature 385*, 700–702.

Ho, L. C., E. D. Feigelson, L. K. Townsley, R. M. Sambruna, G. P. Garmire, W. N. Brandt, A. V. Filippenko, R. E. Griffiths, A. F. Ptak & W. L. W. Sargent (2001). Detection of Nuclear X-Ray Sources in Nearby Galaxies with Chandra. *The Astrophysical Journal 549*, L51–L54.

Hönig, S. & T. Beckert (2007). AGN dust tori at low and high luminosities. *Monthly Notices of the Royal Astronomical Society 380*, 1172–1176.

Hönig, S. F., T. Beckert, K. Ohnaka & G. Weigelt (2006). Radiative Transfer Modeling of Three-Dimensional Clumpy AGN Tori and its Application to NGC 1068. *Astronomy & Astrophyics 452*, 459–471.

Hönig, S. F., T. Beckert, K. Ohnaka & G. Weigelt (2007). 3D Radiative Transfer Modeling of Clumpy Dust Tori around AGN. In L. C. Ho & J.-M. Wang (Eds.), *The Central Engine of Active Galactic Nuclei*, ASP Conference Series, pp. 487–+.

Hönig, S. F., H. Horst, A. Smette, T. Beckert, W. J. Duschl, P. Gandhi & G. Weigelt (2008). The nuclear mid-infrared emission of Sy 2 AGN. *in preparation*.

Hopkins, P. F., L. Hernquist, T. J. Cox, T. D. Matteo, B. Robertson & V. Springel (2006). A unified, merger-driven model for the origin of starbursts, quasars, the cosmic X-ray background, supermassice black holes and galaxy spheroids. *The Astrophysical Journal 163*, 1–49.

Horst, H. & W. J. Duschl (2007). A Simple Model for Quasar Density Evolution. In B. Aschenbach, V. Burwitz, G. Hasinger, & B. Leibundgut (Eds.), *Relativistic Astrophysics and Cosmology - Einstein's Legacy*, ESO Astrophysics Symposia, pp. 224–226.

Horst, H., P. Gandhi, A. Smette & W. J. Duschl (2007). The mid IR – hard X-ray correlation in AGN and ist implications for dusty torus models. *Astronomy & Astrophysics in press, astro-ph 0711.3734*.

Horst, H., A. Smette, P. Gandhi & W. J. Duschl (2006). The small dispersion of the mid IR – hard X-ray correlation in active galactic nuclei. *Astronomy & Astrophysics 457*, L17–L20.

Houck, J. R., T. L. Roellig, J. van Cleve, W. J. Forrest, T. Herter, C. R. Lawrence, K. Matthews, H. J. Reitsema, B. T. Soifer, D. M. Watson, D. Weedman, M. Huisjen, J. Troeltzsch, D. J. Barry, J. Bernard-Salas, C. E. Blacken, B. R. Brandl, V. Charmandaris, D. Devost, G. E. Gull, P. Hall, C. P. Henderson, S. J. U. Higdon, B. E. Pirger, J. Schoenwald, G. C. Sloan, K. I. Uchida, P. N. Appleton, L. Armus, M. J. Burgdorf, S. B. Fajardo-Acosta, C. J. Grillmair, J. G. Ingalls, P. W. Morris & H. I. Teplitz (2004). The Infrared Spectrograph (IRS) on the Spitzer Space Telescope. *The Astrophysical Journal Supplement Series 154*, 18–24.

Huchra, J. & R. Burg (1992). The spatial distribution of active galactic nuclei. I - The density of Seyfert galaxies and liners. *The Astrophysical Journal 393*, 90–97.

Immeli, A., M. Samland, P. Westera & O. Gerhard (2004). Subgalactic Clumps at High Redshift: A Fragmentation Origin? *The Astrophysical Journal 611*, 20–25.

Iyomoto, N., K. Makishima, Y. Fukazawa, M. Tashiro, Y. Ishisaki, N. Nakai & Y. Taniguchi (1996). Detection of Excess Hard X-Ray Emission from the Optical Jet ' Galaxy NGC 1097. *Publications of the Astronomical Society of Japan 48*, 231–236.

Jaffe, W., K. Meisenheimer, H. J. A. Röttgering, C. Leinert, A. Richichi, O. Chesneau, D. Fraix-Burnet, A. Glazenborg-Kluttig, G. L. Granato, U. Graser, B. Heijligers, R. Köhler, F. Malbet, G. K. Miley, F. Paresce, J.-W. Pel, G. Perrin, F. Przygodda,

M. Schoeller, H. Sol, L. B. F. M. Waters, G. Weigelt, J. Woillez & P. T. de Zeeuw (2004). The central dusty torus in the active nucleus of NGC 1068. *Nature 429*, 47–49.

Jiang, P., J. X. Wang & T. G. Wang (2006). On the X-Ray Baldwin Effect for Narrow Fe Kα Emission Lines. *The Astrophysical Journal 644*, 725–732.

Jiménez-Bailón, E., M. Santos-Lleó, J. M. Mas-Hesse, M. Guainazzi, L. Colina, M. C. no & R. M. González Delgado (2003). Nuclear Activity and Massive Star Formation in the Low-Luminosity Active Galactic Nucleus NGC 4303: *Chandra* X-Ray Observations. *The Astrophysical Journal 593*, 127–141.

Kataoka, J., J. R. Mattox, J. Quinn, H. Kubo, F. Makino, T. Takahashi, S. Inoue, R. C. Hartmann, G. M. Madejski, P. Sreekumar & S. J. Wagner (1999). Multiwavelength observations of the TeV blazar Mrk 501 in March 1996. The first report of the detection by EGRET. *Astroparticle Physics 11*, 149–151.

Käufl, H. U., P. Ballester, P. Biereichel, B. Delabre, R. Donaldson, R. Dorn, E. Fedrigo, G. Finger, G. Fischer, F. Franza, D. Gojak, G. Huster, Y. Jung, J.-L. Lizon, L. Mehrgan, M. Meyer, A. Moorwood, J.-F. Pirard, J. Paufique, E. Pozna, R. Siebenmorgen, A. Silber, J. Stegmeier & S. Wegerer (2004). CRIRES: A High Resolution Infrared Spectrograph for ESO's VLT. In A. F. M. Moorwood & M. Iye (Eds.), *Ground-based Instrumentation for Astronomy*, Volume 5492 of *Proceedings of the SPIE*, pp. 1218–1227.

Keel, W. C. (1983). Spectroscopic evidence for activity in the nuclei of normal spiral galaxies. *The Astrophysical Journal 269*, 466–486.

Kennicutt, R. J. (1992). A spectrophotometric atlas of galaxies. *The Astrophysical Journal Supplement Series 79*, 255–284.

Keremedjiev, M. & L. Hao (2006). Characterization of the Balwin Effect for AGN in the Mid Infrared. In *American Astronomical Society Meeting 209*, Volume 38 of *Bulletin of the American Astronomical Society*, pp. 1096–+.

King, A. R. & J. E. Pringle (2007). Fuelling active galactic nuclei. *Monthly Notices of the Royal Astronomical Society 377*, L25–L28.

Kishimoto, M., S. F. Hönig, T. Beckert & G. Weigelt (2007). The innermost region of AGN tori: implications from the HST/NICMOS type 1 point sources and near-IR reverberation. *Astronomy & Astrophysics 476*, 713–721.

Korista, K., J. Baldwin & G. Ferland (1998). Quasars as Cosmological Probes: The Ionizing Continuum, Gas Metallicity, and the W$_\lambda$-L Relation. *The Astrophysical Journal 507*, 24–30.

Krabbe, A., T. Böker & R. Maiolino (2001). N-Band Imaging of Seyfert Nuclei and the Mid-Infrared-X-Ray Correlation. *The Astrophysical Journal 557*, 626–636.

Kraemer, S. B., I. M. George, D. M. Crenshaw & J. R. Gabel (2004). On the Relationship between the Optical Emission-Line and X-Ray Luminosities in Seyfert 1 Galaxies. *The Astrophysical Journal 607*, 794–799.

Kristian, J. (1973). Quasars as Events in the Nuclei of Galaxies: the Evidence from Direct Photographs. *The Astrophysical Journal 179*, L61–L65.

Krolik, J. H. (2007). AGN Obscuring Tori Supported by Infrared Radiation Pressure. *The Astrophysical Journal 661*, 52–59.

Krolik, J. H. & M. C. Begelman (1988). Molecular tori in Seyfert galaxies - Feeding the monster and hiding it. *The Astrophysical Journal 329*, 702–711.

Krolik, J. H. & G. A. Kriss (2001). Warm Absorbers in Active Galactic Nuclei: A Multitemperature Wind. *The Astrophysical Journal 561*, 684–690.

Lagage, P. O., J. W. Pel, M. Authier, J. Belorgey, A. Claret, C. Doucet, D. Dubreuil, G. Durand, E. Elswijk, P. Girardot, H. U. Käufl, G. Kroes, M. Lortholary, Y. Lussignol, M. Marchesi, E. Pantin, R. Peletier, J. F. Pirard, J. Pragt, Y. Rio, T. Schoenmaker, R. Siebenmorgen, A. Silber, A. Smette, M. Sterzik & C. Veyssiere (2004). Succesful commissioning of VISIR: the mid-infrared VLT instrument. *The Messenger 117*, 12–16.

Landi, R., L. Bassani, G. Malaguti, M. Cappi, A. Comastri, M. Dadina, G. D. Cocco, A. C. Fabian, E. Palazzi, G. G. C. Palumbo & M. Trifoglio (2001). BeppoSAX view of NGC 526A: A Seyfert 1.9 galaxy with a flat spectrum. *Astronomy & Astrophysics 379*, 46–53.

Laor, A., A. J. Baarth, L. C. Ho & A. V. Filippenko (2006). Is the broad-line region clumped or smooth? Constraints from the Hα profile in NGC 4395, the least luminous Seyfert 1 galaxy. *The Astrophysical Journal 636*, 83–89.

Lawrence, A. (1991). The relative frequency of broad-lined and narrow-lined active galactic nuclei - Implications for unified schemes. *Monthly Notices of the Royal Astronomical Society 252*, 586–592.

Lawrence, C. R., J. R. Zucker, A. C. S. Readhead, S. C. Unwin, T. J. Pearson & W. Xu (1996). Optical Spectra of a Complete Sample of Radio Sources. I. The Spectra. *The Astrophysical Journal Supplement Series 107*, 541–+.

Lawson, A. J. & M. J. L. Turner (1997). *Ginga* observations of the X-ray spectra of Quasars. *Monthly Notices of the Royal Astronomical Society 288*, 920–944.

Lee, J. C., P. M. Ogle, C. R. Canizares, H. L. Marshall, N. S. Schulz, R. Morales, A. C. Fabian & K. Iwasawa (2001). Revealing the Dusty Warm Absorber in MCG -6-30-15 with the *Chandra* High-Energy Transmission Grating. *The Astrophysical Journal 554*, L13–L17.

Levenson, N. A., K. A.Weaver, T. M. Heckman, H. Awaki & Y. Terashima (2004). Accretion and Outflow in the Active Galactic Nucleus and Starburst of NGC 5135. *The Astrophysical Journal 602*, 135–147.

Levenson, N. A., M. M. Sirocky, L. Hao, H. W. W. Spoon, J. A. Marshall, M. Elitzur & J. R. Houck (2007). Deep Mid-Infrared Silicate Absorption as a Diagnostic of

Obscuring Geometry toward Galactic Nuclei. *The Astrophysical Journal 654*, L45–L48.

Longinotti, A. L., S. Binachi, M. Santos-Lleó, P. Rodríguez-Pascual, M. Guainazzi, M. Cardaci & A. M. T. Pollock (2007). An X-ray look at the Seyfert 1 Galaxy Mrk 590: *XMM-Newton* and *Chandra* reveal complexity in circumnuclear gas. *Astronomy & Astrophysics 470*, 73–81.

Lumsden, S. L., D. M. Alexander & J. H. Hough (2004). Spectropolarimetry of Compton-thin Seyfert 2 galaxies. *Monthly Notices of the Royal Astronomical Society 348*, 1451–1458.

Lumsden, S. L., C. A. Heisler, J. A. Bailey, J. H. Hough & S. Young (2001). Spectropolarimetry of a complete infrared-selected sample of Seyfert 2 galaxies. *Monthly Notices of the Royal Astronomical Society 327*, 459–474.

Lutz, D., R. Maiolino, H. W. W. Spoon & A. F. M. Moorwood (2004). The relation between AGN hard X-ray emission and mid-infrared continuum from ISO spectra: Scatter and unification aspects. *Astronomy & Astrophysics 418*, 465–473.

Lynden-Bell, D. (1969). Galactic Nuclei as Collapsed Old Quasars. *Nature 223*, 690–+.

Maiolino, R., A. Marconi, M. Salvati, G. Risaliti, P. Severgnini, E. Oliva, F. La Franca & L. Vanzi (2001). Dust in active nuclei. *Astronomy & Astrophysics 365*, 28–36.

Maiolino, R. & G. H. Rieke (1995). Low-Luminosity and Obscured Seyfert Nuclei in Nearby Galaxies. *The Astrophysical Journal 454*, 95–+.

Maiolino, R., M. Ruiz, G. H. Rieke & L. D. Keller (1995). New Constraints on the Unified Model of Seyfert Galaxies. *The Astrophysical Journal 446*, 561–+.

Maiolino, R., M. Salvati, L. Bassani, M. Dadina, R. Della Ceca, G. Matt, G. Risaliti & G. Zamorani (1998). Heavy obscuration in X-ray weak AGNs. *Astronomy & Astrophysics 338*, 781–794.

Malaguti, G., G. G. C. Palumbo, M. Cappi, A. Comastri, C. Otani, M. Matsuoka, M. Guainazzi, L. Bassani & F. Frontera (1998). *Beppo*SAX observation of NGC 7674: a new reflection-dominated Seyfert 2 galaxy. *Astronomy & Astrophysics 331*, 519–523.

Malizia, A., L. Bassani, J. B. Stephen, G. Malaguti & G. G. C. Palumbo (1997). High-Energy Spectra of Active Galactic Nuclei. II. Absorption in Seyfert galaxies. *The Astrophysical Journal Supplement Series 113*, 311–331.

Martínez-Sansigre, A., S. Rawlings, M. Lacy, D. Fadda, F. R. Marleau, C. Simpson, C. J. Willot & M. J. Jarvis (2005). The obscuration by dust of most of the growth of supermassive black holes. *Nature 436*, 666–669.

Mason, R. E., T. R. Geballe, C. Packham, N. A. Levenson, M. Elitzur, R. S. Fisher & E. Perlman (2006). Spatially Resolved Mid-Infrared Spectroscopy of NGC 1068: The Nature and Distribution of the Nuclear Material. *The Astrophysical Journal 640*, 612–624.

Mason, R. E., N. A. Levenson, C. Packham, M. Elitzur, J. Radomski, A. O. Petric & G. S. Wright (2006). Dust and PAH Emission in the Star-Forming Active Nucleus of NGC 1097. *The Astrophysical Journal 659*, 241–249.

Meisenheimer, K., K. R. W. Tristram, W. Jaffe, F. Israel, N. Neumayer, D. Raban, H. Röttgering, W. D. Cotton, U. Graser, T. Henning, C. Leinert, B. Lopez, G. Perrin & A. Prieto (2007). Resolving the innermost parsec of Centaurus A at mid-infrared wavelengths. *Astronomy & Astrophysics 471*, 453–465.

Merloni, A., G. Rudnick & T. Di Matteo (2004). Tracing the cosmological assembly of stars and supermassive black holes in galaxies. *Monthly Notices of the Royal Astronomical Society 354*, L37–L42.

Miller, J. S. & R. W. Goodrich (1990). Spectropolarimetry of high-polarization Seyfert 2 galaxies and unified Seyfert theories. *The Astrophysical Journal 355*, 456–467.

Miller, J. S., R. W. Goodrich & W. G. Mathews (1991). Multidirectional views of the active nucleus of NGC 1068. *The Astrophysical Journal 378*, 47–64.

Miniutti, G., A. C. Fabian, N. Anabuki, J. Crummy, Y. Fukazawa, L. Gallo, Y. Haba, K. Hayashida, S. Holt, H. Kunieda, J. Larsson, A. Markowitz, C. Matsumoto, M. Ohno, J. N. Reeves, T. Takahashi, Y. Tanaka, Y. Terashima, K. Torii, Y. Ueda, M. Ushio, S. Watanabe, M. Yamauchi & T. Yaqoob (2007). Suzaku Observations of the Hard X-Ray Variability of MCG-6-30-15: the Effects of Strong Gravity around a Kerr Black Hole. *Publications of the Astronomical Society of Japan 59*, 315–325.

Miniutti, G., G. Ponti, M. Dadina, M. Cappi & G. Malaguti (2007). IRAS 13197-1627 has them all: Compton-thin absorption, photoionized gas, thermal plasmas and a broad Fe line. *Monthly Notices of the Royal Astronomical Society 375*, 227–239.

Moran, E. C. (2007). Spectropolarimetry Surveys of Obscured AGNs. In L. C. Ho & J.-W. Wang (Eds.), *Astronomical Society of the Pacific Conference Series*, Volume 373 of *Astronomical Society of the Pacific Conference Series*, pp. 425–+.

Moran, E. C., A. J. Barth, L. E. Kay & A. V. Filippenko (2000). The Frequency of Polarized Broad Emission Lines in Type 2 Seyfert Galaxies. *The Astrophysical Journal 540*, L73–L77.

Moran, E. C., L. E. Kay, M. Davies, A. V. Filippenko & A. J. Baarth (2001). A Composite Seyfert 2 X-ray Spectrum: Implications for the Origin of the Cosmic X-ray Background. *The Astrophysical Journal 556*, L75–L78.

Mueller Sánchez, F., R. I. Davies, F. Eisenhauer, L. J. Tacconi, R. Genzel & A. Sternberg (2006). SINFONI adaptive optics integral field spectroscopy of the Circinus Galaxy. *Astronomy & Astrophysics 454*, 481–492.

Müller, S. A. H., M. Haas, R. Siebenmorgen, U. Klaas, K. Meisenheimer, R. Chini & M. Albrecht (2004). Dust in 3CR radio galaxies: On the FR 1 - FR 2 difference. *Astronomy & Astrophyscis 426*, L29–L32.

Nagar, N. M., E. Oliva & R. Maiolino (2002). NGC 5506 unmasked as a Narrow Line Seyfert 1: A direct view of the broad line region using near-IR spectroscopy. *Astronomy & Astrophysics 391*, L21–L24.

Nemmen, R. S., T. Storchi-Bergmann, F. Yuan, M. Eracleous, Y. Terashima & A. S. Wilson (2006). Radiatively Inefficient Accretion Flow in the Nucleus of NGC 1097. *The Astrophysical Journal 643*, 652–659.

Nenkova, M., Z. Ivezić & M. Elitzur (2002). Dust Emission from Active Galactic Nuclei. *The Astrophysical Journal 570*, L9–L12.

Nicastro, F. (2000). Broad Emission Line Regions in Active Galactic Nuclei: The Link with the Accretion Power. *The Astrophysical Journal 530*, L65–L68.

Nicastro, F., A. Martocchia & G. Matt (2003). The Lack of Broad-Line Regions in Low Accretion Rate Active Galactic Nuclei as Evidence of Their Origin in the Accretion Disk. *The Astrophysical Journal 589*, L13–L16.

Osterbrock, D. E. & A. Martel (1993). Spectroscopic study of the CfA sample of Seyfert galaxies. *The Astrophysical Journal 414*, 552–562.

Owen, F. N., C. P. O'Dea & W. C. Keel (1990). Long-slit spectroscopy of 3C 31, 3C 75, 3C 465, NGC 1265, and Cygnus A. *The Astrophysical Journal 352*, 44–54.

Panessa, F. & L. Bassani (2002). Unabsorbed Seyfert 2 galaxies. *Astronomy & Astrophysics 394*, 435–442.

Panessa, F., L. Bassani, M. Cappi, M. Dadina, X. Barcons, F. J. Carrera, L. C. Ho & K. Iwasawa (2006). On the X-ray, optical emission line and black hole mass properties of local Seyfert galaxies. *Astronomy & Astrophysics 455*, 173–185.

Paturel, G., C. Petit, P. Prugniel, G. Theureau, J. Rousseau, M. Brouty, P. Dubois & L. Cambrésy (2003). HYPERLEDA. I. Identification and designation of galaxies. *Astronomy & Astrophysics 412*, 45–55.

Perley, R. A., J. W. Dreher & J. J. Cowan (1984). The jet and filaments in Cygnus A. *The Astrophysical Journal 285*, L35–L38.

Phinney, E. S. (1989). Dusty Disks and the Infrared Emission from AGN. In J. F. W. J. Duschl, F. Meyer (Ed.), *NATO ASIC Proc. 290: Theory of Accretion Disks*, Volume 290, pp. 457–470.

Pier, E. A. & J. H. Krolik (1992). Radiation-pressure-supported obscuring tori around active galactic nuclei. *The Astrophysical Journal 399*, L23–L26.

Pier, E. A. & J. H. Krolik (1993). Infrared Spectra of Obscuring Dust Tori around Active Galactic Nuclei. II. Comparison with Observations. *The Astrophysical Journal 418*, 673–+.

Pogge, R. W. (1989). The circumnuclear environment of nearby, noninteracting Seyfert galaxies. *The Astrophysical Journal 345*, 730–751.

Polletta, M., D. Weedman, S. Hönig, C. J. Lonsdale, H. E. Smith & J. Houck (2007). Obscuration in extremely luminous quasars. *The Astrophysical Journal accepted, astro-ph 0709.4458.*

Pringle, J. E. (1996). Self-induced warping of accretion discs. *Monthly Notices of the Royal Astronomical Society 281*, 357–361.

Quirrenbach, A., A. Witzel, T. P. Kirchbaum, C. A. Hummel, R. Wegner, C. J. Schalinski, M. Ott, A. Alberdi & M. Rioja (1992). Statistics of intraday variability in extragalactic radio sources. *Astronomy & Astrophysics 258*, 279–284.

Ramos Almeida, C., A. M. Pérez García, J. A. Acosta-Pulido & J. M. Rodríguez Espinosa (2007). The mid-infrared emission of Seyfert galaxies. A new analysis of ISOCAM data. *The Astronomical Journal 134*, 2006–2019.

Rejkuba, M. (2004). The distance to the giant elliptical galaxy NGC 5128. *Astronomy & Astrophysics 413*, 903–912.

Revnivtsev, M., S. Sazonov, K. Jahoda & M. Gilfanov (2004). RXTE alls-sky slew survey. Catalog of X-ray sources at $|b| > 10°$. *Astronomy & Astrophysics 418*, 927–936.

Reynolds, C. S., L. W. Brenneman, J. Wilms & M. E. Kaiser (2004). Iron line spectroscopy of NGC 4593 with XMM-Newton: where is the black hole accretion disc? *Monthly Notices of the Royal Astronomical Society 352*, 205–210.

Reynolds, C. S., M. J. Ward, A. C. Fabian & A. Celotti (1997). A multiwavelength study of the Seyfert 1 galaxy MCG-6-30-15. *Monthly Notices of the Royal Astronomical Society 291*, 403–+.

Richard, D. & J.-P. Zahn (1999). Turbulence in differentially rotating flows. What can be learned from the Couette-Taylor experiment. *Astronomy & Astrophysics 347*, 734–738.

Richstone, D., E. A. Ajhar, R. Bender, G. Bower, A. Dressler, S. M. Faber, A. V. Filippenko, K. Gebhardt, R. Green, L. C. Ho, J. Kormendy, T. R. Lauer, J. Magorrian & S. Tremaine (1998). Supermassive black holes and the evolution of galaxies. *Nature 395*, A14–+.

Risaliti, G. (2002). The BeppoSAX view of bright Compton-thin Seyfert 2 galaxies. *Astronomy & Astrophysics 386*, 379–398.

Risaliti, G., M. Elvis & F. Nicastro (2002). biquitous Variability of X-Ray-absorbing Column Densities in Seyfert 2 Galaxies. *The Astrophysical Journal 571*, 234–246.

Roche, P. F., D. K. Aitken, C. H. Smith & M. J. Ward (1991). An atlas of mid-infrared spectra of galaxy nuclei. *Monthly Notices of the Royal Astronomical Society 248*, 606–629.

Rowan-Robinson, M. (1977). On the unity of activity in galaxies. *The Astrophysical Journal 213*, 635–647.

Rush, B., M. A. Malkan & L. Spinoglio (1993). The extended 12 micron galaxy sample. *The Astrophysical Journal Supplement Series 89*, 1–33.

Salpeter, E. E. (1964). Accretion of Interstellar Matter by Massive Objects. *The Astrophysical Journal 140*, 796–800.

Sambruna, R. M., I. M. George, R. F. Mushotzky, K. Nandra & T. J. Turner (1998). ASCA Observations of the Broad-Line Radio Galaxy 3C 445. *The Astrophysical Journal 495*, 749–756.

Sambruna, R. M., J. N. Reeves & V. Braito (2007). The Remarkable X-Ray Spectrum of the Broad-Line Radio Galaxy 3C 445. *The Astrophysical Journal 665*, 1030–1037.

Sanders, D. B. & I. F. Mirabel (1996). Luminous Infrared Galaxies. *Annual Review of Astronomy & Astrophysics 34*, 749–792.

Sanders, D. B., B. T. Soifer, J. H. Elias, G. Neugebauer & K. Matthews (1988). Warm Ultraluminous Galaxies in the *IRAS* survey: The transition from Galaxy to Quasar? *The Astrophysical Journal 328*, L35–L39.

Sanders, R. H. (1974). Super-relativistic phase velocities of radio source components. *Nature 248*, 390–+.

Schartmann, M., K. Meisenheimer, M. Camenzind, S. Wolf & T. Henning (2005). Towards a physical model of dust tori in Active Galactic Nuclei. Radiative transfer calculations for a hydrostatic torus model. *Astronomy & Astrophysics 437*, 861–881.

Schinnerer, E., A. Eckart, L. J. Tacconi & R. Genzel (2000). Bars and Warps traced by the Molecular Gas in the Seyfert 2 Galaxy NGC 1068. *The Astrophysical Journal 533*, 850–868.

Schmidt, M. (1963). 3C 273: a star-like object with large red-shift. *Nature 197*, 1040–1040.

Schödel, R., T. Ott, R. Genzel, A. Eckart, N. Mouawad & T. Alexander (2003). Stellar Dynamics in the Central Arcsecond of Our Galaxy. *The Astrophysical Journal 596*, 1015–1034.

Scott, J. E., G. A. Kriss, J. C. Lee, J. K. Quijano, M. Brotherton, C. R. Canizares, R. F. Green, J. Hutchings, M. E. Kaiser, H. Marshall, W. Oegerle, P. Ogle & W. Zheng (2005). Intrinsic Absorption in the Spectrum of NGC 7469: Simultaneous *Chandra*, *FUSE*, and STIS Observations. *The Astrophysical Journal 634*, 193–209.

Seyfert, C. K. (1943). Nuclear emission in Spiral Nebulae. *The Astrophysical Journal 97*, 28–41.

Shakura, N. I. & R. A. Sunyaev (1973). Black holes in Binary Systems. Observational Appearance. *Astronomy & Astrophysics 24*, 337–355.

Shields, G. A. (1999). A Brief History of Active Galactic Nuclei. *Publications of the Astronomical Society of the Pacific 111*, 661–678.

Shields, G. A., K. L. Menezes, C. A. Massart & P. Vanden Bout (2006). The Black Hole-Bulge Relationship for QSOs at High Redshift. *The Astrophysical Journal 641*, 683–688.

Shields, J. C. (2007). Emission-Line versus Continuum Correlations in Active Galactic Nuclei. In L. C. Ho & J.-M. Wang (Eds.), *The Central Engine of Active Galactic Nuclei*, ASP Conference Series, pp. 355–+.

Shinozaki, K., T. Miyaji, Y. Ishisaki, Y. Ueda & Y. Ogasaka (2006). Spectral Statistics and Local Luminosity Function of a Complete Hard X-Ray Sample of the Brightest Active Galactic Nuclei. *The Astronomical Journal 131*, 2843–2858.

Siebenmorgen, R., M. Haas, E. Krügel & B. Schulz (2005). Discovery of 10μm silicate emission in quasars. Evidence of the AGN unification scheme. *Astronomy & Astrophysics 436*, L5–L8.

Siebenmorgen, R., E. Krügel & H. W. W. Spoon (2004). Mid-infrared emission of galactic nuclei. TIMMI2 versus ISO observations and models. *Astronomy & Astrophysics 414*, 123–139.

Silverman, J. D., P. J. Green, W. A. Barkhouse, R. A. Cameron, C. Foltz, B. T. Jannuzi, D.-W. Kim, M. Kim, A. Mossman, H. Tananbaum, B. J. Wilkes, M. G. Smith, R. C. Smith & P. S. Smith (2005). Co-moving space density of X-ray selected active galactic nuclei. *The Astrophysical Journal 624*, 630–637.

Simpson, C. (2005). The luminosity dependence of the type 1 active galactic nucleus fraction. *Monthly Notices of the Royal Astronomical Society 360*, 565–572.

Smette, A. & L. Vanzi (2007). *VISIR User Manual* (v80 ed.). European Southern Observatory. Released by O. Hainaut.

Soldatenkov, D. A., A. A. Vikhlinin & M. N. Pavlinsky (2003). Soft X-ray Sources at the Centers of the Elliptical Galaxies NGC 4472 and NGC 4649. *Astronomy Letters 29*, 298–303.

Spearman, C. (1904). The proof and measurement of association between two things. *American Journal of Psychology 15*, 72–101.

Spergel, D. N., R. Bean, O. Doré, M. R. Nolta, C. L. Bennett, J. Dunkley, G. Hinshaw, N. Jarosik, E. Komatsu, L. Page, H. V. Peiris, L. Verde, M. Halpern, R. S. Hill, A. Kogut, M. Limon, S. S. Meyer, N. Odegard, G. S. Tucker, J. L. Weiland, E. Wollack & E. L. Wright (2006). Wilkinson Microwave Anisotropy Probe (WMAP) Three Year Results: Implications for Cosmology. *astro-ph 0603449*.

Starling, R. L. C., M. J. Page, G. Branduardi-Raymont, A. A. Breeveld, R. Soria & K. Wu (2005). The X-ray spectrum of NGC 7213 and the Seyfert-LINER connection. *Monthly Notices of the Royal Astronomical Society 356*, 727–733.

Steenbrugge, K. C., J. S. Kaastra, A. J. Blustin, G. Branduardi-Raymont, M. Sako, E. Behar, S. M. K. F. B. S. Paerels & R. Walter (2003). Chandra LETGS and XMM-Newton observations of NGC 4593. *Astronomy & Astrophysics 408*, 921–928.

Storchi-Bergmann, T., A. S. Wilson & J. A. Baldwin (1992). The ionization cone, ob-scured nucleus, and gaseous outflow in NGC 3281 - A prototypical Seyfert 2 galaxy? *The Astrophysical Journal 396*, 45–61.

Strateva, I. V., W. N. Brandt, M. Eracleous, D. P. Schneider & G. Chartas (2006). The X-Ray Properties of Active Galactic Nuclei with Double-peaked Balmer Lines. *The Astrophysical Journal 651*, 749–766.

Sturm, E., D. Rupke, A. Contursi, , D.-C. Kim, D. Lutz, H. Netzer, S. Veilleux, R. Genzel, M. Lehnert, L. J. Tacconi, D. Maoz, J. Mazzarella, S. Lord, D. Sanders & A. Sternberg (2006). Mid-Infrared diagnostics of LINERs. *The Astrophysical Journal 653*, L13–L16.

Sturm, E., M. Schweitzer, D. Lutz, A. Contursi, R. Genzel, M. D. Lehnert, L. J. Tacconi, S. Veilleux, D. S. Rupke, D.-C. Kim, A. Sternberg, D. Maoz, S. Lord, J. Mazzarella & D. B. Sanders (2005). Silicate emissions in active galaxies - From LINERs to QSOs. *The Astrophysical Journal 629*, L21–L23.

Suganuma, M., Y. Yoshii, Y. Kobayashi, T. Minezaki, K. Enya, H. Tomita, T. Aoki, S. Koshida & B. A. Peterson (2006). Reverberation Measurements of the Inner Radius of the Dust Torus in Nearby Seyfert1 Galaxies. *The Astrophysical Journal 639*, 46–63.

Tanaka, Y., K. Nandra, A. C. Fabian, H. Inoue, C. Otani, T. Dotani, K. Hayashida, K. Iwasawa, T. Kii, H. Kunieda, F. Makino & M. Matsuoka (1989). Gravitationally Redshifted Emission Implying an Accretion Disk and Massive Black-Hole in the Active Galaxy MCG:-6-30-15. *Nature 375*, 659–+.

Tananbaum, H., H. Gursky, E. Kellogg & R. Giacconi (1972). Observation of a Correlated X-Ray Transition in Cygnus X-1. *The Astrophysical Journal 177*, l5–l10.

Tavecchio, F., L. Maraschi & G. Ghisellini (1998). Constraints on the Physical Parame-ters of TeV Blazars. *The Astrophysical Journal 509*, 608–619.

Terashima, Y., N. Iyomoto, L. C. Ho & A. F. Ptak (2002). X-Ray Properties of LIN-ERs and Low-Luminosity Seyfert Galaxies Observed with ASCA. I. Observations and Results. *The Astrophysical Journal Supplemet Series 139*, 1–36.

Terashima, Y., H. Kunieda, K. Misaki, R. F. Mushotzky, A. F. Ptak & G. A. Reichert (1998). Detection of an Iron K Emission Line from the LINER NGC 4579. *The Astrophysical Journal 503*, 212–218.

Thorne, K. S. & R. H. Price (1975). Cygnus X-1 - an interpretation of the spectrum and its variability. *The Astrophysical Journal 195*, L101–L105.

Tran, H. D. (2001). Hidden Broad-Line Seyfert 2 Galaxies in the Cfa and $12 \, \mu$m Samples. *The Astrophysical Journal 554*, L19–L23.

Tran, H. D. (2003). The Unified Model and Evolution of Active Galaxies: Implications from a Spectropolarimetric Study. *The Astrophysical Journal 583*, 632–648.

Tran, H. D., J. A. Mader & J. Lyke (2005). The Lack of Broad Line Regions in Unobscured Seyfert 2 Galaxies. In *Bulletin of the American Astronomical Society*, Volume 37, pp. 1444–+.

Tran, H. D., J. S. Miller & L. E. Kay (1992). Detection of obscured broad-line regions in four Seyfert 2 galaxies. *The Astrophysical Journal 397*, 452–456.

Treister, E. & C. M. Urry (2006). The Evolution of Obscuration in Active Galactic Nuclei. *The Astrophysical Journal 652*, L79–L82.

Treister, E., C. M. Urry & P. Lira (2006). AGN unification and the X-ray background. In A. Wilson (Ed.), *The X-ray Universe 2005*, Volume 604 of *ESA Special Publication*, pp. 845–+.

Tristram, K. R. W., K. Meisenheimer, W. Jaffe, M. Schartmann, H.-W. Rix, C. Leinert, S. Morel, M. Wittkowski, H. Röttgering, G. Perrin, B. Lopez, D. Raban, W. D. Cotton, U. Graser, F. Paresce & T. Henning (2007). Resolving the complex structure of the dust torus in the active galactic nucleus of the Circinus galaxy. *Astronomy & Astrophysics 474*.

Tully, R. B. (1988). *Nearby Galaxies Catalog*. Cambridge, UK: Cambridge University Press.

Turner, T. J., I. M. George, K. Nandra & R. F. Mushotzky (1997). ASCA Observations of Type 2 Seyfert Galaxies. I. Data Analysis Results. *The Astrophysical Journal 113*, 23–67.

Ueda, Y., S. Eguchi, Y. Terashima, R. Mushotzky, J. Tueller, C. Markwardt, N. Gehrels, Y. Hashimoto & S. Potter (2007). *Suzaku* observations of Active Galactic Nuclei detected in the *Swift* BAT survey: Discovery of a "new type" of buried supermassive black holes. *The Astrophysical Journal 664*, L79–L82.

Ulvestad, J. S. & A. S. Wilson (1984). Radio structures of Seyfert galaxies. VI – VLA observations of a nearby sample. *The Astrophysical Journal 285*, 439–452.

Urry, C. M. & P. Padovani (1995). Unified Schemes for Radio-Loud Active Galactic Nuclei. *Publications of the Astronomical Society of the Pacific 107*, 803–845.

Vasudevan, R. V. & A. C. Fabian (2007). Piecing together the X-ray background: bolometric corrections for active galactic nuclei. *Monthly Notices of the Royal Astronomical Society accepted*.

Véron-Cetty, M.-P. & P. Véron (2000). A CATALOGUE OF QUASARS AND ACTIVE NUCLEI (9th edition). *ESO scientific report 19*.

Véron-Cetty, M.-P. & P. Véron (2006). A catalogue of quasars and active nuclei: 12th edition. *Astronomy & Astrophysics 455*, 773–777.

Vollmer, B., T. Beckert & W. J. Duschl (2004). From the Circumnuclear Disk in the Galactic Center to thick, obscuring tori of AGNs. *Astronomy & Astrophysics 413*, 949–957.

Wandel, A. (1999). The Black Hole-to-Bulge Mass Relation in Active Galactic Nuclei. *The Astrophysical Journal 519*, L39–L42.

Webster, B. L. & P. Murdin (1972). Cygnus X-1–a Spectroscopic Binary with a Heavy Companion? *Nature 235*, 37–+.

Weigelt, G., M. Wittkowski, Y. Y. Balega, T. Beckert, W. J. Duschl, K.-H. Hofmann, A. B. Men'shchikov & D. Schertl (2004). Diffraction-limited bispectrum speckle interferometry of the nuclear region of the Seyfert galaxy NGC 1068 in the H and K' bands. *Astronomy & Astrophysics 425*, 77–87.

Wittkowski, M., P. Kervella, P. Arsenault, F. Paresce, T. Beckert & G. Weigelt (2004). VLTI/VINCI observations of the nucleus of NGC 1068 using the adaptive optics system MACAO. *Astronomy & Astrophysics 418*, L39–L42.

Wolter, A., I. M. Gioia, J. P. Henry & C. R. Mullis (2005). Unobscured QSO 2: a new class of objects? *Astronomy & Astrophysics 444*, 165–174.

Yaqoob, T. & U. Padmanabhan (2004). The Cores of the Fe K Lines in Seyfert 1 Galaxies Observed by the Chandra High Energy Grating. *The Astrophysical Journal 604*, 63–73.

Zakamska, N. L., G. D. Schmidt, P. S. Smith, M. A. Strauss, J. H. Krolik, P. B. Hall, G. T. Richards, D. P. Schneider, J. Brinkmann & G. P. Szokoly (2005). Candidate Type II Quasars from the Sloan Digital Sky Survey. III. Spectropolarimetry Reveals Hidden Type I Nuclei. *The Astronomical Journal 129*, 1212–1224.

Zeldovich, Y. B. (1964). ? *Akademia nauk SSSR Doklady 155*, 67 (also 158, 811).

Zhang, E.-P. & J.-M. Wang (2006). The Unified Model of Active Galactic Nuclei. I. Non-Hidden-Broad-Line Region Seyfert 2 and Narrow-Line Seyfert 1 Galaxies. *The Astrophysical Journal 653*, 137–151.

Zhou, X.-L. & J.-M. Wang (2005). Narrow Iron Kα Lines in Active Galactic Nuclei: Evolving Populations? *The Astrophysical Journal 618*, L83–L86.

Acknowledgments

been Paulina Jiron, always organising everything, and Maria Eugenia Gomez who somehow managed to find even the most obscure articles. Muchas gracias a toda la gente de la ESO Chile! Uds. me dieron un tiempo inolvidable.

And finally, I would be nothing without my friends! The many great people I met in Chile made this a very special and exciting time for me and my thanks goes out to all of them. I would also like to thank the members of Wolfgang Duschl's group in Kiel who gave me a very warm welcome after my two years of absence. In addition, I thank all my friends and family out there for just being what they are: wonderful people.